APPLICATION OF AN ALL-SOLID-STATE DIODE-LASER-BASED SENSOR FOR CARBON MONOXIDE DETECTION BY OPTICAL ABSORPTION IN THE 4.4 – 4.8 μm SPECTRAL REGION

A Dissertation

by

RODOLFO BARRON JIMENEZ

Submitted to the Office of Graduate Studies of
Texas A&M University
in partial fulfillment of the requirements for the degree of

DOCTOR OF PHILOSOPHY

December 2004

Major Subject: Mechanical Engineering

APPLICATION OF AN ALL-SOLID-STATE DIODE-LASER-BASED SENSOR FOR CARBON MONOXIDE DETECTION BY OPTICAL ABSORPTION IN THE 4.4 – 4.8 μm SPECTRAL REGION

A Dissertation

by

RODOLFO BARRON JIMENEZ

Submitted to Texas A&M University
in partial fulfillment of the requirements
for the degree of

DOCTOR OF PHILOSOPHY

Approved as to style and content by:

J. A. Caton (Co-Chair of Committee)	R. P. Lucht (Co-Chair of Committee)
D. Phares (Member)	G. R. Welch (Member)
D. O'Neal (Head of Department)	

December 2004

Major Subject: Mechanical Engineering

ABSTRACT

Application of an All-Solid-State Diode-Laser-Based Sensor for Carbon Monoxide Detection by Optical Absorption in the 4.4 – 4.8 μm Spectral Region. (December 2004)

Rodolfo Barron Jimenez, B.S., Universidad de Guanajuato;

M.S., Texas A&M University

Co-Chairs of Advisory Committee: Dr. J. A. Caton
Dr. R. P. Lucht

An all-solid-state continuous-wave (cw) laser system for mid-infrared absorption measurements of the carbon monoxide (CO) molecule has been developed and demonstrated. The single-mode, tunable output of an external-cavity diode laser (ECDL) is difference-frequency mixed (DFM) with the output of a 550-mW diode-pumped cw Nd:YAG laser in a periodically-poled lithium niobate (PPLN) crystal to produce tunable cw radiation in the mid-infrared. The wavelength of the 860-nm ECDL can be coarse tuned between 860.78 to 872.82 nm allowing the sensor to be operated in the 4.4 – 4.8 μm region. Results from single-pass mid-IR direct absorption experiments for CO concentration measurements are discussed. CO measurements were performed in $CO/CO_2/N_2$ mixtures in a room temperature gas cell that allowed the evaluation of the sensor operation and data reduction procedures. Field testing was performed at two locations: in the exhaust of a well-stirred reactor (WSR) at Wright-Patterson Air Force Base and the exhaust of a gas turbine at Honeywell Engines and Systems. Field tests demonstrated the feasibility of the sensor for operation in harsh combustion environments but much improvement in the sensor design and operation was required. Experiments in near-adiabatic hydrogen/air CO_2-doped flames were performed featuring two-line thermometry in the 4.8 μm spectral region. The sensor concentration measurement uncertainty was estimated at 2% for gas cell testing. CO concentration measurements agreed within 15% of conventional extractive sampling at WSR, and for the flame experiments the repeatability of the peak absorption gives a system uncertainty of 10%. The noise equivalent CO detection limit for these experiments was estimated at 2 ppm per meter, for combustion gas at 1000 K assuming a SNR ratio of 1.

DEDICATION

This work and all of the implicit effort is dedicated to my grandparents: *Papa Tino*†, *Abuelita Josefina*, *Papa Lito*†, and *Abuelita Felipita*†. Because your example, love, and legendary charisma has propelled me through my life to my goals. God bless you.

Faustino Barrón Moreno†

Josefina Domínguez de Barrón

Heliodoro Jiménez Alvarez†

Felipa Bárcenas de Jiménez†

ACKNOWLEDGMENTS

This research was supported by the Air Force Research Laboratory, Propulsion Directorate, Wright-Patterson AFB through Innovative Scientific Solutions, Inc. under Contract #F33615-00-C-2020, by the U.S. EPA under Project No. R-82818001, and by the U.S. DOE through Honeywell Power Systems under contract #DE-FC02-00-CH11053.

I would like to express my deep thankfulness to Dr. R. P. Lucht for his trust, support and the opportunities he has offered me while introducing and leading me in the combustion diagnostics world. I also wish to acknowledge Drs. Th. Walther and J. A. Caton for their friendship, patience and teachings which have allowed this project to move forward.

Thank you to all of the current and former personnel of the Diode-Laser-Based Sensor Laboratory who helped me in this venture, especially to good friends, G. Ray, T. N. Anderson, and S. F. Hanna from whom I learned, shared and enjoyed this pre-doctoral stage.

Field testing of the sensor could not have been possible without the assistance and hard work of a number of people. Dr. J. R. Gord, Dr. M. S. Brown, Dr. S. Roy, Dr. S. Stauffer and Mike Arstingstall at Wright-Patterson AFB and Innovative Scientific Solutions Inc. helped in performing the WSR exhaust experiments. Ian Critchley and Luis Flamand, at Honeywell Engines and Systems supported and facilitated the sensor testing in the gas turbine.

Finally, I would like to thank all those who supported me through my time in College Station. Part of my education has been supported by CONACYT through a national scholarship. I deeply appreciate the support, friendship and encouragement from my loved ones and friends, a long list of people either close or far away, whom I consider my extended family.

TABLE OF CONTENTS

CHAPTER Page

Page

LIST OF FIGURES

FIGURE Page

FIGURE Page

FIGURE Page

FIGURE Page

FIGURE Page

LIST OF TABLES

CHAPTER I

INTRODUCTION

1.1 Carbon Monoxide

Carbon monoxide (CO) is considered one of the six principal pollutants by the Environmental Protection Agency (EPA). Its concentration was regulated in 1994 by the National Ambient Air Quality Standards (NAAQS) to be less than 9 ppm (10mg/m^3) average for an eight hour period and 35 ppm (40 mg/m^3) for a one hour period [1]. Information in the following paragraphs is intended to be a brief summary of the "Air Quality Criteria for Carbon Monoxide [1]," which provides an excellent review of the effects of CO on human health as well as its role in the atmosphere.

When carbon monoxide is present in the blood stream it will combine with hemoglobin, displacing oxygen and producing carboxyhemoglobin (COHb). CO thus interferes with cellular respiration causing hypoxia. Although there are intrinsic physiologic mechanisms to counteract the effects of hypoxia (e.g., increased blood flow and oxygen extraction), the elimination of the COHb can take from 2 to 6.5 hours. When the CO concentration increases and overwhelms these defense mechanisms, hypoxia causes health effects or death. At COHb levels >20% significant behavioral impairments in healthy individuals are expected; however, mild central nervous system effects have been reported at COHb levels between 5 to 20%. COHb levels <5% are expected from exposure to typical ambient CO, and current research emphasizes the understanding of health effects at lower COHb levels.

In the atmosphere, carbon monoxide plays an important role as the principal reactant for hydroxyl (OH) radicals. Many trace gases (e.g. CH_4) are destroyed in the atmosphere by reacting with OH radicals. Thus an increase of CO concentration can reduce the presence of OH radicals and allow these trace gases to contribute to global environmental problems like the greenhouse effect or the depletion of ozone. On the contrary, decreasing the CO concentration can stabilize or reverse the growth of trace gases.

This dissertation follows the style and format of Applied Physics B - Lasers and Optics.

Due to the adverse effects on the environment and human health, carbon monoxide emissions from anthropogenic sources are regulated. Anthropogenic CO originates from methane oxidation, fossil fuel and biomass combustion. CO emission from non-road sources has increased from 12.7% in 1988 to 19.2% in 1997 [1]. Mobile sources accounted for 80% of the 1997 nationwide emissions inventory for CO such that the decline in ambient CO concentrations follows the decline in CO vehicle emissions. Table 1 shows how tight the CO emission standards for passenger cars have become in the state of California [2].

Emission Standard		Time Period	Vehicle Durability [miles]		
			50,000	100,000	120,000
LEV I	TLEV	2001 – 2003	3.4	4.2	
	LEV	2001 – 2006	3.4	4.2	
	ULEV	2001 – 2006	1.7	2.1	
LEV II	LEV	2004	3.4		4.2
	ULEV	2004	1.7		4.2
	SULEV	2004			1.0

TLEV – Transitional low-emission vehicle
LEV – Low-emission vehicle,
ULEV – ultra-low-emission vehicle
SULEV – Super-ultra-low-emission vehicle

TABLE 1 California CO emission standards [gram per mile] for passenger cars [2]

1.2 CO Sensor Technology

Quantitative measurements of carbon monoxide are important in molecular physics, chemistry and astrophysics, but CO concentration measurements are primarily required to monitor and control its potential effects on human health. A number of technologies have been developed to monitor ambient CO as well as to monitor and control CO emissions from combustion sources. A brief review of the optical and chemical sensors for carbon monoxide is presented below.

1.2.1 Monitoring of ambient CO

Biological and atmospheric monitoring of carbon monoxide has been an active research topic driven by the need for reliable measurement methods to assure regulation compliance. The EPA performance specifications required for sensors monitoring CO in ambient urban air includes a range from

0 to 50 ppm, a detection limit of 1.0 ppm, and a precision of 0.5 ppm. Monitoring CO in non-urban areas might require better sensors. The EPA has approved a reference monitoring method based on absorption of infrared radiation from a nondispersed source (e.g. collimated radiation from an IR lamp); this technique is generally accepted as being the most reliable method for measurement of CO in ambient air. Nondispersive infrared (NDIR) analyzers that operate at atmospheric pressure are commercially available with CO-detection limits of about 0.02 ppm [1]. NDIR systems are not sensitive to gas flow rate and are independent of temperature changes in the ambient air. Burch *et al.* [3] described a Gas Filter Correlation (GFC) NDIR absorption instrument that presents no interference from CO_2 and little interference from water vapor. Parrish *et al*. [4] enhanced a commercial GFC-NDIR monitor to approach 1.4 ppb of instrument precision; however, the monitor still requires sampling, filtering, zeroing, and calibration.

Other techniques to monitor ambient CO include Gas Chromatography-Flame Ionization Detection (GC-FID) [5] and Gas Chromatography-Mercury Oxide/Ultraviolet Absoprtion (GC-HgO/UV) [6, 7] with detection limits below 10 ppb. These techniques provide enhanced performance when compared with NDIR analyzers; however, they still require sampling and sample preparation, are sensitive to calibration and rely on chemical processes that affect the CO concentration of the sample. Electrochemical CO sensors have been used for personal exposure and micro-environmental sampling [1, 8-10]. However, electrochemical CO sensors are not EPA approved for compliance monitoring since they lack independent studies to establish equivalence to the NDIR analyzers.

Optical techniques have been used for the measurement of atmospheric CO concentrations. Resonance fluorescence (RF) of CO in vacuum-ultraviolet has been used for airborne CO measurements in the troposphere [11]. Gerbig *et al*. [12] improved the instrument obtaining a detection limit of 3 ppb with a 1 sec integration time. Sensors based on optical absorption provide a means to calculate the CO concentration with high precision, fast response, and interference-free operation without using a calibrated blend of gases to operate. Tunable diode laser spectroscopy (TDLS) in the infrared (IR) spectral region has been used for atmospheric measurements of CO concentration either on an open-path [13] or in samples [14-16].

All of the techniques described above (NDIR, GC-FID, GC-HgO/UV, TDLS) for monitoring of ambient CO concentrations have been evaluated and compared in field environments, and the measured concentrations agreed within experimental uncertainty [1, 5, 7, 15]. For the interested reader, a comprehensive review of atmospheric monitoring techniques for CO and other molecules (e.g. NO_x, H_2O, OH, O_3, CO_2) is presented by Clemitshaw [17].

1.2.2 CO sensors for combustion control

In general, CO is a major species product of fuel rich combustion. Fuel rich combustion is not a desirable operating condition for most combustors or engines. In stoichiometric and slightly lean conditions CO is found as a result of carbon dioxide (CO_2) dissociation. Partial oxidation of hydrocarbons (C_xH_y) at either rich or lean conditions also results in CO production; unburned hydrocarbon emission results from a variety of conditions within the combustion chamber (e.g., incomplete flame propagation, low residence time, wall quenching) so that engine design has been the main control strategy for such emissions.

Combustion is most efficient when its harmful emissions (CO, NO_x, and C_xH_y) are minimized; therefore combustion control is employed to operate at those conditions. Open loop combustion control does not allow for optimization, hence new combustion technologies will integrate feedback controllers. Closed loop control is currently used in automotive engines, and its application is under consideration in many other applications like biomass combustors and gas turbines [18]. Combustion control can be differentiated as Active Combustion Control (ACC) which aims for performance optimization and instability control while Operating Point Control (OPC) is directed towards efficiency and emissions management.

Sensors are of crucial importance in the implementation of combustion control strategies. Their integration in combustion systems was explored by Docquier and Candel [18]. After reviewing current control requirements in automotive engines, gas turbines and combustor performance, Docquier and Candel concluded that the strategies required to met future objectives in pollutant emissions reduction and

instability alleviation will require fast, reliable monitoring of a broad range of parameters (e.g., equivalence ratio, temperature, CO, NO_x, HC concentrations).

In combustion control, relative data is required as oppose to absolute values. Therefore, sensors should be reliable, fast, robust, and should withstand noise and harsh environments. With all these requirements CO is better detected by sensors using solid-state or IR optical absorption technologies.

Solid-state CO sensors have been developed from oxygen sensors. To detect a particular species (CO or NO_x), solid-state sensors use a semiconductor material, such as titanium (TiO_2) [19] or tin (SnO_2) [20], whose electrical resistance changes with oxygen partial pressure. Zirconium oxide (ZrO_2) [21, 22] CO sensors detect voltage or current changes through the semiconductor; they offer greater selectivity and better stability under high temperature conditions. Solid-state sensors face challenges in improving accuracy, selectivity, durability, time response (currently on the order of few seconds), detection thresholds (currently in the range of 10 to 50 ppm), and sensitivity (uncertainties are typically on 10 to 25% and can be influenced by sensor aging) [18]. Solid-state sensors are under development and they have a significant potential for health hazard monitoring and combustion control.

1.2.3 Tunable diode laser absorption spectroscopy

Traditionally, physical probing has been employed to characterize combustion phenomena. However, physical probes are intrusive and can affect the flame behavior through flow disturbance, thermal, and chemical effects. Other issues associated with probe sampling are sample conditioning, calibration, and corrections needed. Optical techniques are superior to traditional techniques for combustion diagnostics since they are non-intrusive and offer spatial and temporal resolution. By being non-intrusive, there is no temperature limit and are not restricted to equilibrium conditions so that non-equilibrium phenomena can be studied.

Eckbreth [23] surveys the laser diagnostics techniques available to the combustion researcher. Some of these techniques have been used for CO detection. Versluis *et al*. [24], Meijer and Chandler [25], and Gregoriev *et al*. [26] used degenerate four wave mixing (DFWM). Polarization spectroscopy (PS) was applied for CO detection in flames by Nyholm *et al*. [27]. Amplified spontaneous emission (ASE) of

the CO molecule has been reported by Westblom *et al*. [28] and Hasegawa and Tsukiyama [29]. Laser-induced fluorescence (LIF) has been extensively applied for CO detection in flames and combustion exhaust gas [30-35]. Although well suited for the lab environment, these techniques are difficult to implement in the field because of mobility and their requirement of powerful laser sources (e.g., excimer-laser) that allow access to weak nonlinear processes.

The telecommunication and consumer electronics industries require room-temperature, wavelength tuning, narrow linewidth, long-term stability, high reliability, small size, and compatibility with fiber optics networks. Thus, these industries had driven the development and refinement of diode laser sources in the visible, near-, and mid-infrared. Many of these lasers have been applied for gas dynamics and combustion diagnostics. Allen [36] presents a review of laser-source technology, detection strategies, and sensor configurations for tunable diode laser absorption spectroscopy (TDLAS).

Room-temperature, tunable, low-cost diode lasers developed for telecommunications have found widespread use in absorption spectroscopy. Tunable diode laser absorption spectroscopy (TDLAS) provides quantitative accuracy, high sensitivity, species selectivity, and time resolution; they are also a rugged, portable (applicable for *in situ* measurements), and low-cost option to develop combustion gas sensors. Optical absorption in the infrared is almost universal since in this spectral region nearly every molecule, except homonuclear diatomics, shows vibration- rotation molecular transitions. Also, Doppler broadening is much smaller for vibration-rotation transitions than for electronic transitions allowing for better resolution in the IR spectrum.

Optical absorption also has disadvantages. It is line-of-sight measurement so it is not spatially resolved and any absorber molecule in the path can interfere contributing to the absorption. These molecular interferences are common because of the large number of absorbing molecules in the IR. Spectral interferences can be avoided by carefully selecting the target absorption transition. Diode lasers have a narrow linewidth and the output frequency can be coarse tuned allowing for species selectivity. Telecommunication diode lasers operate in the near-infrared wavelength region (1000 – 2000 nm.)

In the near-IR spectral region, species such as H2O, CO2, and CO exhibit overtone vibrational transitions which are much weaker than fundamental transitions. Absorption signals are very sensitive to

several sources of noise. With the development of TDLAS several techniques have been applied to improve the sensitivity of the measurements. These techniques include wavelength modulation spectroscopy [37], one- and two-tone frequency modulation spectroscopy [38, 39], etalon fringe reduction [40, 41], increasing the beam path through multiple beam passes, dual-beam and balanced radiometric detection [42], power increase by fiber amplifiers and improvement of infrared laser sources [43] (e.g., Gallium-Arsenide, Antimonide III-V, distributed-feed-back, quantum-cascade laser diodes).

1.2.4 CO detection by infrared TDLAS

To detect carbon monoxide by TDLAS, a specific vibration-rotation transition in the infrared has to be addressed. The spectrum shown in Fig. 1 was generated by the HITRAN HITEMP [44] spectroscopic database, and as can be seen, the CO molecule strongly absorbs IR radiation in one fundamental and three overtone bands located at 4.6 μm, 2.4 μm, 1.6 μm, and 1.2 μm respectively (see Chapter II). The limited availability of diode lasers that access these transitions has driven the development of a new generation of TDLAS based CO-sensors.

There are numerous reports describing infrared (IR) tunable diode-laser spectroscopy of the in the second-overtone band (Δv = 3) carbon monoxide molecule [45-52]. Mihalcea *et al.* [47, 48] developed a

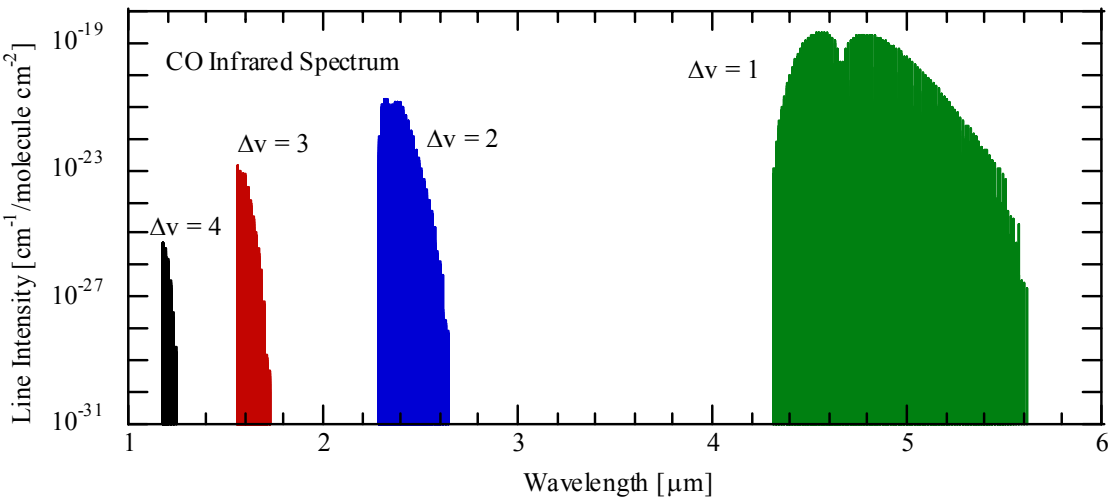

FIGURE 1 Infrared CO spectra at 1000 K. Based on the HITRAN HITEMP [44] database

diode-laser absorption system for combustion emission measurements using a tunable external cavity InGaAsP diode laser in the spectral range 1.49 - 1.58 μm. CO was one of the species detected using the system. CO was detected by identifying the R(13) line in the second-overtone band. Furlong *et al*. [49] used this diode as a component of a real-time closed-loop control system of a pulsed combustion engine. Transitions in the second-overtone band (1.4 – 1.8 μm) of CO are four orders of magnitude weaker than those in the fundamental band. In addition, this spectral region includes strong interference from major species such as carbon dioxide (CO_2) and water (H_2O). With similar diode-laser systems some authors [50-52] have taken advantage of these spectral interferences to perform multi-species detection.

Using a room-temperature, continuous-wave (cw), single mode, research-grade InGaAsSb/AlGaAsSb diode laser operated near 2.3 μm Wang *et al*. [53, 54], Webber *et al*. [55], and Nicolas *et al*. [56] performed absorption measurements on the first-overtone band ($\Delta v = 2$) of the CO molecule. Wang *et al*. [53] determined CO concentrations in the post-flame region [R(30) transition at 4343.81 cm^{-1}] as well as in the duct that carried the exhaust gasses from the flame [R(15) transition at 4311.96 cm^{-1}]. For measurements in the post-flame zone, CO concentrations in rich flames were in good agreement with chemical equilibrium predictions. For measurements in the exhaust, a detection limit of 1.5 ppm-m at 470 K was demonstrated. The detection bandwidth was 50 kHz and the total measurement time was 0.1 s. Wavelength modulation spectroscopy techniques were used to achieve a sensitivity of 0.1 ppm-m. For these measurements the detection bandwidth was 500 Hz with a total measurement time was 0.4 s. In a different combustion study, Lackner *et al*. [57] used a similar diode to measure time evolving CO and CH_4 concentrations close to the surface of a burning particle. Transition lines in the first-overtone are about two orders of magnitude stronger than those in the second-overtone band, and several transitions in the R branch are isolated from spectral interference with CO_2 and H_2O. However, these excellent diode lasers were out of the market and just recently become available again [58].

There are two types of semiconductor diode lasers capable of accessing the fundamental band ($\Delta v = 1$) of carbon monoxide, near 4.6 μm [43]. Lead-salt diode-lasers are made from IV-VI semiconductor materials and operate cryogenically at wavelengths ranging from 3 μm to 30 μm. Lead-salt diodes have

been extensively used for spectroscopic studies of the CO molecule e.g., [59-64], detection of CO in flames e.g., [65, 66], and other atmospheric and combustion processes e.g., [67, 68]. Although successful, the implementation of *in situ* sensors based on lead-salt diodes has been limited due to operational complexity, the requirement of cryogenic cooling of the lasers, and multimode operation. Lead-salt diode lasers have mainly been used for spectroscopic purposes, and without the driving force of the telecommunications market their development is not nearby as advanced as GaAs diodes.

The semiconductor laser alternative to lead-salt diode is the quantum cascade laser (QC). Quantum cascade lasers are based on a completely different operational principle than common semiconductor lasers. Quantum cascade lasers use the same base semiconductors (InGaAs, AlInAs lattices on InP) so that they can generate light in the 3.5 to 24 μm spectral region. Quantum cascade lasers are engineered to be compact narrow-linewidth mid-IR sources producing single-mode radiation with substantially higher powers (e.g., 2-20 mW at 120 K as compared to 200 μW of a cryogenically cooled lead-salt diode). Kosterev and Tittel [69] review the applicability and capabilities of QC lasers in chemical sensing. The recent development of quantum-cascade lasers in a distributed-feedback (QC-DFB) structure has allowed spectroscopic monitoring of CO in gas cells, ambient air and engine exhaust [70-72]. QC lasers are operated in pulsed mode at room-temperature. Continuous wave operating is achieved only at lower temperatures.

Wagner *et al*. [73] reported on the InAs/GaInSb/AlGaAsSb type-II W-laser suited to cover the 3- to 5-μm spectral region. However, the bulk of experimental data reported is concentrated in the 3.2- to 4-μm region. There is room for optimization of type-II design which will allow for cw operation of type-II W-diode lasers up to temperatures which are within the range of thermoelectric coolers in the near future.

In addition to the semiconductor sources of mid-IR, there is a second class of sources of mid-IR radiation based on nonlinear optical parametric frequency conversion; this strategy offers broadband tunability, narrow linewidth, broadband parametric gain, efficient continuous wave (cw) single pass conversion (avoiding the complexity of resonators), near room-temperature operation, and the use of many mature laser technologies to seed the nonlinear conversion to the IR [74]. Among the frequency

conversion processes, difference-frequency-mixing (DFM) provides a mid-IR source (3 to 20 μm) by mixing visible or near-IR fundamental diode lasers. In the literature groups have reported spectroscopic measurements of H_2O, CO_2, CO, NO, C_2H_2, C_6H_6, CH_4, C_2H_4, OCS [75, 76] and other molecules in the IR region using DFM sources.

DFM and in general every nonlinear optical process depends on phase-matching of the mixing beams. Phase matching is achieved using birefringent or periodically poled materials. Detection of CO in the fundamental band by means of DFM in a $AgGaS_2$ birefringent crystal has been reported. Schade *et al*. [77] used a $AgGaS_2$ crystal to obtain DFM radiation in resonance with line P(28) in the fundamental band of CO at 2022.914 cm^{-1}. In a similar, but modular set up, Kelz *et al*. [78] used the same birefringent nonlinear crystal to access the spectral region around 4.76 μm. Recently, Khorsandi *et al*. [79] used this nonlinear crystal to address a nitric oxide transition and the P(27) transition of the fundamental band of CO at 2027.649 cm^{-1}. In their system Khorsandi *et al*. used 789-nm and 682-nm diode lasers; the system had a spectral tuning range of 71.5 cm^{-1} achieved by improving the mode-hop-free range of the pump source by use of a short external cavity. These systems produced low levels of mid-IR radiation from DFM of moderate power diode lasers. Schade *et al*. used 30 and 50 mW fundamental beams to produce 200 nW while Keltz *et al*. and Khorsandi *et al*. typically produced approximately 100 nW of mid-IR radiation.

Quasi-phase-match (QPM) materials have many advantages for the production of mid-IR radiation through nonlinear conversion. QPM materials such as $LiNbO_3$, $LiTaO_3$, $KTiOPO_4$, and $RbTiOAsO_4$ can be engineered to use the largest nonlinear susceptibility component of the material. The power conversion efficiency of DFM processes in periodically-poled lithium niobate (PPLN) is, typically, one order of magnitude higher than the conversion efficiency in birefringent materials [75]. Lancaster *et al.* [80] used a PPLN crystal to produce radiation in the 3.25 to 4.4 μm region; their apparatus produced about 3 μW at 3.3 μm which represents a conversion efficiency of 0.44 $mW/(W^2cm)$, the highest efficiency reported for a portable device.

Absorption sensors based on the use of a PPLN crystal to produce mid-IR radiation in a DFM process have been applied for the detection of trace gases [80-85]. Petrov *et al*. [85] investigated the feasibility of application of a diode-pumped mid-IR difference-frequency-mixing (DFM) source based on a periodically-poled $LiNbO_3$ (PPLN) crystal to detect atmospheric CO, N_2O and CO_2. Their tunable mid-IR DFM source mixed a diode-pumped Nd:YAG ring laser (220 mW at 1064 nm) and 820 mW from a high power GaAlAs tapered amplifier seeded at 860 nm by a diode-laser that allows for fast-frequency tuning by means of current modulation. A maximum of 8 μW was measured at 4.5 μm, however CO measurements were typically performed with 3 μW of mid-IR power. With this system Petrov *et al*. addressed the CO fundamental band at the R(6) transition near 2169 cm^{-1}. The detection sensitivity of 5 ppb-m/√Hz was extrapolated based on rms noise measured in the 2*f* spectra under interference-free conditions in the 4.31 to 4.63 μm spectral region.

Petrov *et al*. [83] reported the development of an all-solid-state compact DFG spectrometer pumped by a widely tunable ECDL and a 700 mW diode-pumped monolithic Nd:YAG ring laser at 1064.5 nm. The 16 mW ECDL was coarse tuned in the region 842 to 865 nm, the output beam was scanned over 80 GHz by a 50 Hz triangular wave. The DFG process generated 0.5 μW radiation in the range 3.98 to 4.62 μm. The spectrometer was used for open path and multi-pass gas-cell measurements of CO, N_2O, and CO_2.

1.3 Objectives

The objective of this research project is to design, build and operate an all-solid-state diode-laser based carbon monoxide sensor capable of sensitive, non-intrusive, single-pass measurements for combustion diagnostics. The specific objectives of this research program are as follows:

1. Design and build the experimental apparatus. This goal includes the optical design of the sensor, selection of operational mid-IR region as well as transition selection, detection strategy.
2. Laboratory testing. Required testing of the system under well controlled laboratory conditions allows us to check the feasibility of the system and to gain insight into basic and detailed

processes from alignment to sensor operation as well as data reduction. Testing in a room-temperature gas-cell will allow for positive identification of the crucial spectroscopic parameters of the CO target transitions.

3. Field testing. Field testing of the CO sensor will demonstrate its feasibility and ability to operate under real combustor conditions. Field testing will allow us to pinpoint and improve potential weakness of the system as well as to evaluate its potential for combustion control. Scheduled field experiments will perform CO measurements on the exhaust of real combustors.
4. Studies on a near adiabatic H_2/Air/CO_2–doped flame. Such flame in the lab environment is able to produce small quantities of CO by CO_2-dissociation. This flame allows for high temperature CO measurements and to study spectral interferences from CO_2 and H_2O that can limit the sensitivity of the system.
5. Evaluate potential applicability to other molecules. Carbon dioxide (CO_2) can be detected in the 4.3 – 5 μm spectral region so that the system is well suited to perform CO_2 measurements. With some modification (e.g., different PPLN crystal, an ECDL lasing at 725-nm), the general layout of the proposed sensor can be used to detected ammonia (NH_3) in the 2.27 to 2.29 μm region.

1.4 Dissertation Organization

This dissertation is divided in six chapters. A brief review of the importance of CO and the motivation for CO concentration measurements are presented in Chapter I, along with the methods available for such measurements. Special emphasis is given to the use of optical sensors for carbon monoxide concentration measurement.

The theoretical background for optical absorption spectroscopy of CO is presented in Chapters II and III. The spectroscopy of diatomic molecules is discussed in Chapter II, with special attention given to the spectroscopy of CO. The theory of quantitative absorption spectroscopy is discussed in Chapter III. The HITRAN database of spectroscopic parameters is briefly described. This database is the primary

source of transition information for theoretical quantitative absorption modeling. Chapter III also includes a brief treatment of nonlinear optical processes, with emphasis on the DFM process.

The CO sensor is described in Chapter IV. The procedures for alignment and data acquisition and processing are also discussed. The code developed for data processing is briefly described in Chapter IV. The code is described in detail in Appendix A.

The results of all measurements using the sensor are presented in Chapter V. Results from room-temperature gas-cell measurements are presented along with line selection criteria. The sensor was used for field tests in two facilities: a gas turbine auxiliary power unit (APU) at Honeywell Engines and Systems and the well-stirred reactor (WSR) at Wright-Patterson Air Force Base. Finally Chapter V describes results from the near-adiabatic H_2/air/CO_2 flames.

Conclusions from this research are presented in Chapter VI. This chapter also includes recommendations for future improvements to the sensor. Chapter VI closes with a discussion of the potential for applying this sensor to detection of other interesting molecules.

CHAPTER II

CARBON MONOXIDE SPECTROSCOPY

In this chapter the spectroscopic properties of the carbon monoxide molecule are reviewed. The molecular spectrum and structure of carbon monoxide are very well understood and modeled. The concepts and notations in this chapter follow the theoretical development by Herzberg [86]. Khristenko *et al*. [87] summarizes and presents the concepts of molecular structure in a narrative, factual fashion. Both references were used extensively in the preparation of this chapter.

2.1 Spectroscopy of Diatomic Molecules – Introduction

A diatomic molecule is formed when the electron shells of two atoms merge so that a chemical bond develops maintaining a stable molecule. In this condition, the electronic structure of each atom changes drastically. The atomic spectrum is related to the electronic energy distribution while for a diatomic molecule two additional modes of motion are possible; rotation of the molecule around an axis perpendicular to the internuclear axis at the center of mass, and vibration of the atoms along the internuclear axis. These vibrational and rotational modes are responsible for the infrared spectral structure.

The molecular energy levels are determined in principle by solving the Schrödinger wave equation (SWE). Numerical solutions of SWE have been performed only for the simplest molecules e.g., H_2. Molecular energy levels are typically analyzed using the Born-Oppenheimer approximation. In this approximation, it is assumed that nuclei move much more slowly than electrons, and electron motion is analyzed assuming stationary nuclei. The Born-Oppenheimer approximation leads to the separation of the total wave function into nuclear and electronic wave functions [88]. As the main consequence, the internal energy of the molecule can be split into electronic, vibrational, and rotational modes. The solution of the SWE for the electrons gives the electronic energy levels, or "potential surfaces" which are dependent on nuclear coordinates. The SWE for the nuclear motion can be divided into two parts: vibrational and

rotational. For each electronic estate there is a unique set of vibrational energy levels whereas for each vibrational level there is a particular set of rotational levels.

The total energy of the molecule can be expressed as:

$$\varepsilon = \varepsilon_{trans} + \varepsilon_{\text{int}} = \varepsilon_{trans} + \varepsilon_{elec} + \varepsilon_{vib} + \varepsilon_{rot} \tag{1}$$

The translational kinetic energy (ε_{trans}) is obtained from the particle-in-the-box solution to the SWE. Electronic (ε_{elec}), vibrational (ε_{vib}), and rotational (ε_{rot}) energies of a diatomic molecule will be treated in detail on the following sections. Table 2 shows the typical spacing of the energy levels of a diatomic molecule; notice that transitions occurring in the infrared are produced by vibrational-rotational changes in the state of the molecule.

$\Delta\varepsilon$	[eV]	$\Delta\varepsilon/hc$	[cm^{-1}]	Spectral Region
Rotational	0.001 – 0.01	ΔF(J)	10 – 100	Microwave, Far-IR
Vibrational	0.05 – 0.2	ΔG(v)	500 - 2000	Mid-IR
Electronic	2 – 5	ΔT(n)	20000 - 50000	Visible, UV

TABLE 2 Typical energy level spacing ($\Delta\varepsilon$) for a diatomic molecule

2.1.1 The rigid rotator

The simplest model for a diatomic molecule is the so called dumbbell model. It considers the two atoms of masses m_a and m_b but neglect the finite extent of the atoms since their mass is mainly concentrated in the nucleus. Both atoms are fastened at the ends of a weightless, rigid rod of length r_e. To determine the energy states of this model the SWE can be solved by setting the potential energy to zero since the rotator is completely rigid.

Solutions to this case of the SWE are single-value, finite, and continuous occurring only at the eigenvalues ε_{rot} as given by

$$\varepsilon_{rot} = \frac{h^2 \mathrm{J}(\mathrm{J}+1)}{8\pi^2 I} \tag{2}$$

where I is the moment of inertia for a rigid rotator of reduced mass μ at a fixed distance r_e from the axis of rotation. The moment of inertia is given by

$$I = \mu r_e^2 \tag{3}$$

$$\mu = \frac{m_\mathrm{a} m_\mathrm{b}}{m_\mathrm{a} + m_\mathrm{b}} \tag{4}$$

J is the rotational quantum number and can take the values J = 0, 1, 2 … notice that the rotational quantum number relates to the angular momentum $(\vec{\mathrm{J}})$ in units of $\hbar = h/2\pi$. This means that the molecule angular momentum vector $(\vec{\mathrm{J}})$ has a magnitude $\sqrt{\mathrm{J}(\mathrm{J}+1)} \cdot (\hbar)$.

The rotational term energy F(J) (in units of wavenumbers [cm^{-1}]) is defined by (5) where the constant *B* is called the rotational constant and is defined by (6).

$$F(\mathrm{J}) = \frac{\varepsilon_{rot}}{hc} = \frac{h}{8\pi^2 c I}\mathrm{J}(\mathrm{J}+1) = B\mathrm{J}(\mathrm{J}+1) \tag{5}$$

$$B = \frac{h}{8\pi^2 c I} \tag{6}$$

2.1.2 The harmonic oscillator

The harmonic oscillator is the simplest model for the vibration of a diatomic molecule. It is assumed that the atoms move away from and towards each other in simple harmonic motion. In classical mechanics a harmonic oscillator can be reduced to a single particle of mass μ that moves about the equilibrium position (r_e) with a sinusoidal motion as a function of time. To solve the SWE for the harmonic oscillator model, the potential energy (V) of the two nuclei is assumed to be given by the classical mechanics solution of the harmonic oscillator (7). The potential energy curve is a parabola where k is the stiffness constant that relates to the oscillation frequency (ν_{osc}) by (8).

$$V = \frac{1}{2}\mathrm{k}(r - r_e)^2 \tag{7}$$

$$\mathrm{k} = 4\pi^2 \mu \nu_{osc}^2 \tag{8}$$

The solution of the SWE is complicated but can be found in the literature; Herzberg [86] recommends the treatment by Puling and Wilson [89]. The solutions are single-valued, finite, continuous, and exist only for the values of ε_{vib} given by

$$\varepsilon_{vib} = \left(\mathrm{v} + \frac{1}{2} \right) h \nu_{osc} \tag{9}$$

where the vibrational quantum number v = 0, 1, 2 … notice that for v = 0, $\varepsilon_{vib} = 0.5 h \nu_{osc}$.

The vibrational term energy (G(v)) is given by

$$G(\mathrm{v}) = \frac{\varepsilon_{vib}}{hc} = \left(\mathrm{v} + \frac{1}{2} \right) \frac{\nu_{osc}}{c} = \omega \left(\mathrm{v} + \frac{1}{2} \right) \tag{10}$$

where the vibrational frequency $\omega = \nu_{osc}/c$ [cm^{-1}] is adopted by band spectroscopy.

2.1.3 Correcting the ideal models

The ideal molecular models of the harmonic oscillator and the rigid rotator explain the main characteristics of the infrared spectrum. Improvement of these models leads to better understanding of the finer details of the molecule. A more accurate representation of the diatomic molecule considers:

2.1.3.1 Vibrational anharmonicity

In the harmonic oscillator model, the potential energy of the two nuclei is described by a parabolic curve, implying that the restoring force between atoms increases linearly with distance. In a real molecule when the atoms are separated sufficiently from one another, the attractive force reduces to zero. Thus the potential function is approximately harmonic only for the lowest vibrational levels (around the equilibrium position, r_e). The actual potential function is better represented by a Morse potential. As a first approximation, a third degree term is added to the quadratic function of the harmonic oscillator,

$$V(r) = f(r - r_e)^2 - g(r - r_e)^3 \tag{11}$$

this function does not represents the whole potential energy curve but it's a better approximation for not too great values of r-r_e. More terms of higher order can be added to the approximation of the potential function (11) for an improved approximation.

A mass point that moves under the influence of a potential curve described by (11) or a Morse potential is called anharmonic oscillator. If the potential energy (11) is substituted in the wave equation for small anharmonicity of the oscillator ($g << f$) the eigenvalues of the anharmonic oscillator are given by

$$\varepsilon_{vib} = hc\omega_e(\mathrm{v}+\tfrac{1}{2}) - hc\omega_e x_e(\mathrm{v}+\tfrac{1}{2})^2 + hc\omega_e y_e(\mathrm{v}+\tfrac{1}{2})^3 + \ldots \tag{12}$$

or the corresponding term energy values

$$\mathrm{G(v)} = \omega_e(\mathrm{v}+\tfrac{1}{2}) - \omega_e x_e(\mathrm{v}+\tfrac{1}{2})^2 + \omega_e y_e(\mathrm{v}+\tfrac{1}{2})^3 + \ldots \tag{13}$$

where v is the vibrational quantum number and the vibrational constants $\omega_e y_e << \omega_e x_e << \omega_e$ are constant for a given electronic level. The vibrational constants can be determined from the observed positions of the IR absorption bands of the diatomic molecule.

2.1.3.2 Centrifugal stretching

If the molecule is able to oscillate in the internuclear axis direction the rigid rotator approach does not strictly apply. Then the molecule is considered a non-rigid rotator where the nuclei are point masses connected by a massless spring. When such a system rotates, the centrifugal force produces an increase in the internuclear distance and thus in the moment of inertia of the molecule.

The rotational term energy of this system is given by

$$\mathrm{F(J)} = \frac{\varepsilon_{rot}}{hc} = B\mathrm{J}(\mathrm{J}+1) - D\mathrm{J}^2(\mathrm{J}+1)^2 + \ldots \tag{14}$$

$$D = \frac{4B^3}{\omega^2} \tag{15}$$

where the rotational constant B is defined as in (6). D is expressed by (15); and depends on the vibrational frequency (ω) of the molecule as a harmonic oscillator. It is always the case that $\omega >> B$, so that $D << B$. From analysis of the observed far IR spectrum, B can be obtained carrying information on the moment of inertia and internuclear distance, D is also obtained from the spectrum giving a measurement of the influence of the centrifugal force.

2.1.3.3 Vibration-rotation interaction

Up to this point, the rotational and vibrational modes of the molecule have been considered to be uncoupled. However, the structure of the infrared spectra supports the conclusion that the two modes interact. To model this interaction, consider that during vibration the internuclear distance, the moment of inertia, and the rotational constant B all change. Since the rotation period is larger than the vibration period, take a mean B value (B_v) of the rotational constant in the vibrational state v as defined by

$$B_v = \frac{h}{8\pi^2 c\mu}\overline{\left[\frac{1}{r^2}\right]} \tag{16}$$

B_v is expected to be smaller than B evaluated at the equilibrium separation r_e (B_e) as given by

$$B_e = \frac{h}{8\pi^2 c\mu r_e^2} = \frac{h}{8\pi^2 c I_e} \tag{17}$$

By means of wave-mechanical calculations [89] to a first approximation the rotational constant B_v is given by

$$B_v = B_e - \alpha_e(v+\tfrac{1}{2}) + \ldots \tag{18}$$

where α_e is a small constant, empirically has been found that α_e/B_e is slightly larger than $\omega_e x_e$. If the potential curve of the anharmonic oscillator is assumed as a Morse potential, the obtained α_e is given by

$$\alpha_e = \frac{6\sqrt{\omega_e x_e B_e^2}}{\omega_e} - \frac{6B_e^2}{\omega_e} \tag{19}$$

If very precise measurements are available higher order terms of B_v have to be included and (18) is then modified to give

$$B_v = B_e - \alpha_e(v+\tfrac{1}{2}) + \gamma_e(v+\tfrac{1}{2})^2 + \ldots \tag{20}$$

The constant D_v in expression (21) represents the influence of the centrifugal force on the vibrational state v. Here β_e is small compared with D_e which refers to the vibrationless state (compare (22) with (15)). As with the case of α_e, for a higher order power series for the potential curve, β_e is calculated by (23).

$$D_{\mathrm{v}} = D_e + \beta_e(\mathrm{v}+\tfrac{1}{2}) + \ldots \tag{21}$$

$$D_e = \frac{4B_e^3}{\omega_e^2} \tag{22}$$

$$\beta_e = D_e\left(\frac{8\omega_e x_e}{\omega_e} - \frac{5\alpha_e}{B_e} - \frac{\alpha_e^2\omega_e}{24B_e^3}\right) \tag{23}$$

Finally, the rotational term energy for a given vibrational level can be corrected for the vibrating rotator and is expressed by (24). The equation (24) includes higher power terms of J(J+1) which are exceptionally used for high resolution spectrum. The factor H_{v} is expressed by (25).

$$\mathrm{F_v(J)} = B_{\mathrm{v}}\mathrm{J(J+1)} - D_{\mathrm{v}}\mathrm{J^2(J+1)^2} + H_{\mathrm{v}}\mathrm{J^3(J+1)^3} + \ldots \tag{24}$$

$$H_{\mathrm{v}} \approx H_e = \frac{2D_e}{3\omega_e^2}(12B_e^2 - \alpha_e\omega_e) \tag{25}$$

2.1.3.4 The symmetric top molecule

To this point it has been assumed that for the nonrigid rotator the moment of inertia about the internuclear axis is zero. In reality, this is not exactly true; this moment of inertia is created by the electrons revolving about the two nuclei and is very small due to the mass of the electron. A better model for the rotation of the diatomic molecule will include a flywheel on the axis of the dumbbell; this model is a special case of a symmetric top.

The total angular momentum of a symmetric top is composed by the angular momentum corresponding to the rotation of the molecule around its center of mass and the electrons around the nuclei. According to quantum mechanics and neglecting the electron spin, the component of the total angular momentum on the internuclear axis $(\vec{\Lambda})$ can only be an integral multiple of $h/2\pi$. Thus Λ is defined as the quantum number of the angular momentum of the electrons around the internuclear axis.

The wave equation for the symmetric top can be solved rigorously (see [89]). The resulting energy levels for the vibrating symmetric top are expressed in wavenumbers by (26). Where the constant A, given by (27), takes into account the moment of inertia I_A of the electrons around the internuclear axis.

$$F_v(J) = B_v J(J+1) + (A - B_v)\Lambda^2 - D_v J^2 (J+1)^2 + H_v J^3 (J+1)^3 + \ldots \quad (26)$$

$$A = \frac{h}{8\pi^2 c I_A} \quad (27)$$

Notice that if $\Lambda = 0$, as is the case for electronic Σ states, the rotational term energy of the symmetric top is similar to that of the vibrating rotator.

2.1.3.5 Isotope effect

For isotopic molecules the vibrational and rotational structure are different among isotopes. The reduced mass of the "ordinary" molecule (μ) and the isotopic molecule "*i*" (μ^i) make the difference in both the vibrational frequency of the oscillator and the moment of inertia (I) of the rotator. To correct for this difference from the "ordinary" or most abundant composition, the parameter ρ is defined as

$$\rho = \sqrt{\frac{\mu}{\mu^i}} \quad (28)$$

The vibrational and rotational molecular constants of the corresponding term energies are corrected to a very good approximation as indicated by

$$\begin{aligned} &\omega_e^i = \rho\omega_e, \quad \omega_e^i x_e^i = \rho^2 \omega_e x_e, \quad \omega_e^i y_e^i = \rho^3 \omega_e y_e, \\ &B_e^i = \rho^2 B_e, \quad \alpha_e^i = \rho^3 \alpha_e, \quad D_e^i = \rho^4 D_e, \quad \beta_e^i = \rho^5 \beta_e \end{aligned} \quad (29)$$

2.1.4 Electronic transitions

In a diatomic molecule, the atoms are held together by the electron cloud. As is the case for atomic structure, the molecule has different electronic states depending on which orbital the bonding electrons are located. Molecular electronic transitions typically are in the visible or ultraviolet regions of the spectrum (Table 2). Electronic energy levels of molecules are obtained through detailed experimental spectroscopy. These levels can also be calculated approximately using quantum-chemical calculations. These calculations are beyond the scope of this dissertation and will not be considered. A detailed description of the electronic level structure of molecules is presented by Herzberg [86].

The energy (ε_{elec}) of the electronic state is considered to be the minimum value of the potential energy function (V). The minimum of the lowest electronic states is typically chosen to be the zero of the energy scale; this electronic state is called "ground state". The total internal energy (ε_{int}) of the molecule is given by the sum of the electronic, vibrational, and rotational components as shown in (1). In term values, cm^{-1} units, the internal energy can be expressed by

$$E = T_e + G(v) + F_v(J) \tag{30}$$

Spectral lines correspond to transitions between two molecular internal energy states. The line position or wavenumber for the transition (τ, emission or absorption) between an upper state (') and a lower state (") is given by

$$\omega_\tau = E' - E'' = (T_e' - T_e'') + (G' - G'') + (F_v' - F_v'') \tag{31}$$

For a given electronic transition, (T_e'-T_e'') is constant, but G' and G" belong to different vibrational series with different vibration constants (ω_e, $\omega_e x_e$). Similarly, F_v' and F_v'' correspond to different rotational term series with different constants (B_e, α_e).

From detailed analysis of the visible and UV spectra, the position for vibrational levels, vibrational frequencies, and anharmonicities can be derived. The rotational constants can also be derived from the spectrum in the infrared region.

To close this section, the nomenclature of electronic states is briefly considered. For atomic systems, the electronic angular momentum ($\vec{L}$) is quantized because electrons move in a spherically symmetric potential. For a diatomic molecule the potential field is axially symmetric along the internuclear axis and only the projection of $\vec{L}$ on the internuclear axis ($\vec{\Lambda}$) is quantized as

$$\left|\vec{\Lambda}\right| = \Lambda \frac{h}{2\pi} \tag{32}$$

The spectroscopic symbol for a molecular electronic level is based on the value Λ, thus for Λ = 0, 1, 2, 3, 4,… the corresponding term symbol (ξ) is Σ, Π, Δ, Φ, Γ,... . Similarly, the projection of the total electron

spin ($\vec{S}$) to the internuclear axis ($\vec{\Sigma}$) is quantized as given by (33). The quantum number Σ assumes values between $-S \le \Sigma \le S$.

$$\left|\vec{\Sigma}\right| = \Sigma\frac{h}{2\pi} \tag{33}$$

The vector addition $\vec{\Lambda} + \vec{\Sigma}$ produce $\vec{\Omega}$ which is also quantized as

$$\left|\vec{\Omega}\right| = \Omega\frac{h}{2\pi} \tag{34}$$

The term symbol (ξ) for the electronic states is given by (35). States whose electronic wave functions are symmetric (+) or antisymmetric (-) on reflection about any plane through the internuclear axis are designated by the superscript "+" or "–"

$$^{2S+1}\xi_{\Omega}^{\pm} \tag{35}$$

2.2 CO Spectrum

Deslandres [90] was the first to study the CO emission spectrum. He studied the electronic transition $A^1\Pi - X^1\Sigma^+$, known as the "fourth positive system". Since then, a number of investigations have been carried out to study the carbon monoxide spectrum in the microwave, infrared, visible, ultraviolet, and vacuum-ultraviolet regions. Huber and Herzberg [91] compiled available data for the $^{12}C^{16}O$ molecule and its ions $^{12}C^{16}O^-$ and $^{12}C^{16}O^+$ through the year 1979. The compendium cites 188 studies on the CO molecule plus over 40 identified electronic transitions. In recent years, with the availability of better laser sources and detectors, much more work has been done. This section of the chapter is not intended to be a review of all of these studies but instead to briefly present the main characteristics of the CO spectrum with special attention given to the mid-IR vibrational-rotational transitions.

2.2.1 CO electronic transitions

Carbon monoxide is the most abundant molecule after H_2 in outer space. Thus, quantitative spectroscopy of CO is important in astrophysics for study of the stellar medium, the structure of stellar

atmospheres, and thermal dynamics of molecular clouds. In other fields CO transition intensities are important for a number of applications. In chemical physics the CO laser is used to measure population distributions in chemical reactions. Outside the laboratory, the fundamental vibration-rotation bands of CO are used for atmospheric detection of CO, either for pollution control or for the study of atmospheric radical chemistry.

A detailed energy level diagram of the CO molecule is given by Herzberg [86]. This diagram shows the spacing between electronic states, their nomenclature and the designation of each band of transitions. In 1994, Morton and Noreau [92] published a compilation of 1589 electronic transitions of five isotopic species of CO in the UV range from 100 to 154.5 nm. Morton and Noreau included all the known spin-allowed bands, $A^1\Pi - X^1\Sigma^+$, $B^1\Sigma^+ - X^1\Sigma^+$, $C^1\Sigma^+ - X^1\Sigma^+$, $E^1\Pi - X^1\Sigma^+$, and $F^1\Sigma^+ - X^1\Sigma^+$ as well as the spin-forbidden bands, $a'^3\Sigma^+ - X^1\Sigma^+$, $d^3\Delta - X^1\Sigma^+$, and $e^3\Sigma^- - X^1\Sigma^+$. The spin forbidden bands are enhanced by perturbations of $A^1\Pi$. Table 3 indicates the band term symbol and the spectral range for each of the electronic transitions in this compilation. The Morton and Noreau compilation includes wavenumbers, wavelengths, and oscillator strengths for each transition.

In 2003 Eidelsberg and Rostas [93] published an atlas for CO but only included the intersystem transitions of the forbidden triplet-singlet bands. Line positions and intensities were calculated and compared with observed values. Other authors [94, 95] have performed precise measurements for some of the other CO electronic levels. Techniques applied to study the electronic transitions of carbon monoxide

Band term	Spectral range [nm]	Band Designation	Schematic included in Ref [92] ?
$A^1\Pi - X^1\Sigma^+$	111.5 – 154.4	4^{th}-Positive System	✓
$B^1\Sigma^+ - X^1\Sigma^+$	109.8 – 115.1	Hopfield-Birge Bands	✓
$C^1\Sigma^+ - X^1\Sigma^+$	101.7 – 108.9		
$E^1\Pi - X^1\Sigma^+$	102.9 – 107.7		
$F^1\Sigma^+ - X^1\Sigma^+$	100.24 – 100.28		More in Ref [93]
$a'^3\Sigma^+ - X^1\Sigma^+$	136.6 – 148.2	Triplet-Singlet Bands	✓
$d^3\Delta - X^1\Sigma^+$	136.7 – 156.2	(Enhanced by	✓
$e^3\Sigma^- - X^1\Sigma^+$	132.2 – 154.4	perturbations of $A^1\Pi$)	✓

TABLE 3 Spectral ranges for the electronic transitions in Morton and Noreau [92] 1994 compilation

include absorption [94, 95], electron impact [96], electron loss [97], and theoretical calculations [98].

2.2.2 CO transitions in the ground state ($X\,^1\Sigma^+$)

The ground state ($X^1\Sigma^+$) of CO has been extensively studied. Transition lines of CO in the ground state are observed in the photosphere of the sun and the spectrum from cooler stars. In the $X^1\Sigma^+$ state of CO, vibrational-rotational and pure rotational transitions occur. The fundamental and first three overtone bands absorb in the mid-IR (1 - 6 μm). The pure rotational transitions absorb in the far-IR region (1 – 3 mm) of the spectrum.

Guelachvili *et al.* [99] carried out an extensive study of the vibrational-rotational spectra in the ground state of CO. In their study, Guelachvili *et al.* measured about 8500 transitions, some of which were observed for the first time. This study was performed using a high-resolution Fourier transform interferometer. Numerical calculation of the molecular parameters for the CO molecule have been performed by several groups; calculations were improved by better and more precise frequency measurements that have evolved with the application of techniques such as microwave, heterodyne, laser, grating, and Fourier spectroscopy. Extremely accurate frequency measurements of the CO ground state had been performed using microwave [100] and IR heterodyne methods [101, 102].

HITRAN (HIgh-resolution TRANsmission) database [44] is a compilation of spectroscopic parameters for 38 molecules including carbon monoxide. HITRAN includes 4447 lines of 6 isotopomers of CO in the spectral range 1.18 μm to 3.33 mm. This coverage includes the fundamental ($\Delta v = 1$) and three overtone bands ($\Delta v = 2$, 3, and 4) of CO in its ground state. Figure 1 shows the intensity of the transitions in these bands as retrieved from HITRAN at 1000 K. The far-IR lines that correspond to pure rotational transitions in the ground state $X^1\Sigma^+$ are provided by HITRAN, but are not shown in Fig. 1.

The HITRAN compilation first appeared in 1973 [103]. Carbon monoxide bands in that early compilation were based on the work by Young [104]. Young calculated the spectra of the fundamental and first two overtone bands. New transitions and spectroscopic parameters for the compilation are incorporated periodically as new or improved data becomes available. The 1996 release of HITRAN

[105] included new calculations for intensity, position and lower state energies of the fundamental and overtone bands. The current version of HITRAN 2000 [44] did not include changes for the CO molecule compared to the 1996 edition.

In the HITRAN compilation, line positions are calculated through the Dunham parameters while intensities are computed directly from the dipole moment matrix elements. Dunham [106] carried out a very careful study of the vibration-rotation interactions. He expressed the term values G(v) and $F_v(J)$ in the form of a power series

$$(\mathrm{G}+\mathrm{F_v})^i = \sum_{k,l} Y_{kl}^i (\mathrm{v}+\tfrac{1}{2})^k (\mathrm{J}^l)(\mathrm{J}+1)^l \tag{36}$$

the Y_{kl}^i terms are known as the Dunham parameters; the index "*i*" makes reference to the isotopic species "*i*" with a reduced mass μ^i. In the case of a multi-isotope molecule such as CO, the mass-independent parameters (U_{kl}) are related to the Dunham parameters through

$$U_{kl}(\mu^i)^{-(k/2)-l} = \frac{Y_{kl}^i}{1+m_e((\Delta_{kl}^{\mathrm{a}}/m_{\mathrm{a}})+(\Delta_{kl}^{\mathrm{b}}/m_{\mathrm{b}}))} \tag{37}$$

where Δ^{a}_{kl} and Δ^{b}_{kl} are known as the mass-scaling coefficients associated to atoms a and b with masses m_{a} or m_{b}.

Thus the relations between the Dunham mass independent coefficients and the spectroscopic constants are given by

$$\left|\begin{array}{ll} \omega_e^i = Y_{10} & \omega_e x_e^i = -Y_{20} \\ \omega_e y_e^i = Y_{30} & B_e^i = Y_{01} \\ \alpha_e^i = -Y_{11} & D_e^i = -Y_{02} \\ \beta_e^i = -Y_{12} & H_e^i = Y_{03} \end{array}\right. \tag{38}$$

It was found by Dunham that there are some very small deviations, the corrections are usually much less than one in one thousand and are usually negligible.

Many research groups had derived mass-independent Dunham coefficients from accurate microwave and infrared measurements of the ground state for various CO isotopes. Guelachvili *et al*. [99] derived 25 Dunham coefficients and 10 mass scaling factors for seven isotopic species of CO. Le Floch [107] noticed that the Dunham parameters available in 1991 [99, 101, 102] did not reproduce observed

data for the ground state of the $^{12}C^{16}O$ molecule. Le Floch calculated more refined Dunham parameters for the ground state from all available frequency measurements, and also recalculated the molecular constants with this new set of Dunham parameters. Farrenq *et al.* [108] recommended a set of Dunham coefficients for CO transitions with high rotational excitation (high J values). By 1992, Authier *et al.* [109] noticed that the Dunham parameters of Farrenq *et al.* [108] did not reproduce very accurate heterodyne measurements of the first overtone band and microwave transitions. Authier *et al.* re-fitted the mass-independent Dunham coefficients to a complete set of existing high quality microwave and heterodyne frequency measurements of six isotopic species of CO in the ground state.

Calculating the spectroscopic parameters also involves calculation of the transition strength through the fit of the dipole moment. On 1978, Kirby-Docken and Liu [110] calculated the dipole moment; they obtained vibration-rotation wave functions by numerically solving the radial SWE assuming a Rydberg-Klein-Rees (RKR) potential derived from the spectroscopic constants for the ground state of CO. The matrix elements are formed by integrating the calculated dipole moment function between two vibrational eigenfunctions, thus the line absorption oscillator strength is directly computed.

Chackerian and Tipping [111] computed the dipole moment matrix elements for the five most abundant isotopes of CO. They claimed to have incorporated the most recent, accurate, and extensive intensity measurements for any heteronuclear diatomic molecule. And therefore, they propose that some of the lines in the fundamental band of $^{12}C^{16}O$ can be used as laboratory standards for intensity measurements.

In 1993, Hure and Roueff [112] reported the oscillator strengths for vibrational-rotational transitions of CO in the fundamental and the three first overtone bands. They found the dipole moment matrix elements were changed in magnitude by approximately 10% due to change in the values of the dipole moment function. This difference produces a significant 20% discrepancy in the absorption oscillator strength of the 21600 lines used. The current transition list for CO in the HITRAN database has been adapted from Goorvitch [113] compilation. Goorvitch used the expectation values of the dipole matrix elements experimentally determined by Chackerian and Tipping [111] since they are preferred over the calculated values by Hure and Roueff [112]. Goorvitch calculations for line positions are based on the

Dunham parameters by Farrenq *et al.* [108]. Rotational transition lines in the current HITRAN database were updated based on line positions by Varberg and Evenson [114].

Nolt *et al*. [100] produced far-IR radiation of high spectral purity by two mixing techniques. Second- and third-order (respectively, two- and three-wave) mixing was performed on a metal-insulator-metal (MIM) diode producing 100 to 500 nW of far-IR radiation for the second-order mixing scheme. Nolt *et al*. studied R ($\Delta J = 1$) transitions in the ground state (v = 0) up to J = 33 in the far-IR region 74.9 μm to 2.63 mm. Recently, Varberg and Evenson [114] accurately measured carbon monoxide rotational spectrum. Their absorption measurements were performed with a tunable far-IR spectrometer; their equipment was similar to Nolt *et al.* using a MIM diode with two-wave mixing. They calculated transition frequencies which are an order of magnitude more accurate than those reported by Nolt *et al.*

Table 4 shows the molecular constants calculated from the Dunham coefficients for $^{12}C^{16}O$ published by Farrenq *et al.* [108]. HITRAN uses the parameters from Farrenq *et al.* to compute the molecular constants. Table 4 also includes the molecular constants as published by Le Floch [107].

	Farrenq *et al.* [108]	Le Floch [107]
ω_e	2169.81266	2169.75589
$\omega_e x_e$	13.28787	13.28803
$\omega_e y_e$	0.0104110	0.0104109
B_e	1.931281	1.931602
α_e	0.01750439	0.01750513
D_e	6.12161×10^{-6}	6.12159×10^{-6}

TABLE 4 Molecular constants [cm^{-1}] for the ground state transitions of $^{12}C^{16}O$. Constants in column Farrenq *et al.* [108] have been calculated from the Dunham parameters given by (38) and constants for m_e and μ^{12C16O} given in ref. [108]

CHAPTER III

THEORETICAL BACKGROUND

3.1 Quantitative Absorption Spectroscopy

The energy level structure of CO was reviewed in Chapter II. Specifically, it was seen that carbon monoxide vibration-rotation transitions occur in the mid-IR, with the strongest being the transitions in the fundamental band ($\Delta v = 1$) in the 4.2 – 5.6 μm region. Physical processes through which transitions between energy levels occur in a molecule are collisions and radiative transitions such as spontaneous emission, stimulated emission, and stimulated absorption. To produce stimulated absorption, an incident photon must have the exact frequency ν_τ [Hz] given by

$$\nu_\tau = c\,\omega_\tau \tag{39}$$

where c [cm/s] is the speed of light in vacuum and ω_τ [cm^{-1}] is the wavenumber of the transition between levels η'' (v'',J'') and η' (v',J') as expressed by (31). In practice, light with frequency ν_τ from a given source (i.e., laser) is sent through the absorbing media. The amount of absorbed energy can be measured and theoretically predicted, relating the absorbed energy to the molecular concentration in the beam path.

This section is concerned with the theoretical description of the absorption process. Relevant relations in quantitative absorption spectroscopy are presented and closely follow the discussion by Lucht *et al.* [115]. A rigorous development can be found in Penner [116] which has been also extensively used in the preparation of the following sub-sections.

3.1.1 Beer's law of absorption

The Bouguer-Lambert law of absorption is derived from thermal radiation considerations. Specifically for absorbing liquids or gases, and because of a change in nomenclature, the Bouguer-Lambert law is referred to as Beer's law of absorption. Beer's law (40), describes the attenuation of spectral intensity ($I_\omega(z)$, [W/m^2]) that occurs when radiation travels through matter. Radiation is considered to move in the z-direction and the interaction distance (L, [cm]) is known as the path length.

$$T_\omega \equiv \frac{I_\omega(L)}{I_\omega(0)} = \exp(-\int_0^L k_\omega dz) \tag{40}$$

In optical absorption experiments, it is customary to determine either the spectral absorptivity (A_ω) or the spectral absorbance (α_ω). The spectral absorptivity (A_ω) is related to the spectral transmissivity (T_ω) by

$$A_\omega + T_\omega = 1 \tag{41}$$

Assuming uniform conditions along the line of sight, the spectral absorption coefficient (k_ω) is constant in the z-direction and the absorptivity can be expressed by

$$A_\omega \equiv \frac{I_\omega(0) - I_\omega(L)}{I_\omega(0)} = 1 - \exp(-k_\omega L) \tag{42}$$

The spectral absorbance (α_ω) is defined by

$$\alpha_\omega \equiv -\ln\left(\frac{I_\omega(L)}{I_\omega(0)}\right) = k_\omega L \tag{43}$$

The spectral absorption coefficient (k_ω, [cm^{-1}]) accounts for the strength (S_τ^*, [cm^{-2}/atm]) and line profile ($\phi(\omega)$, [cm]) of the molecular energy transition. When several transitions overlap and thus absorb, the spectral absorption coefficient is obtained by adding the contributions ($k_{\omega,\tau j}$) from each transition τ of the absorbing species "j" as expressed by

$$k_\omega = \sum_j \sum_\tau k_{\omega,\tau j} \tag{44}$$

where $k_{\omega,\tau j}$ is given by

$$k_{\omega,\tau j} = S_\tau^* \cdot P \cdot X_j \cdot \phi_\tau(\omega) \tag{45}$$

The spectral absorption coefficient is a function of the total pressure of the medium (P, [atm]) and the mole fraction of the (X_j) of the absorbing species. Another common set of units for line strength is [cm^{-1}/molecule cm^{-2}] (S_τ), this number-density dependent version is used by HITRAN. The conversion between S_τ and S_τ^* is given by

$$S_\tau^*[\mathrm{cm}^{-2}/\mathrm{atm}] = \frac{S_\tau[\mathrm{cm}^{-1}/\mathrm{molecule}\cdot\mathrm{cm}^{-2}]\cdot n_j[\mathrm{molecule}/\mathrm{cm}^3]}{P_j[\mathrm{atm}]} \tag{46}$$

where n_j [molecule/cm^3] is the number density and P_j [atm] is the partial pressure of the absorbing species. The number density can be calculated using the ideal gas law

$$n_j = \frac{X_j P}{k_B T} \tag{47}$$

where k_B is the Boltzmann constant (k_B = 1.3806x10^{-23} J/K or 1.3626x10^{-22} atm·cm^3/K) and T [K] is the temperature. In this unit convention, the spectral absorption coefficient ($k_{\omega,\tau j}$) for transition τ of the absorbing species "*j*" is given by

$$k_{\omega,\tau j} = S_\tau\, n_j\, \phi_\tau(\omega) \tag{48}$$

The line strength of the transition is independent of ω and is related to the probability of the transition (Einstein coefficients) and the population in the lower quantum state, which depends on the Maxwell-Boltzmann distribution or temperature. The line strength of a transition τ between lower level η" (v",J") and upper level η' (v',J'), is given in [113] as

$$S_{\eta''\eta'} = \frac{\pi e^2}{m_e c^2} g_{J''} f_{\eta''-\eta'} \frac{\exp\left[-c_2 \mathrm{E(v''J'')}/T\right]}{Q(T)}\left[1-\exp(-c_2\omega_{\eta''\eta'}/T)\right] \tag{49}$$

where E(v",J") is the lower state term energy as defined by (30), $Q(T)$ is the partition function, and the constants in (49) are given by

$$\frac{\pi e^2}{m_e c^2} = 8.8523\times10^{-13}\ \mathrm{cm/molecule} \tag{50}$$

$$c_2 = \frac{hc}{k_B} = 1.438\ \mathrm{K\cdot cm} \tag{51}$$

the statistical weight ($g_{J''}$) of the lower state is given by

$$g_{J''} = 2J''+1 \tag{52}$$

and the absorption oscillator strength ($f_{\eta''-\eta'}$) is related to the Einstein A-value for spontaneous emission ($A_{\eta'-\eta''}$) by (53) and (54)

$$g_{J''} f_{\eta''-\eta'} = -g_{J'} f_{\eta'-\eta''} \tag{53}$$

$$g_{J'} f_{\eta'-\eta''} = -\frac{m_e c}{8\pi^2 e^2 \omega_{\eta'-\eta''}} (2J'+1) A_{\eta'-\eta''} \tag{54}$$

3.1.2 Broadening processes

Ideally, a transition between energy levels is monochromatic i.e., it only absorbs or emits photons with frequency ν_τ, given by (39). As opposed to a sharp line in frequency, transitions are broadened so they have a linewidth. Figure 2 shows a schematic of a transition profile ($\phi(\omega)$) with center at $\omega_{o\tau}$ [cm^{-1}]; $\Delta\omega$ is the full width at half maximum (FWHM), which is a meaningful indication of the linewidth. The transition profile function $\phi(\omega)$ is normalized according to

$$\int_{-\infty}^{+\infty} \phi(\omega)\, \mathrm{d}\omega = 1 \tag{55}$$

thus, $\phi(\omega)$ represents a probability distribution function for the line.

There are several mechanisms for line broadening and they can be classified as "inhomogeneous" or "homogeneous" broadening. Inhomogeneous broadening indicates that an assembly of identical molecules does not have a similar frequency response. Inhomogeneous broadening processes include Doppler broadening, inhomogeneous dc magnetic fields, and impurities in the media. Homogeneous broadening indicates that the broadening mechanism acts similarly on all molecules in the assembly; natural, Stark, and collisional or pressure broadening are examples of these mechanisms.

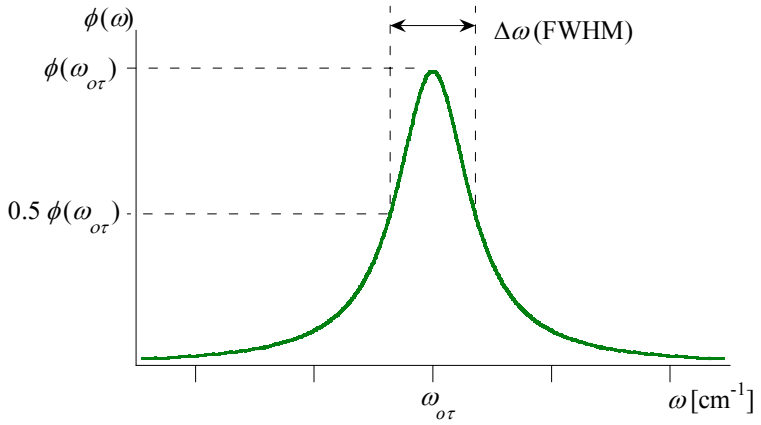

FIGURE 2 Transition profile $\phi(\omega)$

The kinetic energy of a collection of gas molecules is characterized by a Mawell-Boltzmann velocity distribution. Thus the transition line is broadened because the beam frequency ($\omega_{o\tau}$) will appear Doppler-shifted (to value ω) to a molecule moving in a direction along the beam axis. Since the velocity distribution is Maxwellian for a gas in thermal equilibrium, the Doppler broadening is described for a Gaussian function $\phi_D(\omega)$

$$\phi_D(\omega) = \sqrt{\frac{\ln 2}{\pi}} \frac{2}{\Delta\omega_D} \exp\left[-4 \ln 2 \frac{(\omega - \omega_{o\tau})^2}{\Delta\omega_D^{\,2}} \right] \tag{56}$$

where $\Delta\omega_D$ is the Doppler full width (FWHM) given by (57). The reduced form of $\Delta\omega_D$ [cm^{-1}], (58), is more convenient.

$$\Delta\omega_D = 2\sqrt{\frac{2 \ln 2 \, k_B T}{Mc^2}} \omega_{o\tau} \tag{57}$$

$$= 7.162 \times 10^{-7} \, \omega_{o\tau} \sqrt{\frac{T}{M}} \tag{58}$$

where M is the molecular weight in grams per mole [g/mol], $\omega_{o\tau}$ is the wavenumber [cm^{-1}] of the center of the transition, T is temperature in Kelvin degrees [K]. The Doppler linewidth depends only on temperature. Temperature can be determined from the spectral line shape if the line is predominantly Doppler broadened. As would be the case for high temperatures and low pressures.

Collisional broadening is another important broadening mechanism for gases at atmospheric pressure. When molecules within a gas sample collide with each other there is an energy exchange that leads to the shortening of the lifetime of the molecule in its energy level. Since the energy state of the molecule has changed, its interaction with the electromagnetic field is altered in the sense that collisions interrupt the phase of the field as seen by the molecule therefore broadening the frequency bandwidth of the field with respect to the molecule. By increasing the pressure of the sample the molecular density will increase and collisions are more likely to occur. The total response of the molecular sample determines the line shape of the transition and statistically represents the averaged effect of the distribution of collision times. Lorentz was the first to perform the calculation thus the resulting line shape $\phi_C(\omega)$ known as Lorentzian shape, is given by

$$\phi_C(\omega) = \frac{\Delta\omega_C}{2\pi} \frac{1}{(\omega - \omega_{o\tau})^2 + (\Delta\omega_C / 2)^2} \tag{59}$$

where $\Delta\omega_C$ [cm^{-1}] is the collision broadened linewidth FWHM expressed by

$$\Delta\omega_C = \frac{1}{\pi c}(Z_{\eta'} + Z_{\eta''}) \tag{60}$$

where Z represents the dephasing collision frequency for levels η' and η". The FWHM of collision broadening is modeled by

$$\Delta\omega_C = 2\left(\frac{T_{ref}}{T}\right)^n P \sum_b \gamma^o_{a-b} X_b \tag{61}$$

where $\gamma^o_{a\text{-}b}$ [cm^{-1}/atm] is the half-width at half-maximum (HWHM) coefficient for collisional broadening of species a by species b at reference temperature (T_{ref}, [K]), P [atm] is the total gas mixture pressure, T [K] is the gas temperature, X_b is the mole fraction of species b in the mixture, the exponent "n" is the coefficient for temperature dependence of the HWHM coefficient, and b represents every species in the gas mixture including the absorber species a. Expression (61) takes into account that the absorber molecules can collide each other (self- or Holtsmark-broadening, $\gamma^o_{a\text{-}a}$) or with other kinds of molecules (Lorentz broadening, $\gamma^o_{a\text{-}b}$ for b≠a).

When $\Delta\omega_D \approx \Delta\omega_C$ the transition broadening cannot be characterized as pure collision or pure Doppler broadened; then both effects play a role in determining the line shape of the transition. The Voigt line shape $\phi_V(\omega)$ is the convolution of the Gaussian and Lorentzian shapes. And is given by

$$\phi_V(\omega) = \frac{2}{\Delta\omega_D}\sqrt{\frac{\ln 2}{\pi}}V(a,x) \tag{62}$$

where $V(a,x)$ is called the Voigt function and is given by (63); x represents the distance from the line center ($\omega_{o\tau}$) normalized by the Doppler width. The Voigt parameter (a) is an indication of the dominant mechanism for broadening; for $0 < a < 1$ the Voigt profile becomes Gaussian representing Doppler broadening. The parameter a increases as pressure increases. For $a \approx 2$ the Voigt shape is mainly Lorentzian.

$$V(a,x) = \frac{a}{\pi}\int_{-\infty}^{+\infty}\frac{\exp(-y^2)}{a^2+(x+y)^2}\mathrm{d}y \tag{63}$$

$$a = \sqrt{\ln 2}\,\frac{\Delta\omega_C}{\Delta\omega_D} \tag{64}$$

$$x = 2\sqrt{\ln 2}\,\frac{\omega-\omega_{o\tau}}{\Delta\omega_D} \tag{65}$$

The Voigt function can be evaluated using numerical routines developed by Armstrong [117] or Humlicek [118]. The transition represented in Fig. 2. is the Voigt profile (a = 7.95) for the carbon monoxide P(19) fundamental band transition at 2064.3969 cm^{-1}. To generate the profile in Fig. 2., it was assumed that a mixture 1000 ppm CO with buffer gas of N_2 was at room temperature (298 K) and at a pressure of 46.26 kPa. The profile shows wings that vanish slowly; this is a characteristic of a Lorentzian shape. For the same CO transition to be primarily Doppler broadened, the temperature of the mixture would have to be increased significantly; for T = 3050 K the Voigt parameter a = 0.5.

3.1.3 Concentration measurements

The problem of determining the concentration X_a of species a by optical absorption can be approached using three different schemes: narrow band source, integrated absorbance, and full parameter fit.

3.1.3.1 Absorption using a narrow band source

When the light source has a very narrow linewidth compared to the transition linewidth, the concentration of the absorbing species can be directly determined. Diode lasers are sources with typical linewidths on the order of 100 MHz or less.

The spectral absorptivity for a narrow source ($A_{\omega,NS}$) can be found by integrating over the source profile; using (42) to (48) this can be expressed by

$$A_{\omega,NS} = \frac{I_S(0) - I_S(L)}{I_S(0)} = \int_{\omega 1}^{\omega 2} \phi_S(\omega) \left\{1 - \exp\left[-S_\tau\, n_j\, L\, \phi_V(\omega)\right]\right\} \mathrm{d}\omega \tag{66}$$

where the integration limits (ω_1, ω_2) cover the full source line shape thus $\phi_S(\omega_1) = \phi_S(\omega_2) = 0$. The molecular transition profile ($\phi_V(\omega)$) is given by a Voigt shape. Under the assumption of a source with narrow linewidth compared to the molecular linewidth

$$\phi_V(\omega) = \phi_V(\omega_{oS}); \qquad \text{if } \Delta\omega_S << \Delta\omega_V \tag{67}$$

the molecular transition profile can be regarded as constant across the source linewidth.

Substituting (67) into (66) gives the spectral absorptivity for narrow source

$$A_{\omega,NS} = 1 - \exp\left[-S_\tau\, n_j\, L\, \phi_V(\omega_{oS})\right] \tag{68}$$

Experimentally, the source spectral intensity has to be measured before ($I_S(0)$) and after ($I_S(L)$) transmission through the absorbing media. To perform these measurements two different detectors can be used. $I_S(L)$ is easily recorded by locating the appropriate detector at position L after the absorbing media. $I_S(0)$ can be detected either by removing the absorbing media from the beam path or by detuning the laser frequency to ω_{wing} were $\phi_V(\omega_{wing}) = 0$ and no absorption of the laser energy occurs.

To compute the right hand side of (68), the transition profile ($\phi_V(\omega)$) should be calculated from knowledge of temperature ($\Delta\omega_D$), pressure, and medium composition ($\Delta\omega_C$). Since the medium composition is not known *a priori*, the use of libraries is necessary to implement this technique.

3.1.3.2 Integrated absorbance area

For a narrow source, the spectral absorption coefficient (k_ω) is constant over the laser bandwidth. If the laser light is tuned over the entire transition profile the actual shape of the absorption profile will be duplicated. Integrating the area (σ) under the profile and using (43), (48), and (55) gives the following expression for the absorbing species concentration

$$\begin{aligned}\sigma &= \int \alpha_\omega \mathrm{d}\omega = \int k_\omega L \,\mathrm{d}\omega \\ &= \int -\ln\left(\frac{I_\omega(L)}{I_\omega(0)}\right)\mathrm{d}\omega = S_\tau \; n_j \; L\end{aligned} \tag{69}$$

The absorption line shape is generally described by a Voigt profile, and a fit to the absorbance profile may improve the numerical calculation of the area. To implement this scheme, the temperature of the absorbing media must be known. The line strength is a function of the temperature as described by (49). Figure 3 shows the temperature dependence of three CO fundamental band transitions R(23), R(11), and P(19) at 2224.7127, 2186.6390, and 2064.3969 cm^{-1} respectively. Figure 3b shows the relative sensitivity of the line strength to temperature for these transitions. The sensitivity of each line is different. Therefore the transition should be carefully chosen to minimize temperature sensitivity when temperature of the medium is not accurately known.

Two-line thermometry is a technique for accurate temperature measurements using the integrated absorbance scheme. When possible, the laser frequency is scanned over two contiguous absorption lines (τ_1 and τ_2). Thus the absorbance spectrum will consist of two lines with Voigt profiles. Fitting of the spectrum will allow the determination of each Voigt parameter (a_1 and a_2) and thus numerical integration of the area under each individual transition is possible. Applying (69) to each transition and taking the ratio of both areas results in

$$\frac{\sigma_{\tau 1}}{\sigma_{\tau 2}} = \frac{S_{\tau 1}(T)}{S_{\tau 2}(T)} \tag{70}$$

substituting (49) into (70) and rearranging yields

$$\frac{\sigma_{\tau 1}}{\sigma_{\tau 2}} = \frac{S_{\tau 1}(296)}{S_{\tau 2}(296)} \cdot \frac{\exp\left[-c_2 \mathrm{E}_{\eta'' 1}/T\right]}{\exp\left[-c_2 \mathrm{E}_{\eta'' 2}/T\right]} \cdot \frac{1-\exp\left[-c_2 \omega_{\tau 1}/T\right]}{1-\exp\left[-c_2 \omega_{\tau 2}/T\right]} \tag{71}$$

where temperature is the only undetermined parameter. The line strength evaluated at 296 K [$S_\tau(296)$, (cm^{-1}/molecule cm^{-2})] is available from the HITRAN database.

Two-line spectroscopy is dependent on the availability of two transitions within the scanning range of the laser. Also, spectral interference from other absorbed molecules is not desired although Wang *et al.* [54] have taken advantage of two-line thermometry among two CO_2 lines and then relating this temperature measurement to determine the concentration of carbon monoxide.

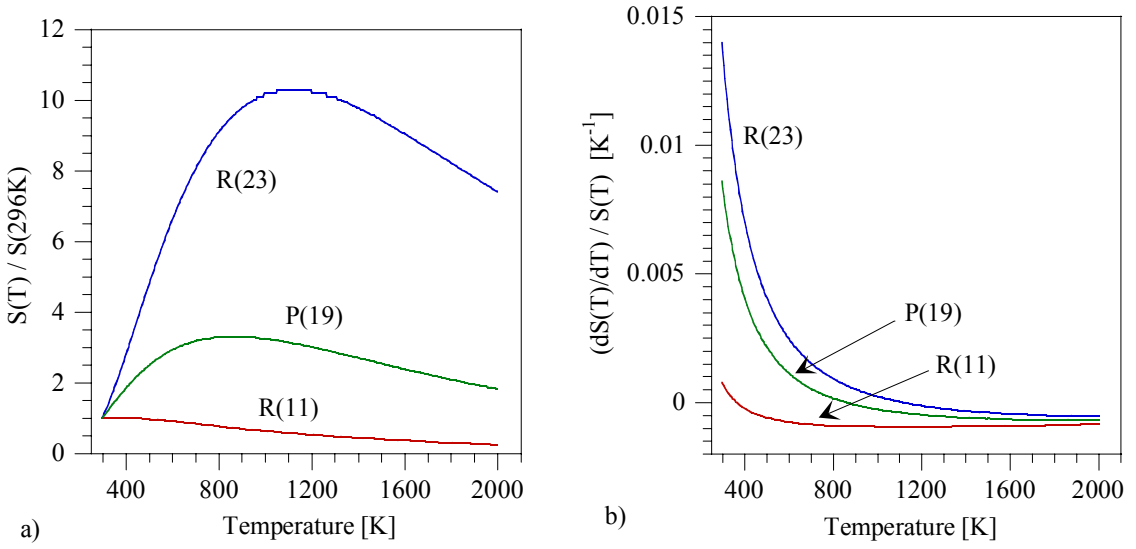

FIGURE 3 Temperature dependence of the line strength for three CO fundamental band transitions R(23), R(11), and P(19) at 2224.7127, 2186.6390, and 2064.3969 cm^{-1}. a) Strength normalized to the value at 296K. b) Temperature sensitivity for the same transitions

3.1.3.3 Full parameter fit of absorption trace

When performing measurements in flames or combustion exhaust streams, temperature, pressure, and/or the gas composition may not be known. To apply optical absorption for concentration measurements a robust detection scheme is required. When scanning a narrow linewidth source over an absorption transition, the line shape of the transition is reproduced. The spectral absorptivity (42) can be determined from the measured detector response to radiation. As given by equations (42) to (63) the specific experimental conditions (i.e., temperature, pressure, path length, and gas mixture composition) and the particular spectroscopic characteristic of each transition (i.e., transition position, line strength, lower state term energy, collisional broadening coefficients, and their temperature dependence coefficient) will result in a distinctive spectral absorptivity profile.

Equations (42) to (63) define the function or model that describes spectral absorptivity. To proceed with a full parameter fit, it is necessary to set a goodness-of-fit criterion and to define the rules to select parameters through iterations. In any parametric fit to a given model the main problem is to assure that the best-fit parameters set indicate a global rather than a local minimum of the model. In combustion problems to which optical absorption can be applied for species concentration the model parameters have a narrow domain i.e., pressure in flames is usually 1 atm, and the temperature is approximately known. Thus a full parameter fit for the absorption profile is usually feasible.

In this model there are two distinguishable sets of parameters. The spectroscopic parameters are given for each transition in the scanning range. The HITRAN database provides these parameters. A detailed treatment of them will be the topic of the following section. The second set of parameters is formed by the experimental conditions. The path length is usually known so this parameter is fixed for the fit, and sometimes pressure and/or temperature are fixed. The gas mixture composition needs to be determined to estimate the collisional broadening of the absorber species transition. Since the composition of the sample media is normally unknown, a "Gamma Factor" (GF_a) is introduced in (61). Equation (72) includes the gamma factor (GF_a) substituting for the summation that accounts for other non-absorbing molecules in the gas sample. This gamma factor (GF_a) is a fitting parameter for the model.

$$\Delta\omega_C = 2 \cdot P \cdot GF_a \cdot \left(\frac{T_{ref}}{T}\right)^n \left[\gamma^o_{a-a} X_a\right] \tag{72}$$

The fitting procedure consists of varying the unknown parameters within their domain to obtain the theoretical absorption spectrum ($A_{\omega,CALC}$). This calculated spectrum is compared with the experimental absorption spectrum ($A_{\omega,EXP}$) using

$$\chi^2 = \sum_{\omega=\omega 1}^{\omega 2} \left[A_{\omega,EXP}(\omega) - A_{\omega,CALC}(\omega : L, T, P, X_a, GF_a)\right]^2 \tag{73}$$

Equation (33) establishes the goodness-of-fit criterion commonly known as "least squares criterion." The best-fit to the experimental data is found when the χ^2 criterion is minimized.

The full-parameter fit strategy has been adopted to interpret the experimental results of the present work. A computer code "Direct_Absorption" has been specifically written for this purpose. The absorption fitting code is based in the fundamentals just outlined. A detailed description of this data processing code is given in Appendix A.

Depending on the particular experimental conditions for our measurements, some parameters were known and fixed. The remaining parameters were adjusted in two steps. An evolutionary algorithm [119] was performed for 100 generations with 100 sets per generation. Subsequently the non-linear Levenberg-Marquardt method [120, 121] was applied and initialized by the best-parameters set found by the evolutionary routine. This scheme is robust but computationally intensive.

The spectral region of interest in this project is the 4.4 - 5.2 μm where the fundamental band of carbon monoxide is located. In this region, spectral interference from carbon dioxide (CO_2) is not desired but frequently encountered. To account for this interference, the code was designed to calculate the total spectral absorption from two absorbing species: CO and CO_2. The contribution of both absorber molecules is accounted for by the spectral absorption coefficient (k_ω) in (44). Therefore, the equations in the model are applied independently to each absorber under the same experimental conditions but with the appropriate spectral parameters set for each transition. Because of the parallelism in the treatment of each

absorber molecule, further consideration and discussion will make reference only to CO, the species of interest in this project.

3.2 HITRAN Database

The HITRAN database [44, 103, 105] has evolved over the last three decades. The current release of the database includes spectroscopic parameters for the most abundant isotopes for 38 species, among them carbon monoxide. In the scope of implementing a full parameter fit, the HITRAN database provides the fundamental spectroscopic parameters required, and the "Direct_Absorption" code developed was designed to closely work with the HITRAN database. Table 5 summarizes the parameters retrieved from the database by the absorption fitting code.

Parameter	Definition	Units	Equation
$\omega_{o\tau}$	Central transition wavenumber	[cm^{-1}]	(57) (65) (74)
$S_\tau(296)$	Transition strength at 296 K	$\left[\frac{cm^{-1}}{molecule\, cm^{-2}}\right]$	(74)
$\gamma^o_{CO\text{-}air}$	Air-broadened half-width at half-maximum (HWHM) coefficient at 296 K	[cm^{-1}/atm]	(61) (76)
$\gamma^o_{CO\text{-}CO}$	CO self-broadened HWHM coefficient at 296 K	[cm^{-1}/atm]	(61) (72) (76)
$E_{\eta''}$	Transition lower state (v", J") term energy	[cm^{-1}]	(49) (74)
n	Coefficient for temperature dependence of $\gamma^o_{CO\text{-}Air}$	--	(61) (72) (76)

The subscript τ indicates transition between lower and upper levels η"-η' defined by quantum numbers (v", J") and (v', J') respectively.

TABLE 5 Transition dependent parameters retrieved from HITRAN and used by the developed absorption fitting code

The line-by-line format adopted in HITRAN is designed to contain the fundamental quantities for each transition. The list is arranged by the transition wavenumber. The other parameters are specific to each transition.

HITRAN uses 296 K as the temperature reference (T_{ref}). The transition line strength in HITRAN is defined at 296 K. Using (49), the temperature correction can be carried out as recommended by Rothman *et al.* [105]

$$S_\tau(T) = S_\tau(296)\cdot\frac{Q(296)}{Q(T)}\cdot\frac{\exp\left[-c_2 \mathrm{E}_{\eta''}/T\right]}{\exp\left[-c_2 \mathrm{E}_{\eta''}/296\right]}\cdot\frac{1-\exp\left[-c_2\omega_{o\tau}/T\right]}{1-\exp\left[-c_2\omega_{o\tau}/296\right]} \tag{74}$$

where the third term on the right of (74) accounts for the ratio of Boltzmann populations and the fourth term for the effect of stimulated emission. $Q(T)$ is the total internal partition function. HITRAN uses the parameterization of Gamache *et al.* [122]:

$$Q(T) = \mathrm{a} + \mathrm{b}T + \mathrm{c}T^2 + \mathrm{d}T^3 \tag{75}$$

where coefficients a, b, c, and d for the isotopes of CO have been determined for the temperature ranges: $70 \le T \le 500$, $500 \le T \le 1500$, and $1500 \le T \le 3005$ [K]. These coefficients are retrieved from HITRAN.

The HWHM coefficients for self- and air-broadening ($\gamma^o_{CO\text{-}air}$, $\gamma^o_{CO\text{-}CO}$ [cm^{-1}/atm]) are given by HITRAN at the reference temperature (T_{ref} = 296 K) along with the coefficient for temperature dependence. Correction for temperature is included in (72). Rothmann *et al.* [105] suggest a similar expression to correct for temperature in which they include the air-broadening effect. For historical reasons, the absorption fit code uses (76) to compute the collisional broadening FWHM.

$$\Delta\omega_C = 2\cdot P\cdot GF_{CO}\cdot\left(\frac{296}{T}\right)^n\left[\gamma^o_{CO-CO}X_{CO} + \gamma^o_{CO-air}(1-X_{CO})\right] \tag{76}$$

Notice that (76) is a modification of (72) that includes the GF_{CO} factor, in which the absorber species (a) is carbon monoxide and the gas sample is considered a binary mixture of CO and air. An assessment of the gamma factor (GF_{CO}) as introduced in (76) was made in preliminary testing of the sensor and is presented in Chapter V.

Table 6 reproduces the spectroscopic parameters retrieved from HITRAN [44] for some of the IR transitions in the fundamental band of $^{12}C^{16}O$ used through the course of this project.

	$\omega_{o\tau}$ [cm^{-1}]	[μm]	$S_\tau(296)$ [cm^{-1}/molecule cm^{-2}]	$\gamma^o_{CO\text{-}air}$ [cm^{-1}/atm]	$\gamma^o_{CO\text{-}CO}$ [cm^{-1}/atm]	$E_{\eta''}$ [cm^{-1}]	n
R(25)	2230.5258	4.483	5.895×10^{-21}	0.0440	0.0500	1247.0592	0.69
R(24)	2227.6386	4.489	9.011×10^{-21}	0.0445	0.0505	1151.3150	0.69
R(23)	2224.7127	4.494	1.350×10^{-20}	0.0450	0.0510	1059.3718	0.69
R(20)	2215.7044	4.513	4.018×10^{-20}	0.0480	0.0537	806.3828	0.69
R(11)	2186.6390	4.573	3.314×10^{-19}	0.0579	0.0634	253.6672	0.69
P(18)	2068.8469	4.833	6.601×10^{-20}	0.0522	0.0578	656.7892	0.69
P(19)	2064.3969	4.844	4.880×10^{-20}	0.0513	0.0565	729.6774	0.69
P(13)*	2064.5839	4.843	1.282×10^{-23}	0.0574	0.0623	2489.7831	0.69

* This is a hot-band transition from v"=1 to v'=2 and it can only be detected at high temperatures.

TABLE 6 Spectroscopic parameters retrieved from HITRAN database [44] for some selected transitions in the fundamental band of $^{12}C^{16}O$. These transitions (τ) correspond to v" = 0 to v' = 1 with $\Delta J = \pm 1$

3.3 Nonlinear Optics

In Chapter I, nonlinear optical frequency conversion was regarded as a means to extend the wavelength coverage of semiconductor sources. The advantages and applications of this technique to the mid-IR detection and spectroscopic study of important molecules were also reviewed in Chapter I. Here nonlinear conversion is reviewed with special emphasis on the generation of mid-IR radiation by means of Difference Frequency Mixing (DFM). Texts by Boyd [123] and Shen *et al.* [124] contain detailed treatments of the theory of DFM. Mid-IR generation by DFM is reviewed by Chen *et al.* [75] and Fischer and Sigrist [125] and documentation from Gemfire Corporation (Bamford [126]) has also been used in this discussion.

The optical properties of matter are altered when exposed to intense electromagnetic radiation such as laser light. For weak laser irradiation, the electrons in the media oscillate at the same frequency as laser field. However, when the strength of the field is intense, the electrons do not follow the oscillation exactly, thus affecting the polarization of the material and resulting in new frequencies. The electric polarization $(\vec{P})$ induced by the applied electric field $(\vec{E})$ can be expressed by a power series in $\vec{E}$. Equation (77) gives the first three elements of the series expansion since these describe most important linear and nonlinear of optical phenomena.

$$\vec{P} = \varepsilon_o\left[\chi^{(1)}\vec{E} + \chi^{(2)}\vec{E}^2 + \chi^{(3)}\vec{E}^3 + \ldots\right] \tag{77}$$

The tensor quantities $\chi^{(1)}$, $\chi^{(2)}$, and $\chi^{(3)}$ are called the linear, and second- and third-order nonlinear optical susceptibilities. Reflection and refraction are explained by $\chi^{(1)}$. The quadratic nonlinear susceptibility allows second harmonic generation, sum and difference frequency mixing, optical parametric generation, and the linear electro-optic effect. The cubic nonlinear susceptibility is responsible for third harmonic generation, quadratic electro-optic effect, two photon absorption, stimulated Raman, Brillouni scattering and Rayleigh scattering.

For second-order nonlinear processes associated with $\chi^{(2)}$, the parametric mixing of three waves within a nonlinear material must be considered. Assume the incident field $\vec{E}(t)$ is composed of two angular frequencies $2\pi\nu_1$ and $2\pi\nu_2$ [rad/s] as given by

$$\vec{E}(t) = E_1 \exp(-i \cdot 2\pi\nu_1 \cdot t) + E_2 \exp(-i \cdot 2\pi\nu_2 \cdot t) + c.c. \tag{78}$$

then, the second order nonlinear polarization $\vec{P}^{(2)}(t)$ is given by

$$\begin{aligned}\vec{P}^{(2)}(t) = \varepsilon_o\,\chi^{(2)}\Big[&E_1^2 \exp(-2i \cdot 2\pi\nu_1 \cdot t) + E_2^2 \exp(-2i \cdot 2\pi\nu_2 \cdot t) + 2E_1E_2 \exp(-(2\pi\nu_1 + 2\pi\nu_2)t) + \\ &+ 2E_1E_2^* \exp(-i(2\pi\nu_1 - 2\pi\nu_2)t) + c.c. + 2E_1E_1^* + 2E_2E_2^*\Big]\end{aligned} \tag{79}$$

where the first and second terms of the right hand side account for second harmonic generation (SHG), the third term is for sum frequency mixing (SFM), and the fourth accounts for difference frequency mixing (DFM) process. The sum of the last two terms represents the process known as optical rectification. Frequency up-conversion processes such as SHG or SFM allow generation of visible or UV light from visible or near-IR diode laser sources, whereas DFM produces mid-IR (3 to 20 μm) by mixing radiation from the same type of sources.

All of these processes occur within the nonlinear material but they result in appreciable frequency conversion only under special conditions. The refractive index in the medium is different for optical fields at different frequencies, a process known as optical frequency dispersion. Since the two waves travel at different velocities in the medium, a phase difference is produced and accumulates along the path. The relative phase of the interacting waves determines the direction of generated power flow. For effective

power generation the interacting waves must stay in phase along the path. This requirement is known as phase-matching (PM).

3.3.1 Difference frequency mixing (DFM)

For difference frequency generation the interaction of three waves within the nonlinear material must be considered. The nonlinear parametric interaction of two electromagnetic fields, with frequencies $2\pi\nu_1$ and $2\pi\nu_2$, traveling through a nonlinear medium gives rise to a new electromagnetic field at $2\pi\nu_3 = 2\pi\nu_1 - 2\pi\nu_2$. Physically, the DFM process is described in Fig. 4. A photon at $2\pi\nu_2$ stimulates the break down of a photon at $2\pi\nu_1$ into two photons at $2\pi\nu_3$ and $2\pi\nu_2$, satisfying the conservation of energy $h\nu_3 = h\nu_1 - h\nu_2$. Since $2\pi\nu_2$ is amplified in the process, DFM is also known as "parametric amplification." By convention the fundamental beams are called "pump" (at $2\pi\nu_p$ [rad/s]) and "signal" (at $2\pi\nu_s$ [rad/s]), and the generated beam is known as "idler" (at $2\pi\nu_i$ [rad/s]) such that $2\pi\nu_p > 2\pi\nu_s > 2\pi\nu_i$; thus, $2\pi\nu_3 = 2\pi\nu_i$, $2\pi\nu_2 = 2\pi\nu_s$, and $2\pi\nu_1 = 2\pi\nu_p$.

To experimentally implement difference frequency mixing there are two main concerns: the selection of the mixing medium, which should posses a high nonlinear coefficient, and the PM conditions that optimize the power generation.

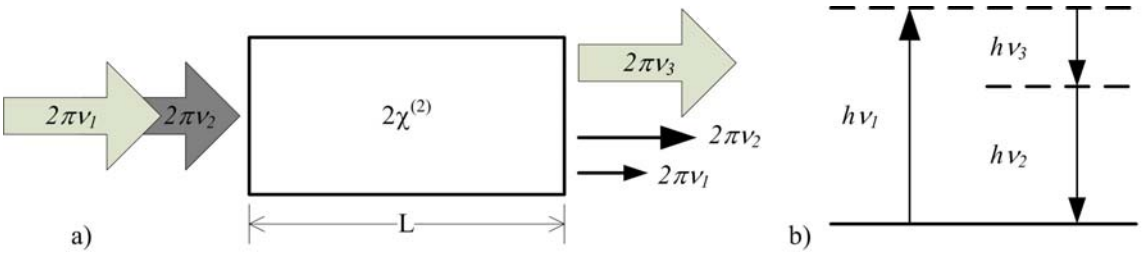

FIGURE 4 Difference frequency mixing. a) Schematic for the mixing, b) energy level interaction

The efficiency (η_{DFM}) of the DFM process was theoretically investigated by Boyd and Kleinman [127]. Considering the pump and signal beams (at $2\pi\nu_p$, $2\pi\nu_s$) to be collinear, Gaussian, and with equal confocal parameters ($b = 2Z_R$), the normalized theoretical conversion efficiency for perfect PM is given by

$$\eta_{DFM} = \frac{512 Z_R \pi^2}{c^3} \cdot \frac{(d_{eff})^2}{n_i n_s n_p} \cdot \frac{2\pi\nu_i^2}{\mathrm{w}_s^2 + \mathrm{w}_p^2} \cdot h(\mu, \xi, \alpha) \cdot \exp(-\alpha L/2) \tag{80}$$

Z_R is the Rayleigh range of the focused beams, c the speed of light in vacuum, n the index of retraction for pump, idler, and signal beams, w is the beam waist of the signal and pump beams, d_{eff} the effective nonlinear coefficient, and α is the absorption coefficient of the medium at frequency $2\pi\nu_i$. The so-called Boyd-Kleinman focusing function $h(\mu,\xi,\alpha)$ accounts for the beam focusing characteristics. The h-function is defined by Boyd and Kleinman [127] as a function of $\mu = (\mathrm{w}_s/\mathrm{w}_p)^2$ and $\xi = L/b = L/2Z_R$.

The conversion efficiency for a DFM process is proportional to the square of the nonlinear coefficient of the material (d_{eff}). For coupling of Gaussian beams, the h-function reaches a maximum at the focusing parameter $\xi \approx 1.3$ ($Z_R = 2.6L$).

The generated DFM power is proportional to the product of the input power of the fundamental beams and to the length of the crystal as given by (81). In practice the optical damage threshold limits the energy flux into the material.

$$\eta_{DFM} \equiv \frac{P_i}{P_s P_p L} \tag{81}$$

Previous results for conversion efficiency have assumed that PM condition was met. The phase matching condition is derived from the conservation of momentum (p) on the three wave interaction. Thus assuming the three waves are planar, traveling in the direction along the axis of the crystal (Fig. 4a) their momentum conservation can be expressed in terms of their wave propagation number (k) as given by

$$\begin{aligned} p_i &= p_p - p_s \\ \hbar k_i &= \hbar k_p - \hbar k_s \\ k_i &= k_p - k_s \end{aligned} \tag{82}$$

For perfect phase matching, the "phase mismatch parameter" (Δk) equals zero and is defined by

$$\Delta k = (k_p - k_s) - k_i = 0 \tag{83}$$

The intensity of the generated field (idler) is proportional to the "coherence factor" (F_c) as given by

$$F_c = L^2 \frac{\sin^2(\Delta k\, L/2)}{(\Delta k\, L/2)^2} \tag{84}$$

This function is periodic and the first maximum occurs at L_c

$$L_c = \frac{\pi}{\Delta k} \tag{85}$$

which is named the "coherence length". As a consequence, the maximum intensity is reached in a crystal L_c thick.

Phase matching methods compensate for the different phase velocities at different wavelengths (optical dispersion). Phase matching methods include phase change at reflection; in a Fabry-Perot type resonator phase change by reflection can be made to compensate slip due to dispersion.

Phase matching in birefringent materials is possible by choosing the propagation direction such that the phase velocity in the extraordinary direction matches the phase velocity of the ordinary direction. The phase velocity difference depends on temperature and the angle of the travel direction with respect to the crystal optical axis.

Quasi-phase matching (QPM) is an alternative technique for achieving phase matching in crystals. A QPM crystal is engineered such that the direction of one of its axes is reversed periodically. For properly chosen crystal orientation and polarization directions, this axis reversal results in a periodic modulation of the nonlinear coefficient tensor element responsible for the interaction. In contrast to birefringent techniques, that take advantage of naturally occurring crystal properties, QPM is accomplished by artificially engineering the structure of the crystal.

Due to the modulation of the nonlinear coefficient the interaction of the beams continues along the crystal and the generated intensity grows monotonically, albeit at a spatial rate smaller than in the case

of an ideal bulk phase matched crystal. The QPM period (Λ) is the distance at which the crystal structure is reversed. The phase mismatch for a QPM process (Δk_{QPM}) is expressed by

$$\Delta k_{QPM} = 2\pi\left(\frac{n_p}{\lambda_p} - \frac{n_s}{\lambda_s} - \frac{n_i}{\lambda_i} - \frac{1}{\Lambda}\right) \tag{86}$$

in terms of the index of refraction ($n_{i,p,s}$) and wavelength ($\lambda_{i,p,s}$) of the idler, pump and signal beams. When $\Lambda = 2L_c$ the condition for phase mismatch ($\Delta k_{QPM} = 0$) is achieved. Notice that the index of refraction is wavelength and temperature dependent; this dependency can be expressed by the Sellmeier equation. Jundt [128] evaluated the Sellmeier parameters for the case of lithium niobate.

Tuning of the QPM period is accomplished by varying the crystal temperature, taking advantage of temperature expansion properties of the bulk material. Alternatively, by tuning the angle of the crystal with respect to input beam the QPM condition can be tuned.

The QPM scheme can significantly extend the utility of a single material, because it can operate non-critically over the entire transparency range of the material. In addition, QPM can be achieved with fields parallel polarized to each other, so that they couple via the diagonal components of the nonlinear susceptibility tensor. These diagonal components are often quite large but inaccessible to birefringent phase matched interactions. The difficulty of implementing QPM lies in creating a medium with the sign reversals every coherent length, typically 1 to 100μm.

3.3.2 Nonlinear materials

When selecting the nonlinear material for mid-IR generation through DFM it is necessary to consider the transparency range of the material. For efficient DFM, absorption losses of the fundamental and generated beams should be negligible. Generated power is proportional to the nonlinear coefficient, therefore it is desirable that the material have a large nonlinear coefficient. Long crystals allow for increased conversion efficiency. Finally, the superficial damage threshold is important since it will limit the input power of the fundamental beams and thus the generated maximum power.

Given these requirements, many materials have been commonly used in DFM. Although none of them met all material requirements, their selection for DFM involves the evaluation and trade-off of the particular requirements. Fischer and Sigrist [125] present an excellent review of the properties of nonlinear materials used for DFM. They list nonlinear coefficients and transparency ranges for birefringent crystals (e.g., $AgGaS_2$, $ArGaSe_2$, GaSe, $ZnGeP_2$, $LiNbO_3$) and periodically poled structures made with ferroelectric materials [e.g., $LiNbO_3$ (PPLN), $KTiOPO_4$ (PPKTP), $RbTiOAsO_4$ (PPRTA), $LiTaO_3$, $KTiOAsO_4$ (PPKTA)] and semiconductor materials (e.g., GaAs, ZnSe). An extract of the Fischer and Sigrist list is reproduced in Table 7.

	Transparent range [μm]	Nonlinear coeff. [pm/V]
$AgGaS_2$	0.46 – 13	d_{36} = 17.5
$ArGaSe_2$	0.71 – 19	d_{36} = 33
GaSe	0.62 – 20	d_{22} = 54
$ZnGeP_2$	0.74 – 12	d_{36} = 69
$LiNbO_3$	0.35 – 5.5	d_{15} = -4.3
$LiNbO_3$ (PPLN)	0.35 – 5.5	d_{33} = -27
$KTiOPO_4$	0.34 – 3.2	d_{15} = 3.6
$KTiOPO_4$ (PPKTP)	0.34 – 3.2	d_{33} = 8.3
$RbTiOAsO_4$	0.35 – 5.8	d_{32} = 4.6
$RbTiOAsO_4$ (PPRTA)	0.35 – 5.8	d_{33} = 12.1
$LiTaO_3$	0.32 – 5.2	d_{33} = -21
$KTiOAsO_4$	0.35 – 5.3	d_{15} = 5.2
$KTiOAsO_4$ (PPKTA)	0.35 – 5.3	d_{33} = 12

TABLE 7 Selected properties of nonlinear materials commonly used for DFM. Extracted from Fischer and Sigrist [125]

Periodically poled lithium niobate (PPLN) is a recently developed QPM crystal that is significantly more efficient and tunable than conventional crystals. The technique of periodic poling lithium niobate (PPLN), which involves periodically inverting the crystal's structure on a micron scale, allows the properties of the material to be precisely tailored. In PPLN the use of the d_{33} nonlinear coefficient increases the nonlinearity of the process by a factor of 20 with respect to the birefringently

phase matched process [129]. With a near-IR input, PPLN can be used to generate radiation from 1.3 μm to the transparency limit of the material near 5.2 μm.

PPLN is poled by an electric field poling technique. In this process, a crystal of $LiNbO_3$ is photolithographically patterned with a metal electrode structure having the desired domain spacing. Regions between the metal electrodes are insulated using a thin layer of photo-resist, and a high voltage pulse is applied to the structure through a liquid electrolyte. Electric fields greater than 21 kV/mm are needed to pole the material and the desired domain shape is achieved by controlling the pulse width and current [130].

PPLN has a number of advantages. Principal among these are the large non-linearity of d_{33} poled material and the absence of the poynting vector walk-off. In addition the losses due to scatter and absorption are very low and have been shown to be comparable to those of congruent lithium niobate that is poled to a single domain. High-quality lithium niobate wafers are available from several vendors at competitive low costs.

The principal drawbacks of the material are associated with photorefractive effects and optical surface damage. Bulk damage includes photorefractive damage. Periodic poling cause photorefraction to be less severe than it is in the base material; however, in practice the effect can not be eliminated. PPLN crystals should be operated at high enough temperature to avoid photorefractive beam distortion.

CHAPTER IV

EXPERIMENTAL SYSTEM AND PROCEDURE

4.1 CO Sensor System

The schematic diagram of the CO sensor system is shown in Fig. 5. The sensor system is based on difference frequency mixing (DFM) of two near-infrared solid-state lasers in a PPLN crystal to produce tunable laser radiation in the 4.2 - 4.8 μm spectral region. The system consists of three major components: the laser sources, the DFM system, and the mid-infrared detection system. Figure 6 shows a photograph of the actual CO sensor.

4.1.1 Laser systems

To access the fundamental vibration-rotation band of CO in the 4.6 – 5.0 μm region, DFM of two near-IR solid-state diode lasers at 1064-nm and 860-nm was used. The 1064-nm laser system is a diode-pumped, Nd:YAG laser system and the 860-nm source is a tunable external cavity diode laser (ECDL).

The 1064-nm laser system is a high-power, compact diode-pumped infrared continuous-wave (cw) Nd:YAG laser system from CrystaLaser. The 1064-nm laser system has an output power of 550 mW. Its fixed vacuum wavelength was measured to be 1064.664 nm using a Burleigh WA-1000 cw

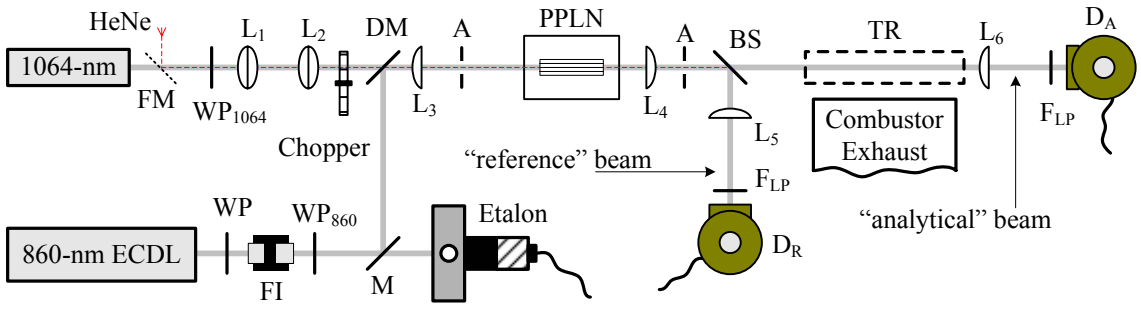

FIGURE 5 Schematic of the CO sensor layout. A – Aperture, BS – Beam splitter, D_A, D_R – Analytical and reference detectors, DM – Dichroic mirror, FI – Faraday isolator, F_{LP} – Long-wave pass filter, FM – Mirror in flipping mount, HeNe – Alignment laser, L – Lens, M – Mirror, PPLN – Nonlinear crystal in oven, TR – Test region, WP – Half-wave plate

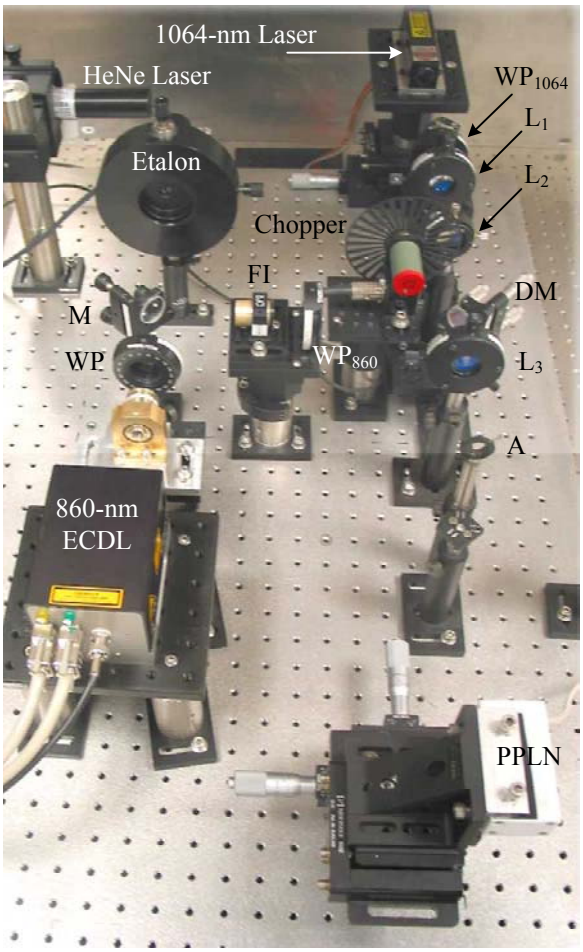

FIGURE 6 Photograph of the CO sensor layout. A – Aperture, DM – Dichroic mirror, FI – Faraday isolator, L- Lens, M – Mirror, PPLN – Nonlinear crystal in oven, WP – Half-wave plate

wavemeter. The major advantages of the diode-pumped Nd:YAG system are its excellent beam quality and stable power level. The beam of the 1064-nm laser is single mode TEM_{00} in a horizontal plane of polarization. According to specifications, the system output power is stable within 1% over 2 hours. In addition, it is compact (3 x 3 x 12 cm), easy to operate, does not require special cooling, and is reliable as required for sensor applications.

For the 860-nm source, a Toptica Photonics AG model DL-100 external cavity diode laser (ECDL) was used. This system was acquired with a GaAs-based diode laser. This semiconductor diode produces 136 mW of 854.2 nm radiation in the free-run mode (outside the external cavity). It was

delivered from Toptica adjusted to 852.831 nm with a maximum output power of 80 mW operating as an ECDL. With this particular diode, the system can be coarse tuned within the range 847.2 to 860 nm according to specifications. Its output power is reduced when the laser frequency is coarse tuned away from 853 nm. For typical operation of the ECDL at 860.782 nm, the output power was measured to be 58 mW.

In the DL-100 laser system the diode laser is part of an external cavity formed by the rear facet of the diode and a reflecting grating in the Littrow configuration. The spectral width of the output beam is reduced significantly by the external cavity. A 2 GHz free-spectral-range Fabry-Perot interferometer "SA^{Plus}" spectrum analyzer from Burleigh was used to observe the spectrum of the 860-nm system. Figure 7 shows the spectral analysis of the 860-nm ECDL output. The etalon peaks linewidth (FWHM) were measured to be 46 MHz which is limited by the cavity finesse and alignment. Although this spectrum does not provide the actual 860-nm beam linewidth, it must be much smaller than the 46 MHz measured.

In addition to the narrow linewidth, the frequency of the ECDL output can be tuned. The frequency of the ECDL system can be tuned coarsely by manually turning the cavity grating. The laser wavelength can be tuned approximately 7 nm above and below the free-running diode wavelength. Coarse

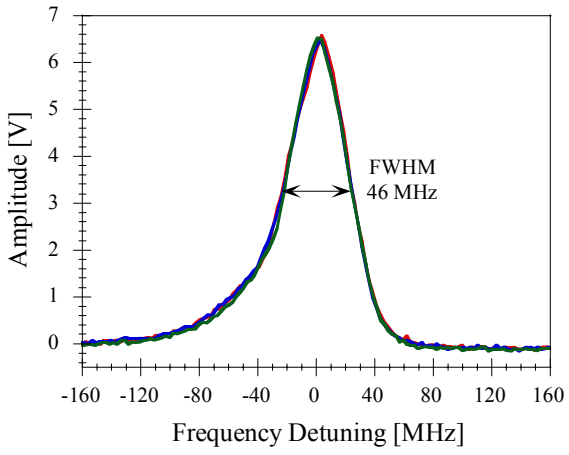

FIGURE 7 Etalon spectrum for the 860-nm ECDL system. The Spectrum was performed with a SA^{Plus} Spectrum Analyzer from Burleigh. The measured FWHM was of 46 MHz at the central wavelength of 860.782 nm

tuning was performed to tune the ECDL frequency into resonance with various CO transitions in the fundamental band. This coarse tuning of the grating was performed with a micrometer screw.

A piezoelectric crystal is mounted at the tip of the micrometer screw. The piezoelectric crystal is used for fine tuning of the laser. A triangular ramp was applied to the piezoelectric actuator via the "Scan Control Module" of the DL-100. The ECDL output was scanned, typically, at a rate of 1.3 Hz over a mode hop-free range of 12 GHz.

Scanning the laser output at higher rates is possible but in doing so, the single-mode operation of the laser is affected. As described in the Toptica manual for the ECDL [131], the single-mode operation of the ECDL is determined by the interaction of various factors:

1. The gain profile of the laser medium.
2. The mode structure of the laser diode internal resonator. The cavity is formed by the facets of the diode where the modes are determined by the distance between the facets and the index of refraction of the material in the active layer of the diode.
3. The mode structure of the external cavity. Determined mainly by the optical length of the cavity formed between the rear facet of the diode and the grating.
4. The angular dispersion and reflection profile of the grating.

When the piezoelectric actuator is modulated, factors 3 and 4 are modified. In order to suppress mode-hops the internal diode cavity length (factor 2) should be scanned as well. This can be done by modulating the diode operating current since a change in current leads to a change in the refraction index of the active medium. When the diode current is changed the internal and external cavities change at a different rate causing a mode competition in the ECDL which leads to multimode operation or to a decrease of the coherent length. These effects can be avoided by properly adjusting the diode laser current.

During scanning of the piezoelectric actuator, the control unit of the EDCL also modulates the diode current with a ramp proportional to the piezoelectric modulation. The scan control module of the DL-100 provides a "feed-forward" setting that allows controls the ratio between the scanning ramps of the piezoelectric actuator and the current. In addition, the diode operational current can be finely adjusted

with the "Current Control Module" of the DL-100. These modules provide an effective means to control the single mode operation. Once the current and feed-forward settings were adjusted minimal tweaking was necessary to correct for single mode operation of the 860-nm ECDL during the sensor operation.

External factors also affect the single mode operation of the laser. Back reflections into the 860-nm ECDL perturb the cavity. The single-mode operation of the ECDL was protected by using a 36-dB Faraday isolator that blocks back reflections into the ECDL (Fig. 5).

As noted above, scanning the ECDL output wavelength by modulating the piezoelectric actuator requires simultaneous modulation of the diode current to prevent mode-hops. This current modulation directly affects the output power of the ECDL laser system, which in turn is reflected in the mid-IR generation from the PPLN crystal. Figure 8 shows the resultant modulation in the generated mid-IR power due to the wavelength tuning of the ECDL. For the particular conditions portrayed in Fig. 7, the ECDL was modulated at a rate of 17.7 Hz over 5.9 GHz; at the central wavelength 860.782 nm, the ECDL output power was measured to be 50 mW. For this modulation of the ECDL the output power was varied by approximately 4% over the tuning range.

The DL-100 temperature is controlled using a thermoelectric Peltier element. Temperature

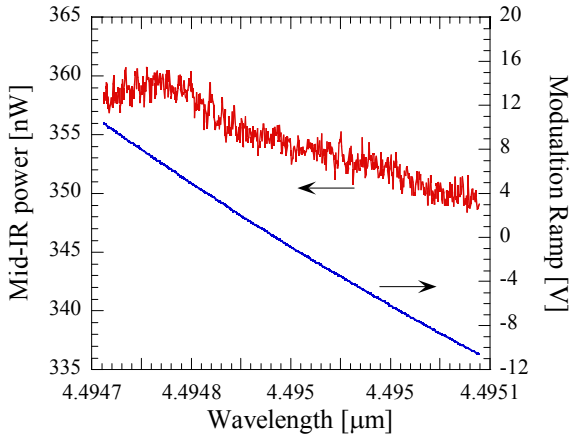

FIGURE 8 Mid-IR power generated by the DFM mixing process. The ECDL wavelength is tuned by applying a modulation ramp to the piezoelectric actuator. In this case ECDL was scanned at a rate of 17.7 Hz over a range of 5.9 GHz centered on transition R(23) at 2224.7127 cm^{-1}

control was required to operate single-mode with maximum power at a desired wavelength. For daily operation of the DL-100 it was necessary to check single-mode operation when the laser system was first turned on. Due to changing environmental conditions it was usually necessary to adjust temperature ±0.1 ºC or current by a few mA to reestablish single mode operation.

This readjustment of the ECDL operating variables reduces the reliability of the laser source and constant monitoring of the single mode operation of the ECDL is required. The SA^{Plus} spectrum analyzer shown in Fig. 5 is thus used to check the ECDL operation. The etalon also serves as a reference for conversion between the time and frequency domains, as will be discussed later in this chapter.

Two more disadvantages of the ECDL design are the quality of the beam shape and the walk-off of the beam. Since the output facet of the diode is square, the beam was re-shaped to circular by means of an anamorphic cylinder lens pair. This corrective optics also minimized the walk-off of the beam.

4.1.2 Difference frequency mixing system

Mid-IR radiation was generated through DFM of the 1064- and 860-nm beams in a periodically poled lithium niobate (PPLN) crystal. The PPLN crystal is commercially available from Deltronic Crystal Industries Inc. The crystal used is 40 mm-long, 0.5 mm-thick and 5 mm-wide. This crystal has a multi-period design. Along the width, the crystal is divided in four tracks each 1.25 mm wide. The correspondent QPM periods for the tracks are 22.8, 23.2, 23.6, and 24.0 μm. For the fundamental beams at 1064-nm and 860-nm, DFM was carried out using the 22.8 μm QPM period track. The QPM period was determined by (86). Bamford [126] provides a code that includes the temperature dependence of QPM period. The PPLN crystal was housed in a constant temperature oven that allowed adjustment of the longitudinal spatial period of the crystal structure. The temperature of the oven was controlled to maintain a constant temperature of the PPLN crystal to within 0.1ºC in the range 25 ºC to 220 ºC. For a particular combination of input frequencies, the temperature control was used to fine tune the phase matching requirement and optimize the DFM process.

Other factors were considered to optimize the DFM conversion in the PPLN crystal. Both fundamental beams were carefully overlapped on a dichroic mirror. As shown in Fig. 5 the 1064-nm beam was transmitted through the dichroic mirror whereas the 860-nm beam was reflected. The dichroic mirror has a dielectric coating so that the transmission and reflectivity are affected by the angle of incidence and beam polarization.

Half-wave plates were located in the beam paths before the dichroic mirror to allow adjustment of the polarization of each beam. In Fig. 5, these half-wave plates are designed WP_{860} and WP_{1064}. The 1064-nm beam polarization required to maximize transmission through the dichroic is different than the polarization required for the DFM process. The polarization of the fundamental beams was adjusted to optimize DFM in the PPLN crystal. The loss of power in 1064-nm beam by reflection at the back surface of the dichroic was measured to be approximately 120 mW. The power lost in the process of reflecting the 860-nm beam was much lower. For the 860-nm beam, the power drop across the Faraday isolator was approximately 5 mW. During scanning of the ECDL the power modulation is approximately 6 mW.

Once overlapped, the input beams were focused with a BK7 plano-convex f_3 = 300 mm focal length lens, designated L_3 in Fig. 5. The PPLN crystal was located so its center coincided with the waist location of the 860-nm beam. By using this lens, the focusing characteristics of the 860-nm beam were calculated and reported in Table 8. It is important to note that the calculations in Table 8 were performed assuming that the fundamental beams are Gaussian ideal beams which in the case of the 860-nm beam is not accurate. Thus, the numbers in Table 8 were used as a guideline. In these calculations, the Rayleigh ranges of the input beams focused by the L_3 lens are comparable to half the length of the PPLN. The waist diameters of the beams were just small enough to be contained within the crystal body.

To correct for the different focusing characteristics of the 860-nm and 1064-nm beams, a telescope was used in the 1064-nm beam path. The telescope allowed us to adjust the location and size of the 1064-nm beam waist. The telescope consisted of two bi-convex lenses of focal lengths of f_1 = 25.4 mm and f_2 = 50.2 mm. These lenses are labeled L_1 and L_2 in Fig. 5. In Table 8 the focusing characteristics of the 1064-nm beam after propagating through the telescope and lens L_3 are listed. The telescope distance reported in Table 8 corresponds to the distance between lenses L_1 and L_2, for a typical distance L_2

to L_3 of 100 mm. The alignment procedure, as described in the following section, ensures proper spatial overlap of the fundamental beams within the crystal by using a 150-μm-diameter pinhole.

Transition	Wavelength [nm]*	Rayleigh range [mm]	Beam waist radius [μm]	Focus location from L_3 [mm]	Telescope distance [mm]
R(25)	860.351	17.5	69	303.18	
	1064.664	17.75	77		71.12
P(19)	872.826	17.8	70	303.15	
	1064.664	19.35	80		71.10

This calculations assume a Gaussian beam profile. Condition not satisfied by the ECDL and the calculations are approximate.

* The refraction indexes in BK7 used are $n_{860nm} = 1.50966$, and $n_{1064nm} = 1.50663$ [132].

TABLE 8 Focusing properties# of the 860-nm and 1064-nm fundamental beams at the PPLN center. The selected transitions are the limits of the CO lines in Table 6

4.1.3 Detection systems

The mid-IR radiation generated in the PPLN crystal was collimated using a plano-convex calcium fluoride (CaF_2) lens after exiting the PPLN crystal. The collimation lens, L_4 in Fig. 5, has a focal length f_4 = 150 mm. After collimation the mid-IR beam was split into two beams designated the "analytical" beam and the "reference" beam. A CaF_2 50-50 dielectrically coated beamsplitter from Janos Technologies was used to split the mid-IR beam. Other authors [133, 134] have used the dual-beam detection scheme that allows for the subtraction of common noise and etalon effects. In situations where the generated power was low, the splitting of the beam reduced the power reaching the detector and thus decreased the signal-to-noise ratio (SNR). For those situations, the beamsplitter was removed and only the "analytical" beam was used.

The "analytical" beam was directed through the "test region" were optical absorption by carbon monoxide molecules occur. In Chapter V the application of the sensor to three "test regions" is discussed: (1) a room-temperature gas-cell filled with a mixture of CO and buffer gases, (2) the exhaust of a well-stirred reactor and gas turbine, and (3) the post-flame region of a hydrogen/air flame doped with CO_2. The optical path length was assumed to be equal to the length of the test region It was also assumed that CO

was homogeneously distributed through the test region and that the temperature in the test region was uniform.

Both "analytical" and "reference" beams were directed through optical filters and then focused onto cryogenically cooled InSb detectors. The beams were focused using plano-convex CaF_2 lenses. These lenses are shown in Fig. 5 as L_5 for the "reference" beam and L_6 for the "analytical" beam. For these lenses, the focal lengths were f_5 = 200 mm and f_6 = 150 mm. To reject the 860-nm and 1064-nm radiation longwave-pass filters from Spectrogon were used, shown as F_{LP} in Fig. 5. These filters have a transmission region from 3.5 μm to 6.6 μm. According to the manufacturer filter tests, the average transmittance of these filters for the 4.4 to 4.8 μm region was 85% and 86% while the fundamental beams are completely blocked by the filters.

The intensities of the "analytical" and "reference" beams were measured using two indium antimonide (InSb) detectors from Kolmar Technologies Inc., and shown as D_A and D_R in Fig. 5. The detectors have an InSb photodiode with 1 mm^2 active area and operate in the spectral region from 1 μm to 5.4 μm. For cryogenic operation, a 17 cm tall dewar holds liquid nitrogen for 12 hours. These detectors were selected to have matching spectral responses to within 5%. Their relative sensitivity parameter (D^*) is 2.04×10^{11} $cmHz^{1/2}W^{-1}$ measured at 5.23 μm and at 10 kHz and the detector responsitivy is 0.39±0.003 MV/W. The detectors were acquired with the integrated preamplifier option with a bandwidth of 5 MHz. These detectors were reviewed as the best in terms of noise as indicated by a highest D^* [135].

4.2 Alignment Procedure

The alignment of the input beams is obviously critical to the nonlinear interaction in the PPLN crystal. To ensure that the fundamental beams are parallel, collinear, and focus with the same characteristics at the center of the PPLN crystal an alignment procedure was developed.

The first step in the alignment procedure is to determine the optical height of the system. The optical height is the distance from the table to the plane of propagation of the lasers. To increase the mechanical stiffness of the system it is desirable to minimize the optical height. For the CO sensor, the

optical height was determined by the PPLN crystal oven. The optical height of the sensor was set at 17 cm, the minimum possible due to the size of the oven and the mounting requirements for the oven. The centers of two apertures were set at this height and the apertures were located as shown in Fig. 5. The line between the centers of the apertures set the desired propagation direction of the laser beams. These apertures allowed for coarse alignment of the sensor and were untouched during the alignment process.

To assist in the alignment of two near-IR laser beams, a visible HeNe laser was used. This HeNe laser beam was not used during sensor operation, and therefore a flipping mirror mount was used to include it, when necessary, in the optical path. As shown in Fig. 5, the HeNe laser was directed through the two main system apertures. After the addition of any optical component to the HeNe path re-alignment of the HeNe was performed to ensure that the beam still traveled through the apertures. Also, the HeNe beam makes alignment of the lenses easier.

The ECDL was mounted at the optical height and the two 45º reflections that were performed before getting to the first aperture provided enough degrees of freedom to precisely align the lasers through the apertures. The ECDL was fixed on an aluminum plate. At the first reflection shown in Fig. 5, the 860-nm beam lost about 1 mW which was transmitted through the first mirror and was collected by the SA^{Plus} spectrum analyzer. The spectrum analyzer was used to constantly monitor the wavelength and single-mode operation of the ECDL. The second reflection of the 860-nm beam occurred at the dichroic mirror and care was taken to assure that the reflection was at 45º. The beam shape of the 860-nm beam was oval and a consistent criterion has to be used to decide if the beam is centered in the aperture. At this point the alignment was still coarse and so it was not very important to ensure perfect alignment through the apertures.

The Crystalaser 1064-nm laser source has the advantage of being small and light, thus it was possible to mount it on a kinematic mount with five degrees of freedom. This mount allows translation in three directions and rotation in two directions, simplifying the alignment of the 1064-nm through the main system apertures. Therefore 1064-nm beam is sent directly into the dichroic mirror. For applications other than laboratory testing, the Crystalaser was fixed to an aluminum plate and two reflections were used to direct the beam through the back of the dichroic into the two apertures.

Once both beams were aligned through the apertures the rest of the optics were installed. The 860-nm beam path was aligned first. When the Faraday isolator was inserted into the beam path the beam deviated from the original path through the apertures; this deviation was corrected using the mirror and dichroic mirror combination. After the half-wave plates and the Faraday isolator were in place, focusing lens L_3 was added. Alignment of lenses is performed by monitoring into the back reflections. For precise lens alignment, back reflections from the lens follow the incoming beam path. Additionally, the focused ECDL beam must pass through the main system apertures.

The telescope lenses were the next elements to be installed. In aligning these lenses it was found to be better to start by aligning lens L_2 and then aligning L_1. In this coarse stage of the alignment procedure the telescope lenses were located at the distances calculated using Gaussian beam propagation equations as shown in Table 8. Lens L_1 was mounted on a translational stage so that the telescope separation could be finely adjusted later. When looking at back reflections from one lens, the beam was blocked after it so the back reflections from the following lenses did not interfere with the alignment. Again, alignment of the lens back reflection and the beam through the apertures was an iterative process. Once the lenses were aligned, the 1064 half-wave plate was installed.

At this point the three beams were roughly collinear through the apertures and focused close to the same axial location. A 150 μm-diameter pinhole on a lens x-y mount was used to perform more precise alignment of the beams. In the process of using the pinhole, it was noticed that the beam waist was always larger than the pinhole diameter therefore the beam was blocked and a power drop was observed. The transmitted power was measured with the visible version of the LaserMate-Q® silicon power meter from Coherent®. This model features a fast response with scale resolution of 0.1 nW for cw power measurements in the range 100 nW to 100 mW. For the 1064-nm beam power measurements, a 10% transmission neutral density filter was used to attenuate the radiation incident at the detector.

The transmitted power through the pinhole was measured as an indication of the localization of the beam, i.e. for a given longitudinal location, in the direction along the beam path, the maximum power transmission through the pinhole indicates the position of the center of the beam. Due to the required Rayleigh range of the beams, the specific location of the waist was not always easy to identify. By using

transmitted power measurements the beam waist was found by comparing different axial locations. With the pinhole located at the radial center of the beam, the axial location with the highest transmitted power was closer to the beam waist. Measurements of transmitted power at a series of axial locations were used to determine the position of the beam waist. For this task, the pinhole was mounted on a 1-inch translational stage that allowed easy displacement of the pinhole along the longitudinal direction.

The focusing characteristics of the 860-nm were mainly determined by the beam diameter and divergence at the first surface of the focusing lens L_3. In turn, the spot size of the 860-nm beam was found to depend on the ECDL grating angle and the corrective anamorphic cylindrical lens pair. Therefore, the waist size and location of the 860-nm beam were fixed for a specific ECDL wavelength setting. The first step for fine alignment was to find the location of the 860-nm waist using the pinhole. Typically, the power drop at the pinhole was on the order of 50% to 60% of the incident power of either the 860-nm or the 1064-nm input beams.

The location of the 1064-nm beam waist was then found, and the telescope distance was adjusted so that the 1064-nm beam waist and the 860-nm waist were at the same axial location. It was found that increasing the telescope distance caused the 1064-nm beam waist to move towards the focusing lens L_3. The axial focal position of both beams was noted since the center of the PPLN crystal was placed at the same location.

The collinearity of the input beams was then checked. The farther the pinhole can be located from the waist location the more precise is the collinearity check for the beams. A translation stage was used to position the pinhole 0.5 inches before and after the waist location. At these axial locations, the center of each beam was found with by power transmission through the pinhole. Normally after the coarse alignment, the 1064-nm and 860-nm beams traveled parallel to each other but were not collinear. Typically, the 860-nm beam was then adjusted so that its path coincided with the 1064-nm beam. The HeNe beam was also checked for collinearity through the pinhole, although its focal position was of no interest.

Before placing the PPLN oven in the beam path, the collimation lens L_4 and the analytical detector components (L_6, F_{LP} and D_A) were aligned using the HeNe beam. The collimation lens was

initially located at its nominal focal length 150 mm from the waist location. Final optimization of the collimation through lens L_4 of the mid-IR beam was performed later. The analytical detector components were located close to the collimation lens, On a temporary basis to assist during alignment of the PPLN crystal.

The oven that houses the PPLN crystal is mounted on a kinematic mount with five degrees of freedom to allow precise orientation of the PPLN crystal. For coarse alignment of the PPLN crystal and selection of the desired crystal track two translation stages were used parallel to and perpendicular to the beam path. The oven temperature was initially set at the calculated optimum temperature for a particular combination of input wavelengths. As mentioned earlier, the 22.8 μm QPM period was used and the temperature was calculated by means of (86) as programmed by Bamford [126]. Empirically, it was observed that mid-IR radiation was detected over a PPLN crystal temperature range of ±4 ºC around the working temperature. Therefore, the calculated optimum crystal temperature is a good starting point for the oven temperature.

Initially the PPLN crystal was oriented horizontally and along the beam propagation path. The initial alignment was done by observing the HeNe beam at the exit of the crystal. The initial polarization of the fundamental beams was checked and was adjusted using the half-wave plates so that both beams were vertically polarized. At this point, the ECDL was not scanned and only single mode operation at its central wavelength was required. The optical chopper was placed in the 1064-nm beam path and adjusted to a frequency of about 500 Hz.

The lasers, chopper and detector were turned on. A digital oscilloscope was triggered by the synchronous output from the chopper. Since the 1064-nm beam was chopped, the nonlinear interaction in the PPLN crystal occurred only when the chopper unblocks the beam. The observed response of the detector was a square-wave at the chopper frequency. The amplitude of the square-wave is a measurement of the power of the generated mid-IR radiation. The DFM process was optimized by maximizing the amplitude of this square-wave.

The nonlinear conversion was very weak with vertically polarized input beams and fine adjustments therefore induce large changes in the amplitude of the mid-IR power square-wave. Fine alignment of the PPLN crystal was performed using vertically polarized beams. Te detector positioning was optimized, also the orientation of the PPLN was adjusted, and the overlap of the 860-nm input beam was adjusted to maximize mid-IR generation. The polarization of the input beams was then adjusted with the half-wave plates to maximize the amplitude of the mid-IR power square-wave.

Although the theoretical optimum DFM temperature calculated from theory is a good initial setting for the oven temperature, fine tuning of the oven temperature was required to ensure maximum DFM conversion. Usually the oven was raised 7 ºC above the initial set temperature the mid-IR power was monitored. Maximum nonlinear conversion was usually observed within this temperature interval. Once stabilized at the higher temperature the oven temperature was decreased at 0.3 ºC intervals. The temperature for maximum mid-IR generation was determined.

Once the DFM system has been aligned and adjusted, the analytical detector system was re-positioned after the test region. This alignment was performed using the HeNe beam since it follows closely the generated mid-IR. First the InSb detector was located at the center of the red spot. Then the collimation lens L_4 was adjusted with the assistance of the analytical detector. The beam splitter was then placed after the collimating lens. The beam splitter requires 45º incidence for a 50-50 split. The D_A and D_R detectors, long-wave filters and focusing lenses L_5 and L_6 were then aligned. The detectors D_A and D_R were translated to ensure that the focused beams incident on the detectors were smaller than the InSb pothodiode.

For daily operation minor tweaking of the alignment of the PPLN orientation was usually required and on occasion some tweaking of the mirror in the 860-nm beam path was required.

4.3 Experimental Procedure

The discussion of the experimental procedure is divided into two parts: the operation of the sensor and the processing of the CO absorption data.

4.3.1 Data acquisition

The specific CO transition for the absorption measurements was selected before starting the alignment procedure. The ECDL was then coarse tuned so that the generated mid-IR radiation is close to resonance with the desired transition. Within the tuning range of the ECDL, mid-IR radiation can be produced in the 4.4 – 4.85 μm spectral region through the DFM process. Vibrational-rotational CO transitions in the fundamental band in the ground state that were interrogated in this project included R(25), R(24), R(23), R(20), R(11), P(18), P(19), and P(13) as listed in Table 6.

Once the ECDL wavelength was set and the alignment carried out, the sensor was ready to operate. First the single mode operation of the ECDL during scanning of the piezoelectric actuator on the grating was checked. The current and the feed-forward were adjusted to obtain typically 12 to 14 GHz of mode-hop-free tuning range of the ECDL. During operation of the sensor, the etalon was used to monitor the wavelength tuning of the ECDL. This etalon was also used to ensure that the ECDL continue to operate single-mode.

The mid-IR generation process was started with the modulated 860-nm beam and the 1064-nm beam going into the PPLN crystal. The optical chopper in the 1064-nm beam path was then started and set to a frequency of 3 kHz. With this chopping action the amplitude of the generated mid-IR was modulated in a square-wave fashion. The InSb detectors signals were processed the by lock-in amplifiers referenced to the optical chopper synchronous output. The use of lock-in amplifiers allowed us to detect the mid-IR signal, removing the amplitude modulation along with noise outside the lock-in bandwidth centered at the chopper frequency. The principles of operation of the lock-in amplifier are discussed in Appendix B.

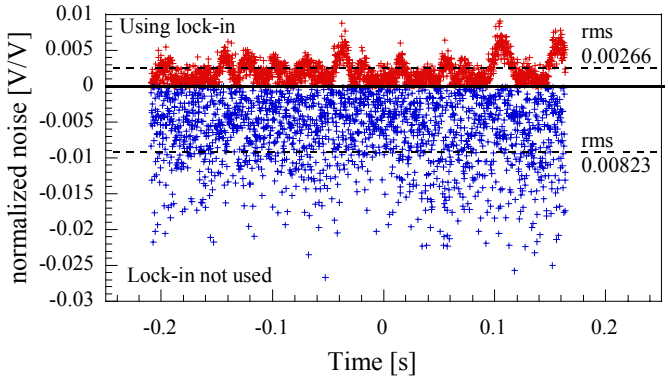

FIGURE 9 Normalized noise comparison of mid-IR scans acquired with and without the lock-in amplifiers. For clarity purposes, data taken without using the lock-in amplifier is presented as the negative of its absolute value. The ECDL was scanned at a rate of 1.34 Hz over a mode-hop-free tuning range of 14 GHz. Mid-IR power at the analytical detector was measured to be 250 nW at the central wavelength. The lock-in amplifier was referenced at 2.4 kHz, with a time constant of 3 ms at 24 dB/oct. Use of phase sensitive detection reduced normalized noise by three times

The noise reduction achieved by using the phase sensitive detection of the lock-in amplifier is shown in Fig. 9. For the results shown in Fig. 9, the ECDL was coarse tuned to 863.613 nm. The generated mid-IR was in resonance with transition R(11) of the CO molecule in the fundamental band at 2186.639 nm; however, for the noise measurements there was no CO in the beam path. The ECDL was scanned at a rate of 1.34 Hz over a mode-hop-free tuning range of 14 GHz. The mid-IR power was 250 nW. The noise data was first recorded without using the lock-in amplifier; data was measured directly from the pre-amplifier of the InSb detector. The noise data were normalized by fitting the data to a quadratic polynomial. Residuals were measured as the difference between data and the fit. Normalized noise was then obtained by dividing the residuals by the fit value. For clarity purposes, in Fig. 9 normalized noise data for the case when no lock-in was used is presented as the negative of its absolute value. The rms standard deviation value of the noise when the lock-in amplifiers was not used was computed at 0.00823 V/V. The chopper was then started and set to a frequency of 2.48 kHz. The trigger of the chopper was used as the reference for the lock-in amplifier. The lock-in amplifier time constant was set at 3 ms with a roll off slope of 24 dB/oct. Under these conditions the low pass filter after the phase

sensitive detection had a bandwidth of 26 Hz. Normalization of the noise was performed in the same manner as for the previous case. For display purposes, the positive absolute value was taken as shown in Fig. 9. Using phase sensitive detection the rms standard deviation of the noise was calculated to be 0.00266 V/V, three times lower than the value when the signal was read read directly from the detector.

Data was collected through a four-channel, digital oscilloscope Tektronix TDS 3014. The oscilloscope was connected via a GPIB interface to a personal computer. A LabView code was written to control the oscilloscope and to record data from the four channels automatically.

The digital oscilloscope was triggered by the modulation ramp of the piezoelectric actuator in the ECDL. Single mode operation of the ECDL was tracked by recording the etalon photodiode signal. The signal from the etalon was also collected because it is used to convert the oscilloscope time scale to the ECDL frequency domain. The analytical and reference signals were processed by corresponding lock-in amplifiers, and the output of the lock-in amplifiers was also recorded by the Tektronix digital oscilloscope.

For each scan, the oscilloscope recorded all four channels. Figure 10 illustrates the oscilloscope screen. In a single scan the ECDL modulation ramp, the etalon trace, analytical, and reference detector

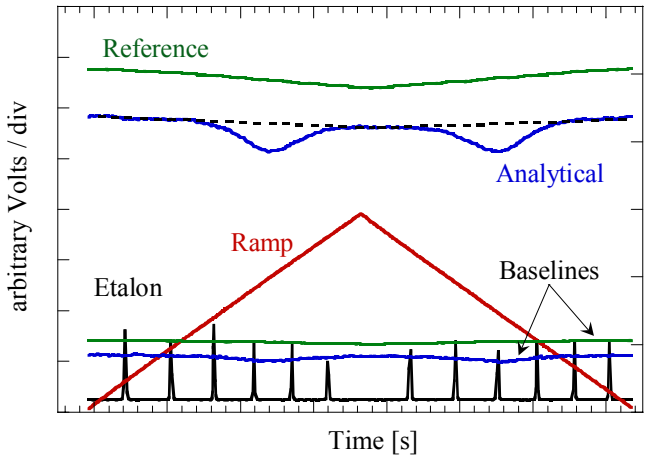

FIGURE 10 Illustration of the data acquisition through the digital oscilloscope. Four channels are simultaneously acquired: ramp of the ECDL scanning, etalon trace, analytical, and reference detectors signals. The indicated baselines are the analytical and reference detector signals taken when mid-IR generation was cancelled

signals were acquired. Notice that in the oscilloscope screen there is an axis of symmetry around the tip of the scanning ramp and thus only half of the ramp period is of concern, this is called "single scan." In one period of the scanning ramp, the wavelength of the mid-IR beam sweeps through the absorption feature twice. These two scans of the same absorption transition are presented together and are designated "Absorption 1" and "Absorption 2".

Figure 10 also includes the baselines for the analytical and reference detectors. Baselines were required to determine the zero levels for the detectors; the baselines are the detector response when the mid-IR generation has been cancelled. To cancel the mid-IR generation the 1064-nm half-wave plate was detuned 45º from its operating position. Thus, the optimum polarization of the 1064-nm beam was rotated 90º, canceling the generation of mid-IR. At the same time, the input beams are still intense.

To reduce random noise several consecutive traces were averaged. The effect of time averaging on the noise reduction can be observed in Fig. 11. Data in Fig. 11 was taken directly from the analytical detector without using the lock-in amplifier. The power of the mid-IR radiation incident on the detector was measured to be 500 nW. The ECDL was scanned at a rate of 265 mHz, therefore the data acquisition

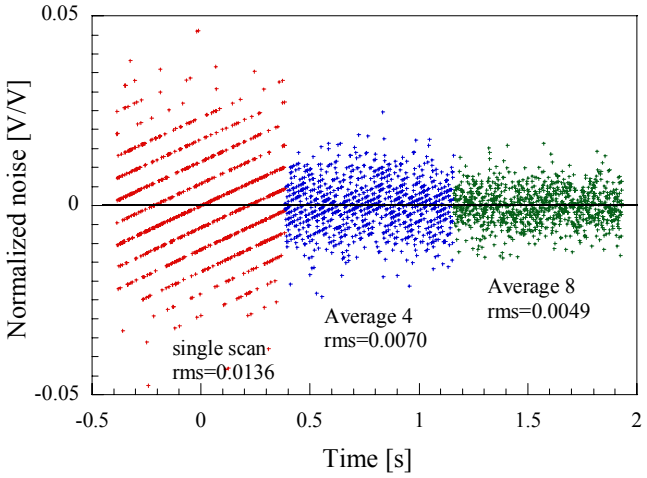

FIGURE 11 Random noise reduction by time averaging. The figure compares the normalized noise in a single scan to the noise obtained when four and eight scans are averaged. No phase sensitive detection was used in this measurements and analytical detector measured 500 nW of mid-IR radiation

time for a single scan was 1.88 s. The normalized rms standard deviation of the noise for a single scan was calculated to be 0.0136. When four single scans were averaged, the normalized noise was reduced 1.94 times. For the averaging of eight scans the noise was reduced by a factor of 2.77. Total acquisition time (t_{acq}) is computed from the ECDL scanning rate (f_{RAMP}) and the number of averaged scans (n_{SCANS}) using

$$t_{acq} = \frac{n_{SCANS}}{2 f_{RAMP}} \tag{87}$$

Averaging can be performed in two ways: by averaging in software or by averaging in hardware. The former implies acquiring single scans and averaging their corresponding data points. This method offers flexibility in determining how many scans are averaged. Average in hardware is performed directly on the oscilloscope and is limited by the instrument. In selecting either method of averaging digitization of the acquired data must be considered. A close look at the normalized noise for the single scan in Fig. 11 shows that the data as acquired by the oscilloscope has been rounded to discrete values. This type of "read noise" is reduced by the averaging of several single scans as observed in Fig 11. If averaging is done on the oscilloscope the read noise will be present just as in the single scan.

To reduce the read noise averaging of neighboring oscilloscope channels was performed. This binning of the oscilloscope channels reduces the read noise but it could affect the shape of the transition if the transition is very narrow. The possible effects of binning on the shape of the CO P(19) were investigated. Figure 12 depicts the CO absorption transition P(19) in the fundamental band at 2064.3969 cm^{-1}. This absorption feature was resolved in 1524 channels, a typical value for a CO transition in the fundamental band where lines are about 4 GHz wide. Bin 1 in Fig. 12 was generated by averaging in software 9 consecutive scans. Each scan was acquired in 1.95 s and the analytical detector signal was processed using the lock-in amplifier. Much of the noise in curve Bin 1 is due to read noise. By binning 10 neighboring channels the curve is smoothed and noise is reduced but its line shape is not affected, resulting in a better fit. When 100 channels are binned, the line shape is lost and only a few points remain. In this extreme case the fit to the curve will not give reliable results. For the experiments performed in this project, data was typically averaged over 10 neighboring channels.

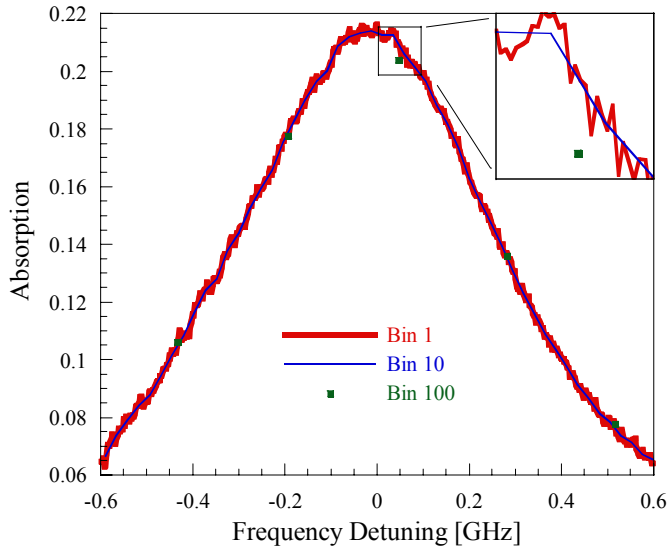

FIGURE 12 The effect of binning oscilloscope channels in the absorption shape. The absorption line shown is the CO transition P(19) of the fundamental band at 2064.3969 cm^{-1} acquired in a room temperature gas-cell at 26.66 kPa. Bin 1 corresponds to the resultant of software averaging of 9 scans acquired using phase sensitive detection. The shown portion of the transition corresponds to 504 channels and the full transition was contained in 1524 channels. Bin 10 and Bin 100 result from averaging 10 and 100 consecutive channels respectively

4.3.2 Data processing

Once the data was acquired it was processed to determine the concentration of CO in the test region. The accurate determination of the spectral absorptivity A_ω is the primary objective of data processing. According to Beer's law the absorptivity can be computed from the measured absorption spectrum, as shown on the left hand side of (42), or by application of quantitative absorption spectroscopy principles, as shown on right-hand side of (42). Matching of these two results to obtain the absorbing gas concentration was done through the full-parameter fit procedure described in Chapter III.

$$A_\omega \equiv \frac{I_\omega(0) - I_\omega(L)}{I_\omega(0)} = 1 - \exp(-k_\omega L) \tag{42}$$

The code "Direct_Absorption" was developed to perform the full-parameter fit procedure described in Chapter III. The code allows for software averaging of several single scans, and binning of oscilloscope channels as described previously. The conversion of the oscilloscope time base to the frequency domain using the etalon trace is also performed. The normalized absorptivity is determined automatically.

In spectroscopy, data is presented as a function of the radiation frequency or wavelentgh. In this experiment the wavelength of the mid-IR radiation is directly related to the wavelength of the EDCL. The recorded etalon trace keeps track of the ECDL laser frequency as a function of the modulation ramp which is a time modulation of the piezoelectric actuator. Knowing the parameters of the Fabry-Perot interferometer, the time to frequency conversion can be performed. The output intensity ($I_{transmitted}$) of an ideal etalon is given by the Airy function [136]

$$\frac{I_{transmitted}}{I_{incident}} = \left[1 + F\sin^2\left(\frac{\pi\nu}{FSR}\right)\right]^{-1} \tag{88}$$

where $I_{incident}$ is the intensity of the incident laser light, F is the finesse of the etalon and is related to the reflectivity of the mirrors, and FSR is the free-spectral-range of the cavity and is set by the distance between mirrors. In a confocal cavity design, the FRS is given by the curvature of the mirrors. The SA^{Plus} spectrum analyzer used is a confocal cavity with two spherical mirrors with a FSR of 2 GHz. The incident laser frequency (ν) is a function of time since the ECDL is scanned by changing the grating angle with time. Assuming a quadratic relationship for the time dependence of $\nu(t)$, the etalon trace can be expressed by

$$I_{transmitted} = \frac{I_{incident}}{1 + F\sin^2\left(\frac{\pi}{FSR'}\left[\mathrm{A}'(t-\mathrm{C}')^2 + \mathrm{B}'(t-\mathrm{C}')\right]\right)} + offset \tag{89}$$

By adjusting the parameters A', B', C', F, $offset$, $I_{incident}$, and 1/FSR', a theoretical curve was fit to the recorded data trace of $I_{trasmitted}$. The evolutionary and Levenberg-Marquardt routines in the "Direct_Absorption" code were used to fit the seven parameters of (89) to the recorded trace. Figure 13 shows an example of the etalon fit. The conversion between time and frequency domains was determined using

$$\nu = \frac{FSR}{FSR'}\left[\mathrm{A}'(t-\mathrm{C}')^2 + \mathrm{B}'(t-\mathrm{C}')\right] \tag{90}$$

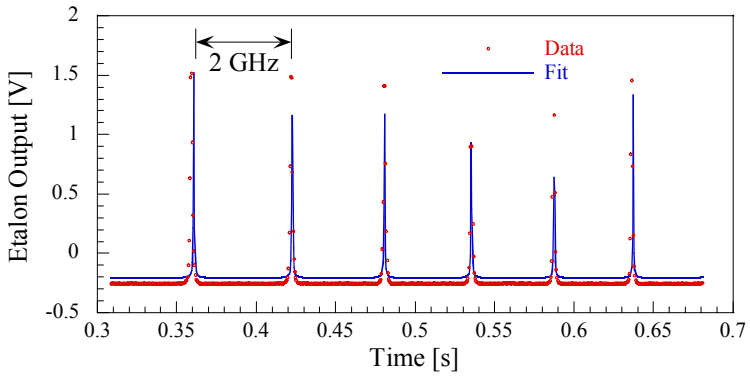

FIGURE 13 Fitting (89) to a recorded etalon trace

With the data referenced to laser frequency, normalization of the absorption trace was performed. Normalization of the absorption data was carried as indicated in the left-hand side of (42). The analytical detector will measure the power corresponding to the spectral intensity ($I_\omega(L)$) after the path length (L). The intensity before the test region ($I_\omega(0)$) was either measured or calculated. The code "Direct_Absorption" offers four normalization schemes for the selection of $I_\omega(0)$: A) use of the reference detector signal scaled by no-CO traces, B) use of the reference detector scaled by maximum data points, C) direct measurement of $I_\omega(0)$ with the analytical detector under conditions of no-CO in the test region, and D) fit of a polynomial to the un attenuated regions of the analytical signal. The option name A, B, C, and D is the menu order in the "Direct_Absorption" code. Selection of the normalization scheme is dependent on the type of data acquired which depends mainly on the conditions of the test.

Scheme C is the easiest to explain. To implement this scheme the reference detector was not used. Thus, all of the generated mid-IR was used in the analytical detector improving the signal-to-noise ratio (SNR) by a factor of two. To directly measure $I_\omega(0)$ with the analytical detector a condition of no-CO present in the test region must be achieved. In the case of gas-cell measurements, the gas cell was emptied and filled with air or nitrogen and a no-CO scan was performed. Next the cell was emptied and

filled with an absorbing mixture containing CO. A CO scan was then performed. The baseline trace was also recorded and the normalized absorption was computed as the ratio of the traces by

$$\text{Absorption}_C = 1 - \frac{(\text{analytical} - \text{baseline})_{\text{CO scan}}}{(\text{analytical} - \text{baseline})_{\text{no-CO scan}}} \tag{91}$$

Panels in Fig. 14 show both traces at CO and no-CO conditions and the resulting normalized absorption along with it theoretical best-fit. The data shown corresponds to transition R(11) in the CO fundamental band at 2186.639 cm^{-1}. The laser system must be very stable with minimal temporal changes or drifts such that the no-CO condition can be implemented and scheme C can be applied.

Scheme D is commonly used for CO scans. It can be applied when the scanning range of the system is large enough to resolve the wings of the transition line and it is not possible or feasible to have a no-CO condition in the test region, i.e. exhaust of an engine. In scheme D the un-attenuated portions of the analytical scan were fit using a 3rd degree polynomial approaching the trace of $I_o(0)$. By computing the polynomial the un attenuated regions must be distinguishable which is easy if the transition has a Gaussian shape (Doppler broadening).

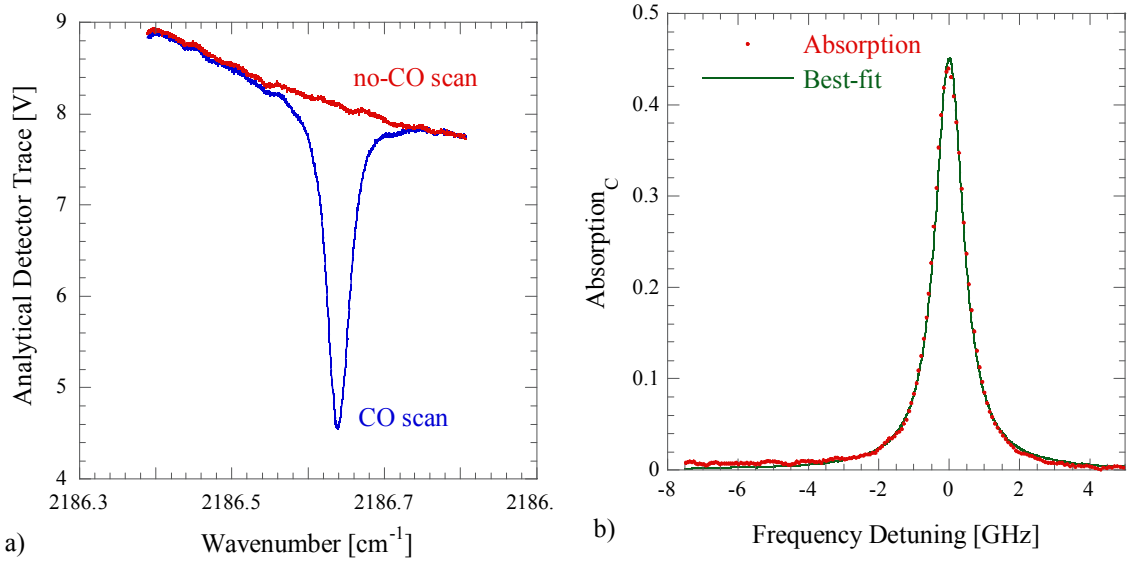

FIGURE 14 Normalization scheme C. Panel a) Analytical detector traces acquired for the absorbing and no-CO conditions of the test region. b) the resulting normalized absorption with its best-fit theoretical shape

Figure 15 shows the same data as Fig. 14 but scheme D was used to compute the normalized absorption using

$$\text{Absorption}_{\text{D}} = 1 - \frac{(\text{analytical} - \text{baseline})_{\text{CO scan}}}{\text{polynomial fit}} \tag{92}$$

observe that when the polynomial is used, the noise in the analytical trace also appears in the absorption feature. In the case of scheme C the noise that is common to the no-CO condition, i.e. an etalon effect, was reduced by the normalization as indicated by Hanna *et al.* [133].

Scheme B is an alternative approach for the case in which the no-CO condition of the test region is not feasible to obtain but the mid-IR power is sufficient to be divided in the beam splitter. In scheme B the spectral intensity before the test region ($I_\omega(0)$) is measured using the reference detector. The reference detector trace contains the noise common to the analytical trace and using it to normalize the absorption will reduce this noise. It is clear in Fig. 10 that for scheme B to be applicable the traces from each detector must have the same slope. The slope of the traces is a function of the spectral response of filter and detector to the modulation of the mid-IR radiation and to certain extent it can be adjusted, i.e., by rotating

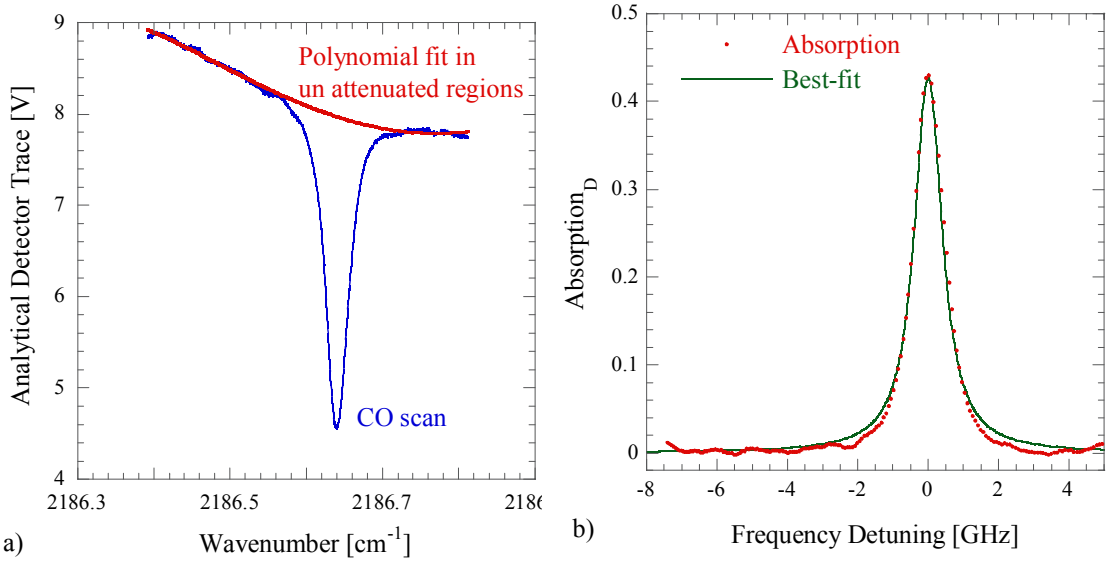

FIGURE 15 Normalization scheme D. Panel a) analytical detector traces acquired for the absorbing conditions of the test region and the polynomial fit to the un-attenuated portions of the analytical trace. b) the resulting normalized absorption with its best-fit theoretical shape. The data shown in Fig 14 is the same but processed with scheme C

the long-wave pass filter. In general, the analytical and reference traces will not match and the reference trace must be scaled. The scaling factor is obtained by considering the maximum point in the reference minus baseline trace (ref-base$_{max}$) and the correspondent point in the analytical minus baseline trace (analyt-base$_{max}$). The normalized absorption in scheme B is computed by

$$\text{Absorption}_{B} = 1 - \frac{(\text{analytical} - \text{baseline})_{\text{CO scan}}}{(\text{reference} - \text{baseline})_{\text{CO scan}} \dfrac{(\text{analytical} - \text{baseline}_{max})}{(\text{reference} - \text{baseline}_{max})}} \tag{93}$$

where the scaling factor is the second factor in the denominator. The indicated baseline is the appropriate baseline trace from the analytical and reference detectors. Panel a) in Fig. 16 shows the traces acquired from the analytical and reference detectors processed by the lock-in amplifiers. The difference in scale is due to the noise removal and amplification of the lock-in amplifiers which is different for each detector. Panel b) of Fig. 16 shows both traces after the reference has been scaled, and panel c) shows the resultant normalized absorption feature obtained through scheme B.

Scheme A is similar to B but, it requires no-CO conditions to evaluate the scaling factor. To scale the whole trace in scheme A, a scaling factor is computed at each point of the trace by using the ratio of the analytical to reference trace from the no-CO conditions. The normalized absorption for this scheme is computed by

$$\text{Absorption}_{A} = 1 - \frac{(\text{analytical} - \text{baseline})_{\text{CO scan}}}{(\text{reference} - \text{baseline})_{\text{CO scan}} \dfrac{(\text{analytical} - \text{baseline})_{\text{no-CO scan}}}{(\text{reference} - \text{baseline})_{\text{no-CO scan}}}} \tag{94}$$

At first glance, scheme A does not seem to offer advantages compared to the other schemes. However the ratio of the reference traces must be equal to one unless long time drift or temporal changes in the DFM process occur. By applying scheme A, temporal drift of the detector can be eliminated. Figure 17 shows an example of data reduction using scheme A. The two panels show the analytical and reference traces for absorbing and no-CO conditions. The scaling of reference detector is shown along with the resulting normalized absorption feature. The absorption transition shown in Fig. 17 corresponds to the same set of data as in Figs. 14 and 15. The corresponding rms deviation to the best-fit was measured to be 0.005974, 0.008762, and 0.005939 respectively for schemes C, D, A. For this particular

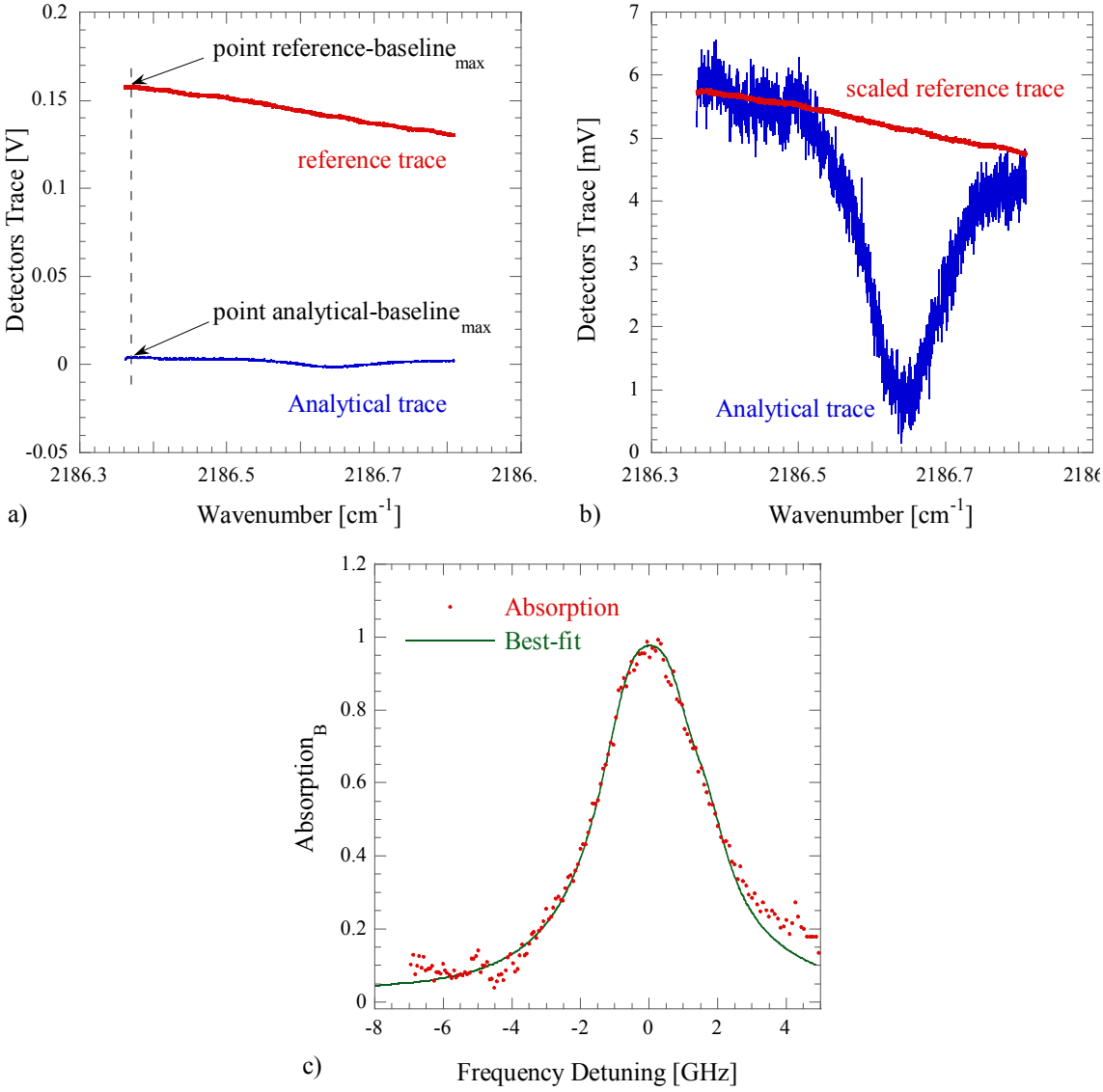

FIGURE 16 Normalization scheme B. Panel a) shows analytical and reference traces as acquired. b) analytical and reference detector traces acquired for the absorbing conditions of the test region. c) the resulting normalized absorption with its best-fit theoretical shape

set of data, scheme A performs as well as scheme C. It is seen that data for the absorption and no-CO cases was taken at different times and that there is a slight change in the slope of both detectors, but this deviation did not affect the normalization. In fact the match of the scaled reference trace to the analytical trace (Fig. 17 c)) is better than for scheme C (Fig. 14 a)).

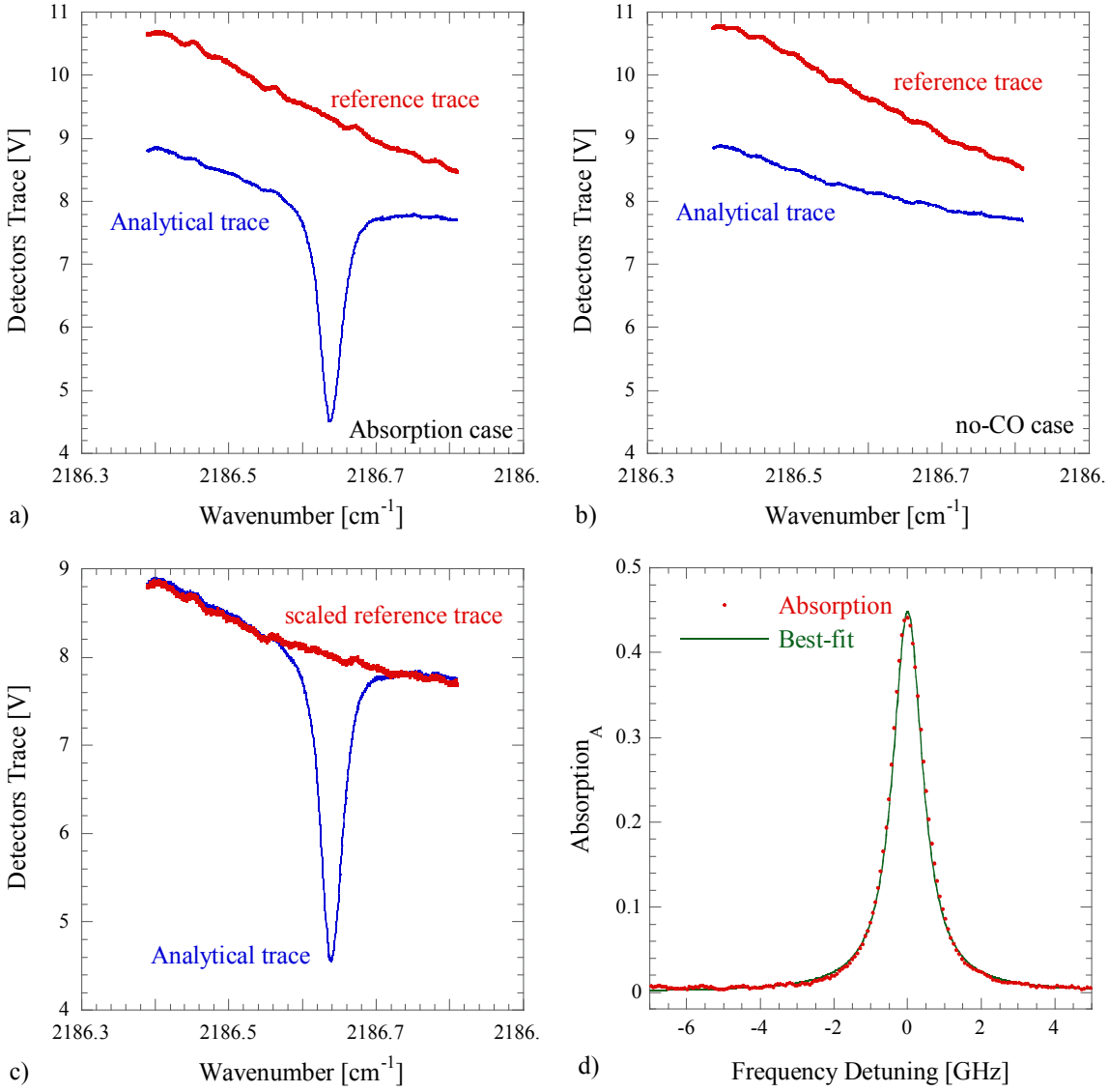

FIGURE 17 Normalization scheme A. Analytical and reference detector traces acquired a) for the absorbing case and b) for the no-CO case of the test region. Panel shows c) the scaling of the reference to the analytical trace and d) the resulting normalized absorption with its best-fit theoretical shape

After the normalized absorption was calculated, the theoretical absorption spectrum at the experimental conditions was calculated. The "Direct_Absorption" code was designed to calculate the absorption spectrum of CO and CO_2 in a given spectral region using temperature, pressure, path length, and gas mixture composition as input parameters. The best match to the data was determined by the

minimization of a least squares criterion, (73). The root-square-mean (rms) refers to the square-root of the mean squared deviation of the measured absorption spectrum from the best-fit value. The rms value of the fit was calculated by

$$\text{rms} = \sqrt{\frac{\sum_{k}^{ndp}\left[A_{k,EXP} - A_{k,CALC}(L,T,P,X_{CO},GF_{CO})\right]^2}{n_{dp}}} \tag{95}$$

where n_{dp} is the number of data points processed, $A_{k,EXP}$ is the normalized absorption measured at each data point, $A_{k,CALC}$ is the theoretically calculated absorption that depends on path length (L), temperature (T), pressure (P), CO concentration (X_{CO}), and the gamma factor for CO (GF_{CO}).

Finally, the sensor detection limit was calculated. At the detection limit, the signal-to-noise ratio (SNR) equals one, and the noise as quantified by the rms value is an indication of the minimum detectable normalized absorption. To evaluate the detection limit for the sensor, the rms value was considered to be equal to the peak absorption of the transition under "combustion conditions" for a standard path length of one meter. "Combustion conditions" was adopted as a standard in which the absorbing mixture was CO and air at atmospheric pressure and temperature of 1000 K. This standard definition of the detection limit provides a means for comparison of the performance of the sensor under different experimental conditions. Under these conditions the theoretical code was used to determine the CO concentration that is detectable for the measured rms noise. This concentration is assumed to be the sensor detection limit and will be reported with experimental results.

CHAPTER V

RESULTS AND DISCUSSION

The application of the CO sensor to single-pass mid-IR direct optical absorption measurements of the CO molecule is discussed in this chapter. The results of CO measurements in four experiments are discussed. Initial absorption measurements were performed using $CO/CO_2/N_2$ mixtures in a room temperature gas cell. Field testing of the sensor was performed in the exhaust stream of a gas turbine combustor and a well-stirred reactor (WSR). Finally, the sensor was used for CO measurements in near-adiabatic hydrogen/air CO_2-doped flames.

An important feature of the sensor is the coarse tuning capability of the ECDL since it allows the sensor to be tuned to a specific transition within the 4.2 – 4.8 μm spectral region using only two different diodes. The ECDL was delivered with an optimized wavelength of 852.831 nm and a power output of 80 mW. With this configuration the initial system produced 2.38 μW of 4.286 μm radiation. At this wavelength no CO absorption was observed, as can be seen in Fig. 1. CO_2 was detected by the sensor at these preliminary conditions. According to specifications, the ECDL with the original diode, ID JJ28, had a scanning range from 847.2 to 860 nm, with the corresponding mid-IR generation from 4.147 to 4.473 μm. To generate mid-IR radiation at longer wavelengths a second diode laser, ID 2624, with output centered at 862 nm was purchased and installed in the ECDL assembly. With the second diode the ECDL was coarse tuned to 873 nm. Near this ECDL wavelength the DFM output radiation could be tuned into resonance with transitions in the R and P branches of the fundamental CO band. The mid-IR radiation was tuned into resonance with numerous CO transitions during the course of this project, R(25), R(24), R(23), R(20), R(11), P(18), and P(19) transitions in the range 2230.5258 – 2064.3969 cm^{-1}. The transitions are listed in Table 6.

For each experimental the line selection was determined by the objectives of the test. Table 9 summarizes the sensor conditions for each set of experiments discussed in this chapter. Notice that as the

Experimental Situation	Test CO Transition		mid-IR generated power [μW]	ECDL		
	Name	Position [cm^{-1}] (μm)		Diode ID No.	Wavelength [nm]	Power [mW]
CO_2 gas cell measurements[#]	-	2332.990 (4.286)	2.388	JJ82	852.831	80.0
Room temperature Gas cell measurements	R(24)	2227.6386 (4.489)	1.766	JJ82	860.565	57.0
	R(23)	2224.7127 (4.494)	0.897	JJ82	860.782	58.0
APU Gas Turbine[*]	R(20)	2215.7044 (4.513)	1.04	JJ82	861.449	59.0
Well Stirred Reactor (WSR)	R(11)	2186.6390 (4.573)	0.089[‡]	2624	863.612	32.3
Hydrogen/Air CO_2 doped flame	P(19)	2064.3969 (4.844) [§]	0.134	2624	872.826	14.4

[#] Delivery settings of the ECDL.
[*] Significant CO_2 interference was observed in this spectral region.
[‡] Output face of the PPLN was chipped impeding full mid-IR power out of the crystal.
[§] To achieve this wavelength the grating in the ECDL was severely tilted affecting beam shape and cavity performance.

TABLE 9 CO sensor experimental parameters

ECDL is coarse tuned to higher wavelengths it suffers a significant power drop that is reflected in the loss of mid-IR power generated from the DFM process.

5.1 Room Temperature Gas Cell Measurements

The initial set of experiments was performed in a 30-cm-long gas cell at room temperature. The cell was filled with known concentrations of CO diluted in nitrogen at various pressures. Room temperature gas cell measurements were initially performed to demonstrate the sensor operation and to check the performance of the theoretical code. It was necessary to investigate numerous CO transitions for measurements in high-temperature combustion gases to find transitions free from CO_2 and H_2O interferences. For each transition that was studied, experiments were performed first in the room temperature gas cell to confirm the wavelength of the ECDL and the HITRAN spectroscopic line parameters.

For the initial gas cell measurements, the ECDL was tuned to 860.565 nm and the generated mid-IR was in resonance with R(24) fundamental band transition of CO at 2227.6386 cm^{-1}. At this wavelength, the power of the 860-nm beam, measured at the entrance face of the PPLN crystal, was 57.0 mW. The CrystaLaser beam at 1064.664 nm had a measured power of 463 mW at the entrance face of the PPLN crystal. Under these conditions the mid-IR power at the PPLN output was 1.766 μW corresponding to a normalized DFM efficiency of 0.016×10^{-3} $W^{-1}cm^{-1}$. With the beam splitter in place and the gas cell windows in the path of the analytical beam the power measured at the analytical detector was 0.62 μW.

The ECDL grating was scanned using a 265 mHz sawtooth function over a mode-hop-free tuning range of 12 GHz. Phase sensitive detection was used with the lock-in amplifiers referenced by the chopper frequency of 2.99 kHz. The lock-in amplifier time constant was 300 μs at a slope of 24 dB/oct. For these direct absorption experiments, about 15 single scans were acquired in 28.3 seconds and averaged in software. Binning of 10 neighboring oscilloscope channels was also performed in software.

At the test region a 32-cm-long gas cell was located. A photograph of the gas cell in the laboratory environment is shown in Fig. 18. The open aperture at the cell windows is 12 mm in diameter.

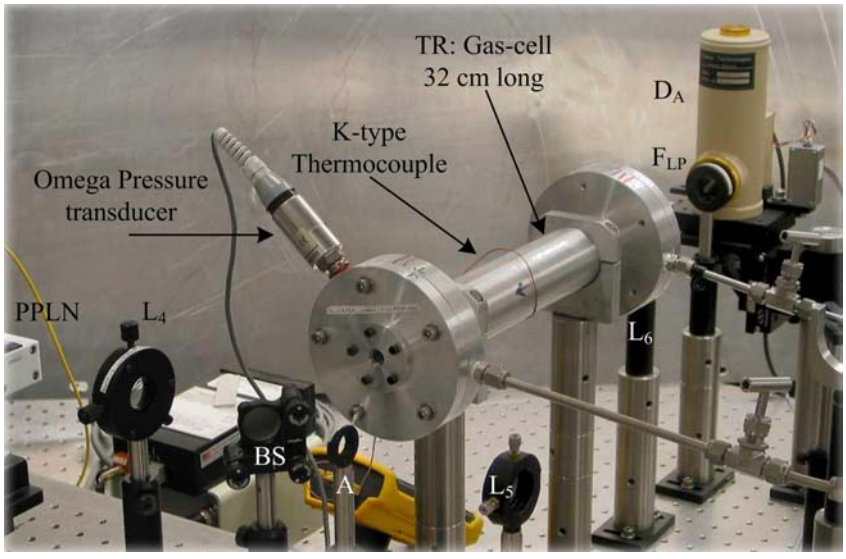

FIGURE 18 Photograph of the gas cell in the laboratory. A – Aperture, BS – Beam splitter, D_A – Analytical detector, F_{LP} – Long-wave pass filter, L – lens, PPLN – Nonlinear crystal in oven, TR – Test region

The windows are CaF_2 with 92% transmission in the mid-IR. The cell was kept at room temperature, measured to be 296 K. The cell was filled with a gas mixture of 1010 ppm CO in a buffer gas of N_2. This gas mixture was prepared by Matheson as a "certified standard" with an accuracy of 2%. The pressure in the cell was measured using an Omega pressure transducer, series PX205. This is a diaphragm transducer for absolute pressure measurements in the range 0 to 775 torr. The accuracy of this transducer was reported by Omega at 0.25% full scale or 1.93 torr for this model. This uncertainty includes linearity, hysteresis and repeatability. The pressure transducer was compared with a Convectron® tube that measures pressure down to 10^{-4} torr. For the range of pressure measurements from 50 to 500 torr, the omega pressure transducer readings (P_Ω, [torr]) were corrected using

$$P = \frac{(P_\Omega - 1.711)}{1.0139} \tag{96}$$

where P [torr] is the pressure measured using the Convectron® tube. It is important to note that the comparison of the gauges allows for better absolute pressure measurements, but the uncertainty of the pressure transducer still propagates as the uncertainty of the gas cell pressure measurements. The use of the Convectron® tube to measure directly the gas cell pressure was not recommended since the tube is sensitive to the gas composition requiring conversion factors for gases other than air.

The gas cell was filled with the 1010-ppm CO mixture at pressures of 10.03 kPa, 32.41 kPa, and 66.05 kPa. Data was processed by fitting a polynomial to the un attenuated portions of the analytical signal. This normalization scheme was selected because the traces recorded with the analytical detector for the no-CO condition showed significant drift in the un attenuated portions of the absorption trace. A sample of the resulting experimental and theoretical spectra is shown in panels of Fig. 19 for the R(24) transition of the fundamental band of CO at 2227.6386 cm^{-1}. The gas cell was kept at room temperature and the best theoretical fit of the data was obtained with a theoretical CO concentration of 1015 ppm. The estimated uncertainty in the experimental measurements for the CO concentration is on the order of 22 ppm, or 2.1% of the measured CO mole fraction. These estimates are indicative of the best-fit concentration values obtained on a series of experiments repeated on different days. This experimental uncertainty is in part due to the uncertainty of the pressure gage, the baseline drift in the spectrum, the

polynomial fit, and uncertainties in the theoretical model. This experimental value is still in good agreement with the uncertainty on the gas mixture concentration, and, as can be seen on Fig. 19, the theoretical spectral line shape, intensity and linewidth are in excellent agreement with the experimental line shape.

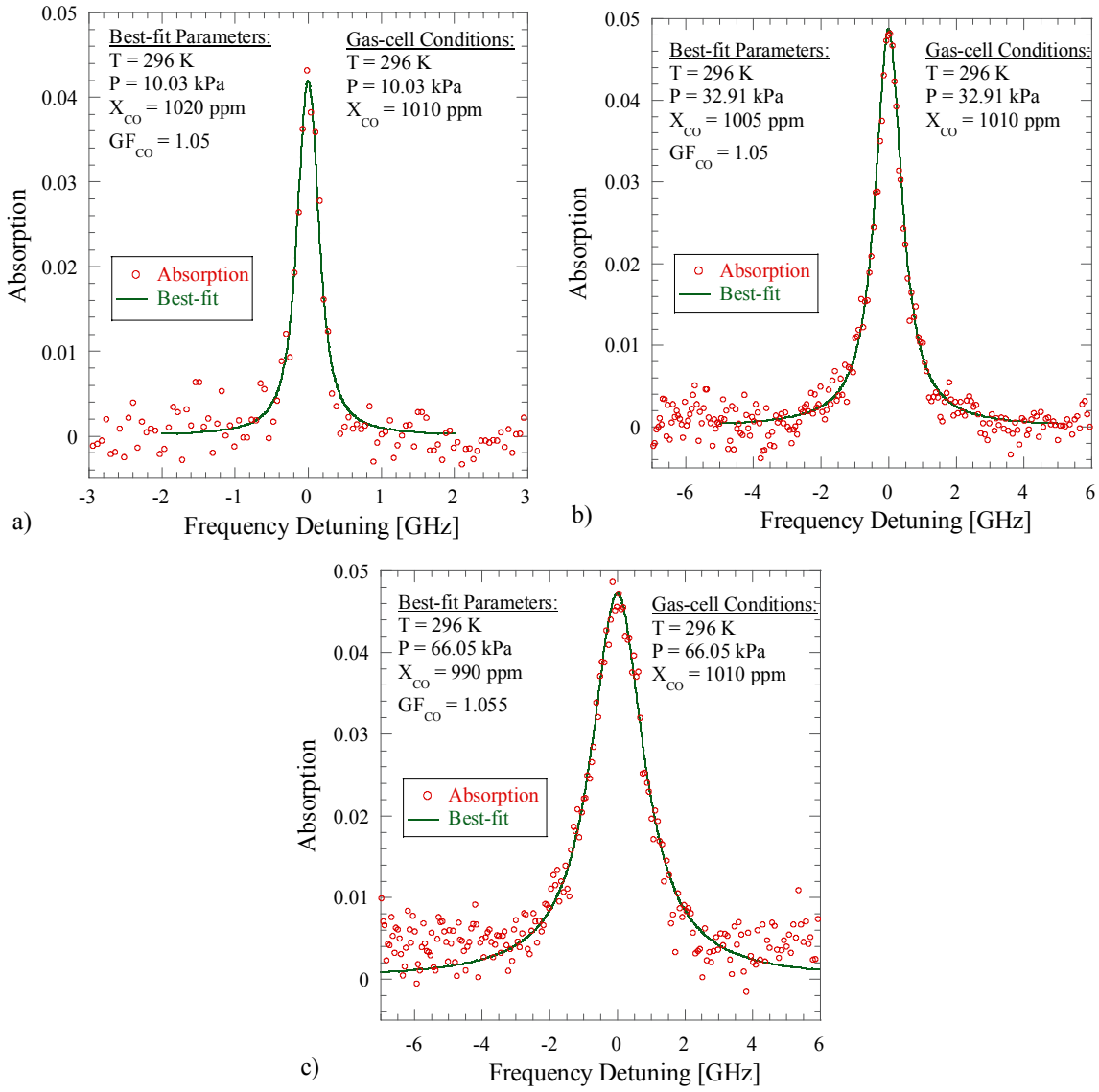

FIGURE 19 Comparison of gas cell measurements and theoretical CO absorption line shape for the R(24) transition of the fundamental band of CO at 2227.6386 cm^{-1}. On the panels the room temperature gas cell was filled to pressures: a) 10.03 kPa, b) 32.91 kPa, and c) 66.05 kPa of the 1010 ppm CO Matheson mixture. The path length through the cell was 0.32 m

For the gas cell measurements, the measured rms noise in the baseline of the fit was measured in the range from 0.001720 to 0.002242, which corresponds, respectively, to a noise detection limit ranging from 1.17 to 1.53 ppm per meter path length in 1000 K gas at atmospheric pressure, assuming a signal-to-noise ratio (SNR) of 1 at the detection limit as described in Chapter IV.

For the gas cell measurements the CO gamma factor (GF_{CO}) accounts for the fact that nitrogen (N_2) is the buffer gas and not air as assumed for the code calculations. Assuming that the gamma factor is 1.0 for this case is equivalent to assuming that nitrogen broadens CO the same as air, but nitrogen actually broadens the CO lines to a slightly greater extent. Nakazawa and Tanaka [137] compute the CO HWHM coefficients for air broadening ($\gamma^{o}_{CO\text{-}air}$) using

$$\gamma^{o}_{CO-air} = 0.79\,\gamma^{o}_{CO-N2} + 0.21\,\gamma^{o}_{CO-O2} \tag{97}$$

where the HWHM coefficients for nitrogen- and oxygen-broadening ($\gamma^{o}_{CO\text{-}N2}$ and $\gamma^{o}_{CO\text{-}O2}$) are combined. Values for the HWHM coefficient for self- and air-broadening of CO in the HITRAN database are based on measurements by Nakazawa and Tanaka.

For the "Direct_Absortion" code to simulate a CO/N_2 mixture, GF_{CO} must be adjusted considering the value of the collisional broadening FWHM. The code computes the collisional broadening FWHM by means of (76) whereas actually it is expressed by (61). Equating these two expressions and solving for GF_{CO} we obtain

$$GF_{CO} = \frac{\sum_{b} \gamma^{o}_{CO-b} X_b}{\gamma^{o}_{CO-CO} X_{CO} + \gamma^{o}_{CO-air}(1 - X_{CO})} \tag{98}$$

where b represents the actual components of the mixture. For the gas cell conditions the mixture components are CO and N_2, so the GF_{CO} can be computed from

$$GF_{CO} = \frac{\gamma^{o}_{CO-CO} X_{CO} + \gamma^{o}_{CO-N2}(1 - X_{CO})}{\gamma^{o}_{CO-CO} X_{CO} + \gamma^{o}_{CO-air}(1 - X_{CO})} \tag{99}$$

the gamma factor is dependent on the mixture composition but also dependent on the particular transition that is of interest.

	R(24)		R(23)	
	$\gamma^{o}_{CO\text{-}N2}$ [cm^{-1}/atm]	GF_{CO}	$\gamma^{o}_{CO\text{-}N2}$ [cm^{-1}/atm]	GF_{CO}
Hartmann *et al.* [138]	0.0474	1.0651	0.04859	1.0796
Predoi-Cross *et al.* [139]	0.04619	1.0379	0.04689	1.0419
Sinclair *et al.* [140]	0.04654	1.0457	0.0473	1.0510
Varghese and Hanson [64]	-	-	0.0515	1.1442
averages	0.04671	1.0496	0.0485	1.0792

TABLE 10 Evaluation of GF_{CO} using published values of the HWHM coefficient for nitrogen broadening at 296 K. Results are computed for CO transitions R(24) and R(23) of the fundamental band at 2227.6386 cm^{-1} and 2224.7127 cm^{-1} respectively. Equation (99) was used with X_{CO} = 1010 ppm

The values of the CO HWHM coefficients for self- and air-broadening are contained in the HITRAN database and were listed in Table 6. The HWHM coefficients for nitrogen broadening of various CO transitions have been determined and published in the literature. Table 10 lists some these values and the corresponding value of GF_{CO} as computed from (99), assuming a CO concentration of 1010 ppm.

From a series of measurements on the R(24) transition in the room temperature gas cell the average best-fit GF_{CO} value was 1.045. With this value of GF_{CO}, the N_2-broadened HWHM coefficient ($\gamma^{o}_{CO\text{-}N2}$) was calculated to be 0.0465 cm^{-1}/atm. This value is 1.88% lower, 0.07% lower, and 0.68% higher than the values reported by Hartmann *et al.* [138], Sinclair *et al.* [140], and Predoi-Cross *et al.* [139] respectively.

According to the HITRAN transition list, the CO absorption lines in the R branch of the fundamental band are separated approximately by 3 cm^{-1} or about 90 GHz, which is beyond the mode-hop-free tuning range of the ECDL. Thus it was not possible to observe two neighboring CO transitions in the same scan, and it was difficult to verify the wavelength of the mid-IR radiation. Therefore, the identification of a particular transition was based on wavemeter readings of the input beams. By adding CO_2 to the CO/N_2 mixture in the gas cell, some weak CO_2 transitions appeared within the mid-IR scanning range. Using the resulting spectrum that included both CO and CO_2 transitions, the wavelength of the DFM-generated mid-IR radiation was verified.

Several $CO/N_2/CO_2$ mixtures were tested in a series of room temperature experiments in the gas cell. To prepare this mixture, the gas cell was filled with the CO/N_2 mixture of the 1010 ppm bottle up to 13.35 kPa and then CO_2 was added until the gas cell pressure reached 19.99 kPa. Figure 20 shows the spectrum obtained from this $CO/N_2/CO_2$ mixture with the sensor tuned for resonance with transition R(24). In Fig. 20 the line at 0 GHz corresponds to the CO R(24) transition whereas the line at about -1 GHz corresponds to the P(48) transition of the CO_2 molecule at 2227.6048 cm^{-1} [44]. At these conditions the mixture composition in the cell was calculated to be: X_{CO} = 660 ppm and X_{CO2} = 33.33% with N_2 comprising the balance of the mixture. It is clearly seen that due to the high concentration of CO_2 the weak CO_2 transition absorbs more strongly that the CO transition. This is a clear example of spectral interference, and to avoid it the ECDL was coarse-tuned to access a different CO transition.

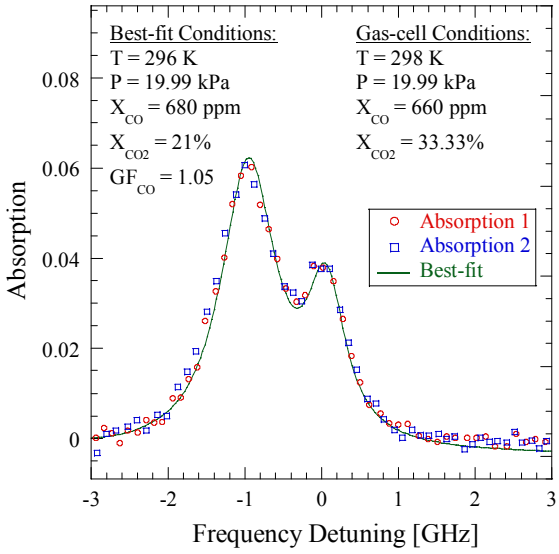

FIGURE 20 Comparison of measured and calculated absorption spectra from the R(24) transition of the fundamental band of CO at 2227.6386 cm^{-1}, seen at 0 GHz. The transition observed at -1 GHz corresponds to the P(48) transition of the CO_2 molecule at 2227.6048 cm^{-1}. The 0.32 m long gas cell was filled with a $CO/N_2/CO_2$ mixture at the indicated concentrations. This is a clear example of spectral interference

The R(23) transition in the fundamental band of CO is located at 2224.7127 cm^{-1} [44]. The ECDL was coarse-tuned to 860.782 nm to access this transition. In the neighborhood of the R(23)

transition is an absorption line observed at approximately -6 GHz, this corresponds to the P(51) transition of the CO_2 molecule at 2224.519 cm^{-1}. This is within the scanning range of the ECDL and the $CO/N_2/CO_2$ experiments were performed with these settings. To prepare the gas mixtures, the cell was evacuated and then filled to 13.33 kPa with the CO/N_2 mixture from the Matheson bottle. Then, CO_2 gas added to the mixture until the cell pressure reached 14.66, 22.66, or 26.66 kPa. For higher pressures the CO_2 transition was broadened beyond the scanning range of the system. The calculated concentrations for these mixtures are listed in Table 11 along with the best-fit values found from data. The uncertainties shown in Table 11 for the calculated values were computed based on the accuracy of the pressure gauge and the Matheson mixture.

Pressure [kPa]		X_{CO} [ppm]	X_{N2} [%]	X_{CO2} [%]
13.33		1010 ± 20	-	-
14.66	calc	918 ± 30	90.8 ± 2.3	9.09 ± 2.3
	best-fit	910	-	9.1
22.66	calc	594 ± 18	58.7 ± 1.3	41.17 ± 1.3
	best-fit	585	-	36
26.66	calc	505 ± 15	49.9 ± 1.0	50 ± 1.0
	best-fit	495	-	45

TABLE 11 $CO/N_2/CO_2$ mixtures composition. Table shows calculated concentrations along with their uncertainty and the best-fit value for the concentrations of CO and CO_2

For these tests, the ECDL was scanned at a rate of 1.32 Hz, and a 10 GHz single-mode, mode-hop-free operational range was observed. The 1064-nm beam power at the entrance face of the PPLN crystal was measured to be 312 mW, and 0.89 μW of mid-IR radiation was generated. A slow scan has the advantage allowing higher time constants for the lock-in amplifiers so that the low-pass filter bandwidth is reduced. For these experiments the lock-ins were set at 1 ms time constant with a roll-off of 18 dB/oct.

Figure 21 shows representative data from this series of experiments. As the concentration of CO_2 increases, the transition broadens and the absorption increases so that the ECDL scanning range becomes insufficient to resolve the lines. The un attenuated region is smaller and the polynomial fit is not reliable

for the far negative side in panels b and c. This is why the data in the region below -6 GHz does not follow the best-fit line. It is evident from Fig. 21 that the agreement between measured line positions, intensities, and concentrations with theoretical values falls within the uncertainties of the system.

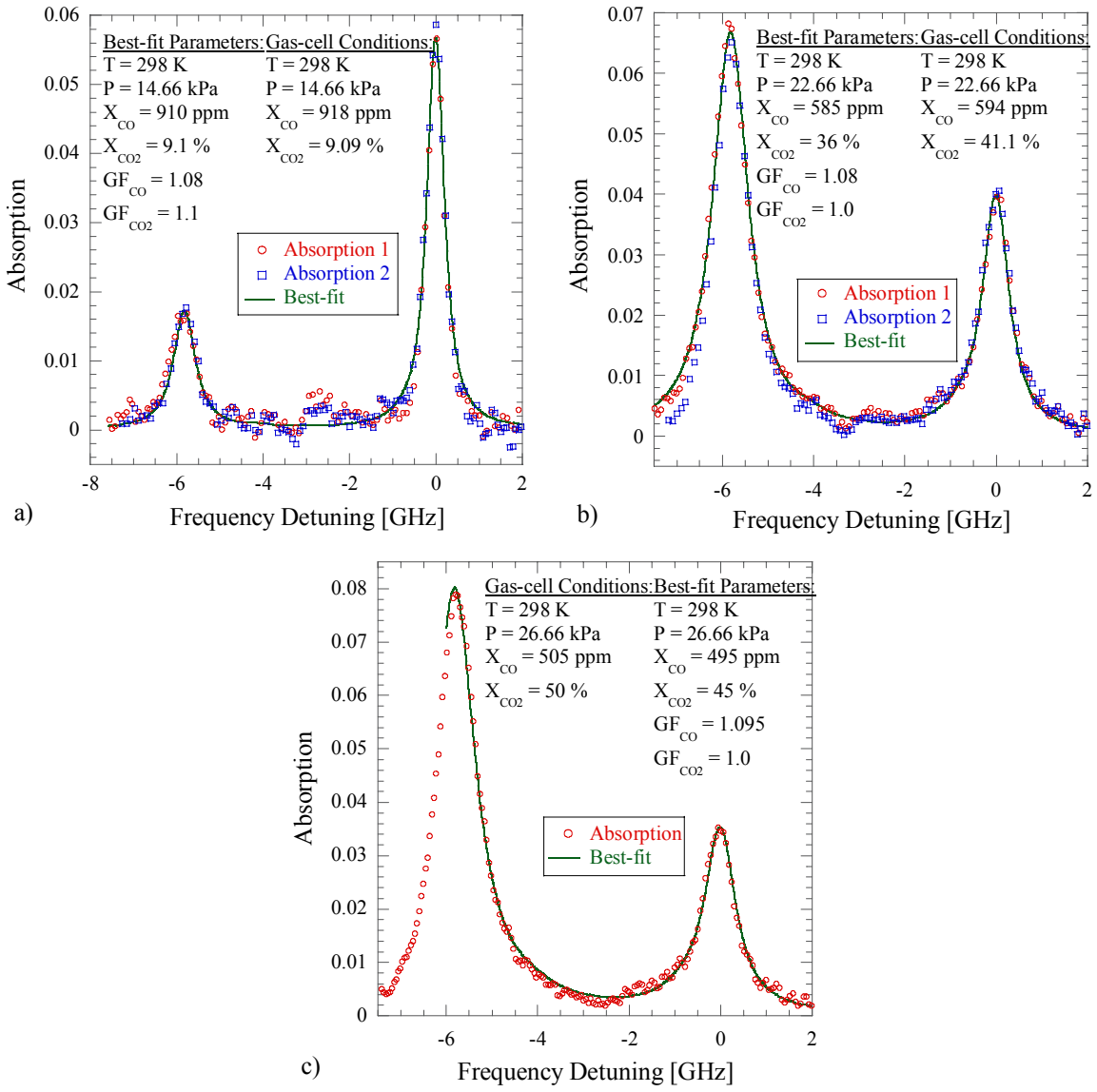

FIGURE 21 Comparison of gas cell $CO/N_2/CO_2$ mixture measurements and theoretical absorption line shapes. At 0 GHz frequency detuning the R(23) transition of the fundamental band of CO at 2224.7127 cm^{-1}. The P(51) transition from the CO_2 molecule at 2224.519 cm^{-1} can be observed at about -6 GHz frequency detuning. The room temperature gas cell was filled with the mixtures to final pressures: a) 14.66 kPa, b) 22.66 kPa, and c) 26.66 kPa. The path length through the cell was 0.32 m and mixtures compositions are given in Table 11

For these experiments, the rms noise calculated at the regions where the baseline was reliable was measured to be between 0.001841 and 0.001408, and the niose detection limit of the sensor was calculated at 1.16 to 0.89 ppm per meter of CO at 1000 K and atmospheric pressure.

For the $CO/N_2/CO_2$ mixture experiments the best-fit average value of GF_{CO} was 1.093, reflecting the inclusion of CO_2 in the mixture. Applying (98) to these $CO/N_2/CO_2$ mixtures an expression for GF_{CO} is obtained. The expression is then rearranged to obtain an expression for the CO_2-broadened HWHM coefficient ($\gamma^o_{CO\text{-}CO2}$), given by

$$\gamma^o_{CO-CO2}X_{CO2} = \gamma^o_{CO-CO}X_{CO}(GF_{CO}-1) + \gamma^o_{CO-air}(1-X_{CO})GF_{CO} - \gamma^o_{CO-N2}(1-X_{CO}-X_{CO2}) \qquad (100)$$

In the next section measurements of the R(23) transition in CO/N_2 mixtures will be discussed, there the $\gamma^o_{CO\text{-}N2}$ for R(23) is obtained to be 0.0502 cm^{-1}/atm. With this result and the measured GF_{CO}, the HWHM coefficient for CO_2-broadening of CO fundamental band transition R(23) was calculated 0.0461 cm^{-1}/atm. It compares within 4.3% of the interpolated value 0.0465 cm^{-1}/atm computed from Hartmann *et al.* [138] theoretical predictions. Experimental data for the $\gamma^o_{CO\text{-}CO2}$ has been published [137, 141, 142] for CO lines in the fundamental band with m ≤ 20 (i.e. m = J+1 for R branch transitions) so that this measurement for $\gamma^o_{CO\text{-}CO2}$ can not be compared.

5.1.1 Evaluation of the effect of GF_{CO} in the fitting procedure

The gamma factor GF_{CO} has been included in the "Direct_Absorption" code but its meaning is obscure in terms of how the line profile and the fitting parameters are changed by its selection. Physically, the gamma factor was included to scale a known absorbing gas mixture to the value of an undefined mixture thus, including the collisional effect of other molecules present in the undefined gas mixture. This section has been prepared to better understand the implications of changes in this factor on the fitting procedure.

Since high quality data for transition R(23) in the fundamental band of CO at 2224.7127 cm^{-1} are available, the effects of changes in GF_{CO} on fitting parameters are assessed for this transition. Calculated values for the GF_{CO} factor are given in Table 10. The listed values were computed based on published

HWHM coefficients for N_2-broadening ($\gamma^{o}_{CO\text{-}N2}$) and on the gas mixture composition of the Matheson certified bottle 1010 ppm of CO in balance N_2. Figure 22 shows the line shape obtained when various GF_{CO} values are used for the theoretical calculation of absorption in the 0.32 m long gas cell at 296 K filled with 13.33 kPa of the known gas mixture. It is observed that as the GF_{CO} increases the absorption profile becomes Lorentzian. Based on the Voigt parameter criterion ($a > 2$) for Lorentzian profiles, for values of $GF_{CO} > 1.08$, the main broadening mechanism for this transition is collisional broadening. Using expression (76) for the collisional broadening FWHM, the Voigt parameter given by (64) can be expressed as

$$a = 2\sqrt{\ln 2}\left(\frac{296}{T}\right)^{n} P \cdot GF_{CO} \cdot \frac{\gamma^{o}_{CO-CO} X_{CO} + \gamma^{o}_{CO-air}(1 - X_{CO})}{\Delta\omega_{D}} \tag{101}$$

There is a linear relationship between GF_{CO} and the Voigt parameter. Thus, GF_{CO} has the same qualitative effect on the line shape as the pressure.

The three solid lines in Fig. 22 correspond to the minimum, maximum, and average values of

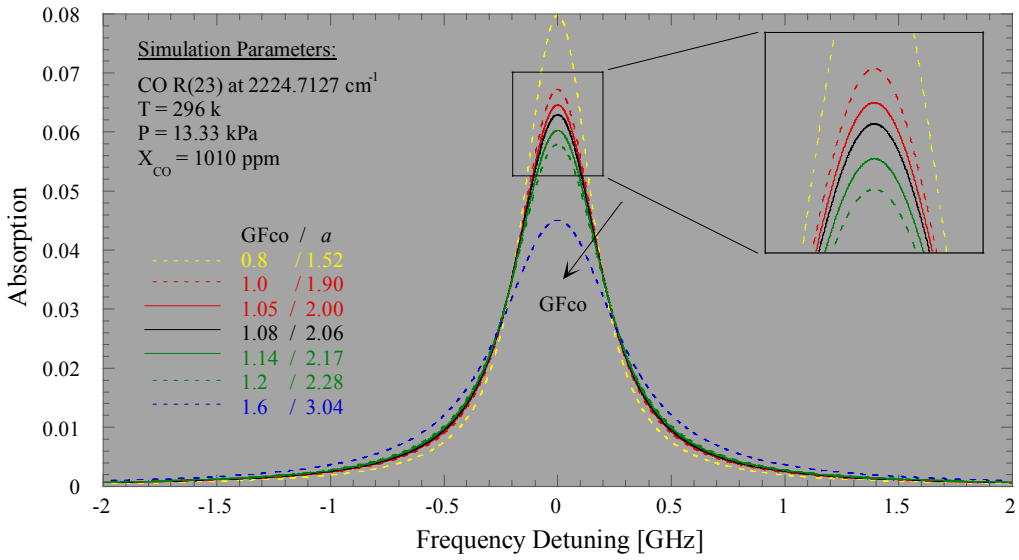

FIGURE 22 Line shape dependence on GF_{CO}. Theoretical absorption line shape for R(23) transition of the fundamental band of CO at 2227.7127 cm^{-1}. Absorption conditions are in the 0.32 m long gas cell at 296 K, 13.33 kPa of 1010 ppm CO and balance N_2. The GF_{CO} indicated by broken lines indicate the maximum, minimum and average GF_{CO} values from Table 10. The Voigt parameter a calculated at each GF_{CO} is included

GF_{CO} given in Table 10. These three profiles are very close to each other especially on the wings but they are clearly distinguishable in the vicinity of the peak absorption. Therefore the peak absorption of the transition is an important feature to match when adjusting GF_{CO} since it allows fine tuning of the rms noise. For instance, the rms deviation of traces GF_{CO} = 1.05 and 1.14 from the trace GF_{CO} = 1.08 are 0.00048 and 0.00076 respectively. These rms deviations are about one order of magnitude smaller than the usual rms noise for the direct absorption experiments.

For an actual data fitting procedure the peak absorption of the recorded feature has to be matched by least-square fitting. To better observe the effect of GF_{CO} on the fitting procedure, Fig. 23 shows how the line profile broadens and become Lorentzian as the GF_{CO} increases while the peak absorption value is held constant. In Fig. 23, the peak absorption at 0.063 is obtained for the 0.32 m gas cell at 296K filled with 13.33 kPa of 1010 ppm CO in balance N_2 mixture assuming a GF_{CO} =1.08. The other traces are adjusted so for each value of GF_{CO} the CO concentration is varied to match the peak absorption. From the best-fit value of CO concentration in Fig. 23 the relationship between GF_{CO} and X_{CO} can be determined.

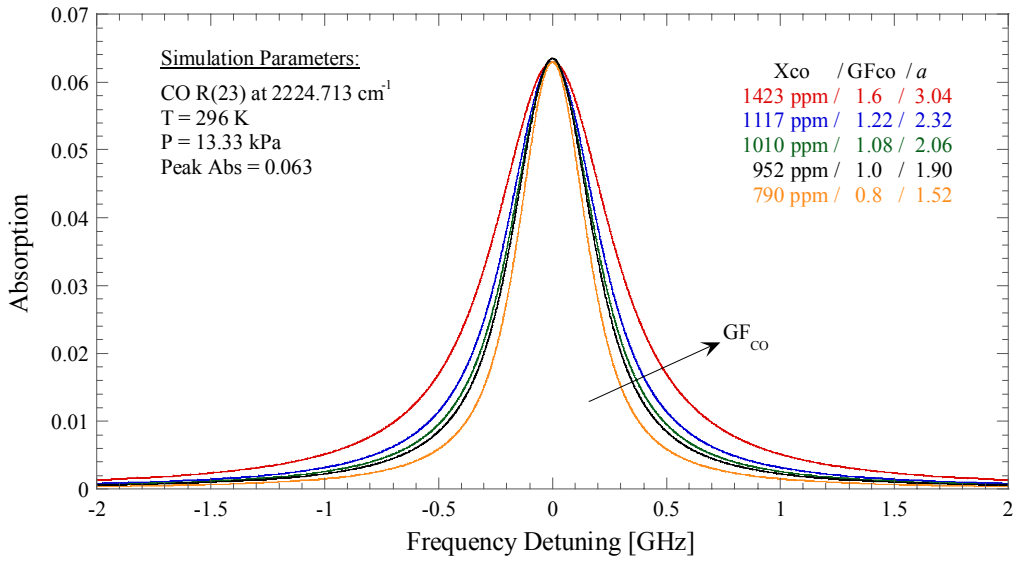

FIGURE 23 The R(23) absorption line shape as GF_{CO} is increased and CO concentration is adjusted so that the peak absorption is constant. The peak absorption value of 0.063 for the CO R(23) transition was obtained from absorption in the 0.32 m gas cell at 296 K and 13.33 kPa with a CO concentration of 1010 ppm

Figure 24 is produced by repeating these calculations at different gas cell pressures. The peak absorption is computed at each gas cell pressure under conditions X_{CO} = 1010 ppm, GF_{CO} = 1.08, T = 296 K, L = 0.32 m. The linear relationship between GF_{CO} and X_{CO} when the peak absorption is kept constant at a given pressure is observed in Fig. 24. In addition to the observed linearity, Fig. 24 shows that for $P \geq 13.33$ kPa the slope of the X_{CO} versus GF_{CO} line is essentially constant.

After this theoretical study of the effect of GF_{CO}, a series of experiments were performed in the room temperature gas cell for the CO R(23) transition at 2224.713 cm^{-1}. Figure 25 shows that for the gas cell conditions, pressures larger than 13.33 kPa will produce Lorentzian profiles, and the peak absorption approaches a value of 0.0688 for pressures larger than 39.99 kPa. The broadening of the transition is dominated by the Doppler effect in the range $0 < P < 6.66$ kPa. Therefore, testing at 6.66 and 13.33 kPa allowed us to observe both Gaussian and Lorentzian profiles. With these testing pressures the peak absorption was as large as possible for the Gaussian at 6.66 kPa, while at 13.33 kPa the peak absorption has not yet reached its high-pressure value allowing for a better fit of the CO concentration and GF_{CO}

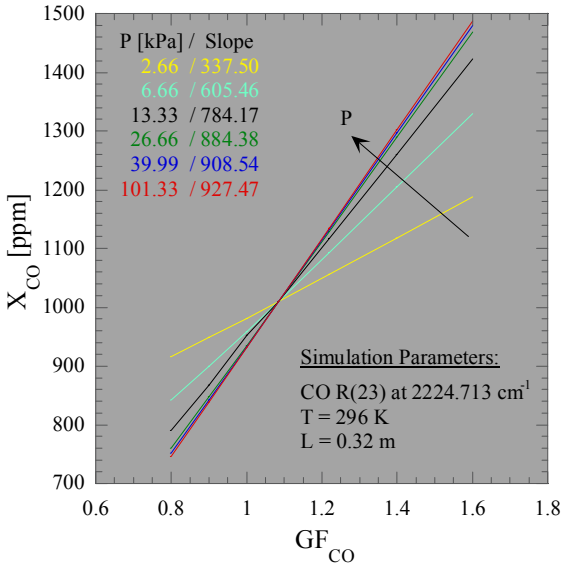

FIGURE 24 Linear variation of CO concentration with GF_{CO} when the peak absorption is kept constant. For each pressure line the peak absorption was obtained with parameters T = 296 K, L = 0.32 m, X_{CO} = 1010 ppm, GF_{CO} = 1.08

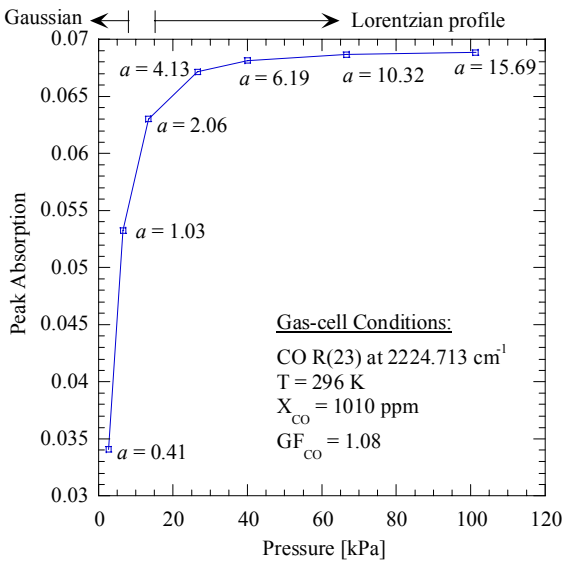

FIGURE 25 For the indicated gas cell conditions the figure shows the peak absorption as a function of the pressure in the cell. The Voigt parameter (a) indicates the shape of the transition, i.e. Gaussian ($0 < a < 1$) or Lorentzian ($a > 2$)

parameters.

For these experiments the ECDL was tuned to 860.782 nm with an output power of 58 mW, and a 10 GHz mode-hop-free tuning range. The power of the 4.494 μm DFM-generated mid-IR beam was measured to be 890 nW. The ECDL was scanned at 1.32 Hz and data was averaged in the oscilloscope over 8 traces, with a total acquisition time of 3 s. As can be seen in Fig. 22 the R(23) transition is approximately 3 GHz wide so that the un attenuated region is about 7 to 8 GHz. A 3rd degree polynomial was fit to the spectrum in the un attenuated region to evaluate the normalized absorption.

Experimental and best-fit theoretical absorption spectra are compared in Fig. 26. Panel a) shows two of the experimental traces at 6.66 kPa, and panel b) shows two experimental traces at 13.33 kPa. The theoretical best-fit in Fig. 26b) has a GF_{CO} very close to the published average value of 1.08. However, for the 6.66 kPa case the best-fit GF_{CO} was 1.21. For these gas cell measurements at 6.66 and 13.33 kPa the best-fit CO concentration falls within the 20 ppm uncertainty of the gas mixture. The rms noise values

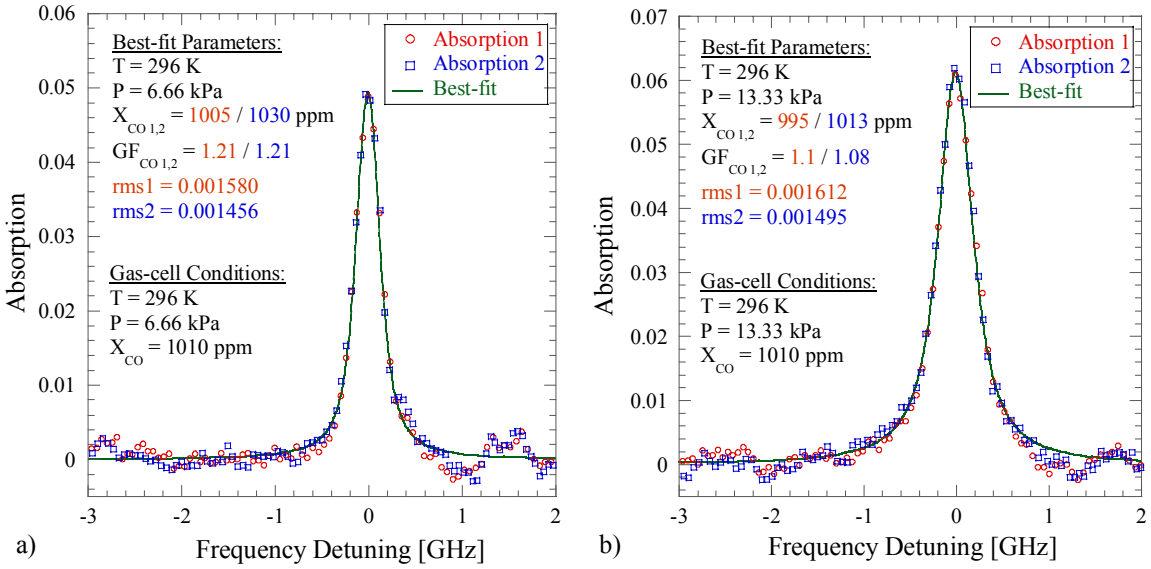

FIGURE 26 Comparison of the measured and calculated CO absorption transition R(23) of the fundamental band at 2224.7127cm^{-1}. Experiments were performed in the 0.32 m room temperature gas cell filled with 1010 ppm CO in N_2 at pressures: a) 6.66 kPa and b) 13.33 kPa. GF_{CO}, X_{CO}, and rms noise of the fit are shown for both measured data sets Absorption 1 and 2

of these fits are in the range 0.001456 to 0.001612, corresponding to a sensor noise detection limit of 0.915 to 1.015 ppm per meter for gas at 1000 K and atmospheric pressure, assuming SNR = 1.

As previously discussed, the relationship between GF_{CO} and X_{CO} is linear. Therefore, by reducing the gamma factor the best-fit CO concentration will drop. For the 13.33 kPa case, Fig. 26b), the best-fit GF_{CO} was close to the published average value and by setting GF_{CO} = 1.079 the best-fit resulting CO concentration was expected to be within the gas mixture uncertainty. In the 6.66 kPa case, Fig. 26a) the best-fit GF_{CO} was 1.21. Using the data in Fig. 24, it was expected that the best-fit CO concentration would drop about 80 ppm when GF_{CO} was changed from 1.21 to 1.079. To evaluate the effect of GF_{CO} in the fitting procedure for real data, the GF_{CO} was set to 1.079 and the fits were repeated. Figure 27 shows the resulting fits to the same sets of data presented in Fig. 26. In Fig. 27a) the measured data was not included for purposes of clarity but comparison can be made with the best-fit curve from Fig. 26a).

Table 12 summarizes the results from Figs. 26 and 27. For gas cell measurements at 13.33 kPa, the adjustment of GF_{CO} to 1.079 has a very low impact both on the CO concentration and the noise limit of

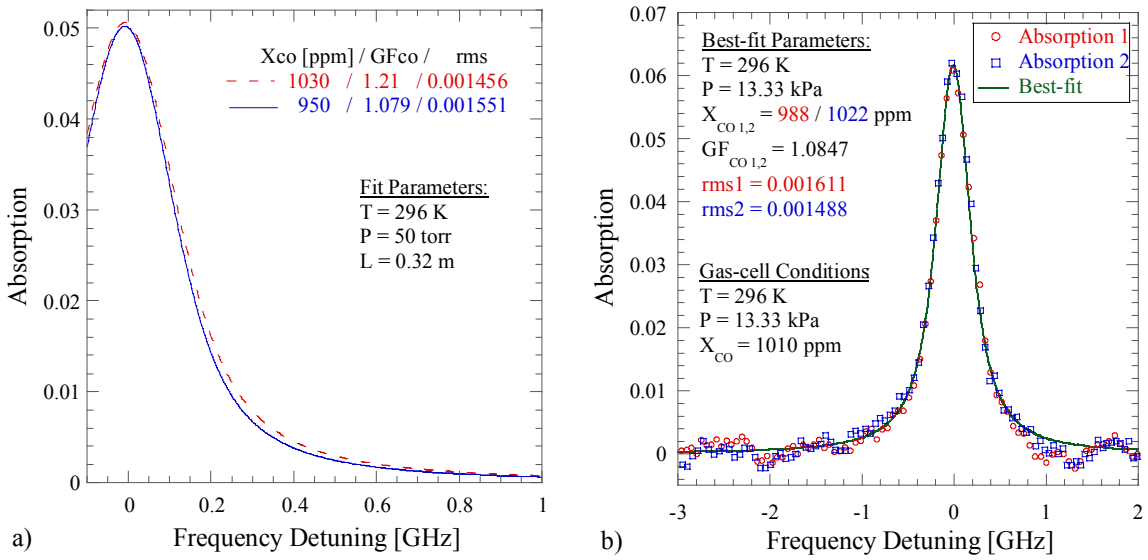

FIGURE 27 Comparison of the measured and calculated CO absorption transition R(23) at 2224.7127 cm^{-1}. Data in panels a), b) is the same as in panels a) and b) of Fig. 26 respectively. However, the fits are produced by seting $GF_{CO} = 1.079$ to evaluate the effect on the best-fit CO concentration. Panel a) does not show the data for clarity. The curve at $GF_{CO} = 1.21$ corresponds to the best-fit curve presented in Fig. 26a)

the sensor. As observed in Figs. 26b) and 27b) the fit "looks" very similar. For the measurements at 6.66 kPa, the best-fit is indicated by the shape of the absorption trace. Changing GF_{CO} from 1.21 to 1.079 requires a CO concentration drop in the order of 7% to obtain a best fit to the experimental spectrum shape. For the best-fit curve with $GF_{CO} = 1.079$, the rms noise was slightly higher than the best-fit for $GF_{CO} = 1.21$, and the noise detection limit of the sensor increased by approximately 0.07 ppm per meter for gas at 1000 K and atmospheric pressure.

Finally, using the best-fits for all the measurements performed on the R(23) transition of CO, the GF_{CO} averaged to 1.11. The average CO concentration was 1004 ppm with a standard deviation of 15 ppm giving an uncertainty less than 2%. The average GF_{CO} and CO concentration were used in (99) to find the nitrogen broadening HWHM coefficient for CO ($\gamma^{o}_{CO\text{-}N2}$). The calculated value for $\gamma^{o}_{CO\text{-}N2}$ was 0.0502 cm^{-1}/atm falls within 6.3% of the values reported in literature (see Table 10). It is 2.41% lower than the value of Varghese and Hanson [64], but 3.43%, 7.18%, and 6.25% higher than the values from Hartmann *et al.* [138], Predoi-Cross *et al.* [139], and Sinclair *et al.* [140] respectively. The averaged

	Fig.	GF_{CO}	X_{CO} [ppm]	ΔX_{CO} [%] [#]	rms	Noise limit[*]
13.33 kPa						
Absorption 1	26b)	1.1	995	-	0.001612	1.015
Absorption 1	27b)	1.079	988	-0.70	0.001611	1.015
Absorption 2	26b)	1.08	1013	-	0.001495	0.941
Absorption 2	27b)	1.079	1022	+0.88	0.001488	0.938
6.66 kPa						
Absorption 1	26a)	1.21	1005	-	0.001580	0.995
Absorption 1	-	1.079	935	-6.96	0.001613	1.015
Absorption 2	26a)	1.21	1030	-	0.001456	0.915
Absorption 2	27a)	1.079	950	-7.76	0.001551	0.977

[#] Column ΔX_{CO} indicates the percentage of change in X_{CO} when GF_{CO} = 1.079 referenced to the best-fit adjustment in Fig. 26.

[*] Noise detection limit in [ppm] is evaluated for 1 meter of path length in a gas mixture at 1000 K and atmospheric pressure.

TABLE 12 Summary of the fits in Figs. 26 and 27. Comparing the effect of GF_{CO} in the best-fit determination of CO concentration and fit rms standard deviation

sensor noise limit was computed to be 1 ppm per meter of gas at 1000 K and atmospheric pressure assuming SNR = 1.

5.2 Field Demonstrations

After the excellent results obtained from the room temperature gas cell measurements, the sensor was tested in real combustion environments where vibrations, high temperatures, remote operation, and spectral interferences were encountered. The sensor was transported to the test facilities of a gas turbine auxiliary power unit (APU) at Honeywell Engines and Systems in Phoenix, AR and a well-stirred reactor (WSR) at Wright-Patterson Air Force Base in Dayton, OH. Installation of the sensor in these facilities and results from both tests are the topic of this section.

One of the main concerns for the field tests of the sensor was the target CO transition. In the hot products from combustion, water vapor (H_2O) and carbon dioxide (CO_2) are always present. An isolated CO transition with minimal spectral interferences was required for reliable CO measurements. Figure 28 shows a HITRAN survey of the three molecules. For clarity, the line intensity of H_2O has been multiplied

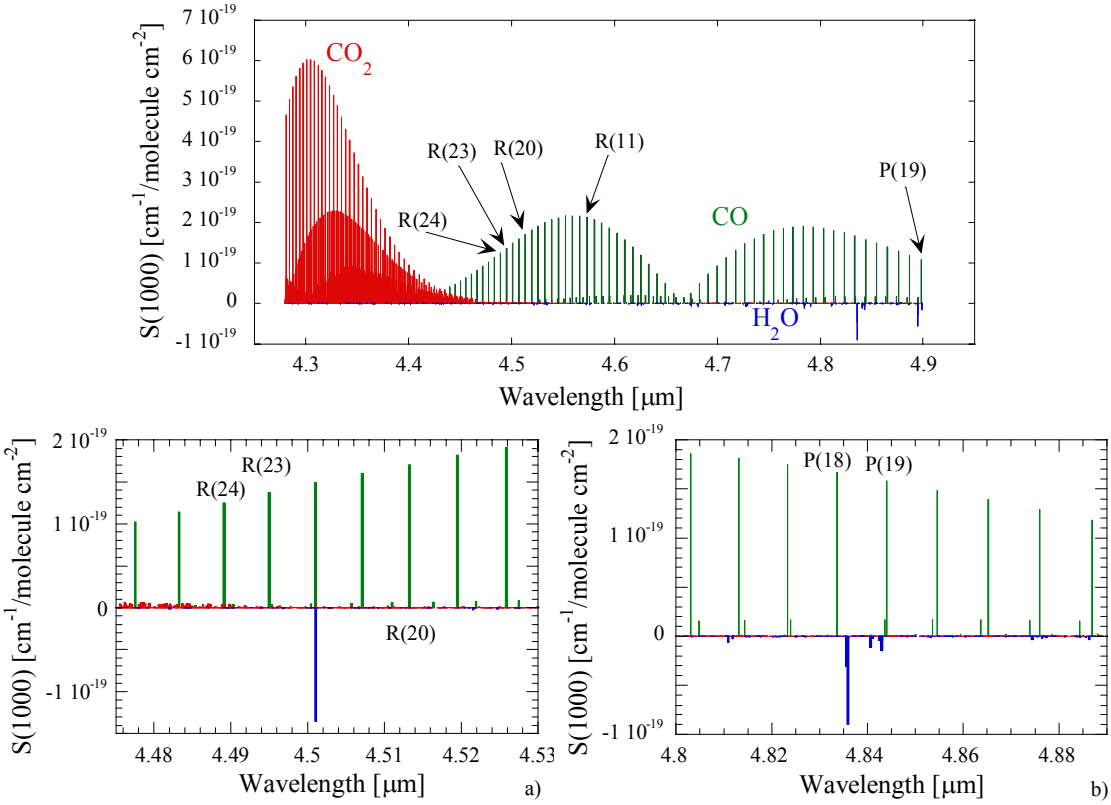

FIGURE 28 HITRAN [44] spectral survey of transition positions and their intensity at 1000 K for CO, CO_2, and H_2O in the 4.3 to 4.9 μm spectral range. For illustration purposes, the line intensity (S [cm^{-1}/molecule cm^{-2}]) for H_2O was multiplied by a factor of -2. The labeled CO transitions correspond to some of the interrogated lines in this project (see Table 6). Panels provide a closer look to regions a) 4.47 – 4.53 μm and b) 4.8 – 4.89 μm

by a factor of -2. From this survey it is clear that although H_2O is present in the gas mixture its spectral interference with CO is mostly negligible for the transitions of interest in this project (see Table 6). On the contrary, CO_2 interferes significantly with CO in the vicinity of the R branch. As previously observed in the gas cell experiments, CO_2 transitions were observed near the R(24) and R(23) CO transitions. Thus, to avoid CO_2 interference the sensor system was tuned to the highest wavelength possible.

5.2.1 Gas turbine exhaust measurements

At the Honeywell facilities in Phoenix Arizona, a 90 kW gas turbine auxiliary power unit (APU) was installed in an engine test cell. The test cell facility is a concrete building that houses the gas turbines

for standard performance tests. In the cell, the gas turbine is isolated and remotely controlled and monitored. The power output of the turbine is loaded with a generator and compressor. The JP-8 fuel flow into the turbine is controlled to maintain constant speed. Loading the gas turbine forces the fuel to increase, changing the equivalence ratio of the combustion process. By this means the combustion conditions are controlled and different exhaust compositions are obtained. The composition of the products is an indication of the efficiency of the combustion process and carbon monoxide measurement in the exhaust stream is especially important. CO absorption measurements were performed at the end of a 1.80 m long, 0.25 m diameter exhaust tube running between the engine and the exhaust vent.

To validate the measurements with the CO absorption sensor, the Honeywell Emissions truck was used to measure the concentration of the exhaust gases by means of extractive sampling. Four physical probes were placed in the exhaust tube approximately 0.90 m upstream from the beam location. The samples collected by the probes were drawn through a heated line to the emissions truck outside the test cell. CO and other stable species were measured by traditional analyzers. The concentrations of CO, CO_2, HC, O_2, NO, and NO_x were measured and recorded.

Thermocouples were used to measure the temperature of the exhaust gases along the path of the beam. Three K-type thermocouples were mounted at three different radial locations at the exit of the exhaust tube to determine the temperature variation along the absorption path. This procedure allowed us to measure a more accurate range on the temperature of the gas. These measurements showed that the temperature close to the center of the stack was about 10 K higher than temperature by the walls of the duct. The thermocouples were not corrected for radiation since the measured temperatures were never higher than 760 K, and half the thermocouple is exposed to cooler surroundings so that correction for radiation is small. The temperature varies along the diameter of the exhaust duct and absorption spectroscopy is a path averaged measurement but the small variation in temperature will have a minimal effect on the measured CO concentration.

The extremely harsh environment near an operating gas turbine raised several other issues with regards to the operation of the sensor. First, all sensor control and data collection had to be performed remotely from the control room adjacent to the test cell. Long cables were run from the controllers to the

lasers and from the detectors to the data acquisition oscilloscope. Second, since the operation of almost every part of the sensor is extremely sensitive to temperature, the high temperatures near the engine and exhaust required a means of cooling the sensor. The third and most critical issue was vibration isolation. When the gas turbine was operating, the mechanical vibrations in the test cell degraded the performance of the laser systems. The sensor was mounted on optical benches and vibration isolation pads to reduce the level of vibration transmitted to the sensor.

The sensor was set on 0.60 x 1.22 m optical breadboard in preparation for the field tests. An aluminum enclosure was fabricated and installed around the sensor to shield the laser systems and optics from the high temperatures of the combustion environment. During testing, clean compressed air was directed through the sensor housing at low flow rate, providing the necessary cooling and maintaining a stable operating temperature for the sensor components.

In the cell, the sensor was mounted on an optical cart next to the engine. The analytical beam passed through the exhaust gases approximately 5 mm from the edge of the exhaust tube along the diameter of the tube. This minimized uncertainty in the path length, which was taken to be the diameter of the tube, 0.25 m. For the CO sensor a single pass through the test region was required. The analytical detector was placed on the opposite side of the exhaust stream, mounted on the same optical table as the sensor enclosure.

For this field test the ECDL was coarse tuned to 861.449 nm. This setting was at the edge of the coarse tuning range of the diode. The mid-IR beam was in resonance with the R(20) transition of the fundamental band of CO for this ECDL wavelength. The spectral simulation showed that the line R(20) was not free of spectral interference from CO_2 but the neighboring CO_2 transitions were much weaker than the for R(23) and R(24) transitions, see HITRAN survey as shown in Fig. 28. Once the system was aligned the mid-IR power was about 1 μW and was distributed to the analytical and reference detectors. The ECDL was scanned at a rate of 1.34 Hz with a single mode scanning range of 10 GHz. Data was averaged in software over 10 scans for a total acquisition time of 3.7 s.

When the diode-laser-based CO sensor was in place and operating, the gas turbine was ignited. At the idle condition the gas turbine produces the most CO and the vibration level is lowest. However, for

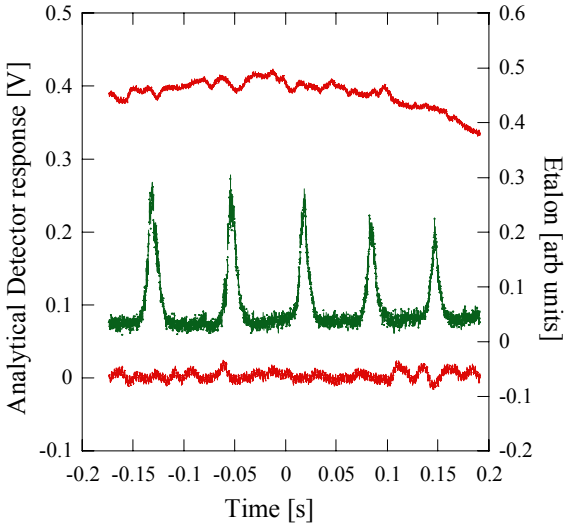

FIGURE 29 Oscilloscope view of the analytical detector for a test of the gas turbine at the full-load condition. The traces include the analytical detector, baseline, and the etalon trace. Noise in this traces obscures the absorption feature occurring at about 0 seconds

this condition the performance of the sensor was highly affected by mechanical vibrations in the room. At the 45-kW "half-load" condition, the noise in the test cell increased to the point where the lock-in amplifiers had to be re-adjusted since they overloaded. At higher engine-load conditions, vibrations were more severe and interfered with the sensor operation, making it impossible to differentiate between the absorption line and noise. For instance, Fig. 29 shows the analytical signals and its baseline acquired at the full-load, 90-kW condition. The noise in the traces covers any absorption feature. The etalon trace is also shown in Fig. 29.

For lower-load conditions, some traces were not as noisy. Figure 30 shows results from measurements on the gas turbine engine at the half-load condition. A comparison of measured and calculated absorption line shapes is shown for the R(20) CO transition in the fundamental band at 2215.704 cm^{-1}. The absorption peak located at 0 GHz frequency detuning corresponds to the CO R(20) transition. The theoretical line shown was calculated with the "Direct_Absorption" code which incorporated spectroscopic line parameters for CO and CO_2 form the HITRAN Database [44]. Even when carbon dioxide (CO_2) transitions in this region of the spectrum are about two orders of magnitude weaker

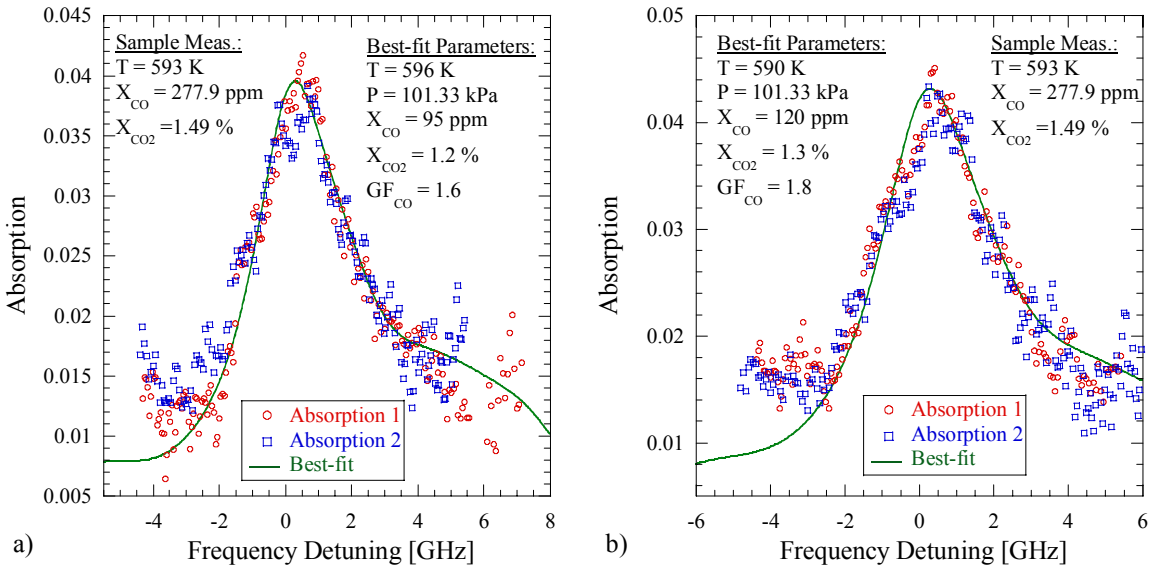

FIGURE 30 Measured and calculated absorption line shape for the R(20) transition of the fundamental band of CO at 2215.7044 cm^{-1} from the gas turbine engine exhaust when running at the half-load condition. For these fits, the path length was assumed 0.25 m, and the temperature was assumed to be the average of the measured temperatures in the exhaust

than the CO transitions, the CO_2 concentration is high enough so that CO_2 absorption is evident in the spectrum. The presence of CO_2 is the reason for the observed broadband absorption and why no un attenuated regions were observed.

The theoretical curves shown in Fig. 30 were calculated using the best-fit parameters indicated with a path length of 0.25 m. The gamma factor is much greater than 1, as expected due to the variety of molecules present in exhaust, but with this quality of data it cannot be computed accurately. In addition the lack of information on the actual gas mixture composition impedes a theoretical approach.

The agreement shown in Fig. 30 in terms of the line width and line shape is an indication that we are detecting the CO molecule. The best-fit CO concentration was a factor of 3 lower than the probe sampling results, but the probe was located 0.90 m upstream of the exhaust exit. CO_2 interference cannot account for the discrepancy between diode laser and probe results. Including the CO_2 absorption in the fitting routine would cause an increase in the CO concentration needed to match the recorded spectrum from the diode laser measurements. For the gas turbine experiments, probe measurements of CO did not

agree with absorption measurements despite the good agreement between experimental and theoretical CO line shapes. Noise in Fig. 30 is on the order of 0.0036 rms standard deviation, which corresponds to 1.93 ppm per meter of CO at 1000 K and atmospheric pressure assuming SNR = 1 at the detection limit.

During testing, it was observed that the operation of the sensor and hence its sensitivity was influenced by the vibrations from the engine. It is clear from the data, however, that this technology can be implemented in this type of environment. The operational demonstration of this sensor was successful but much improvement in the sensor system and operation is required.

5.2.2 Well-stirred reactor exhaust measurements

Field testing of the sensor was also performed at Wright-Patterson Air Force Base (WPAFB). CO concentration measurements in the exhaust of a well-stirred reactor (WSR) were performed. Given the experience gained as a result form the tests in the gas turbine, special attention was given to damping of mechanical vibrations as well as to cooling of the sensor. Again, the CO sensor was mounted on the 0.60 m by 1.20 m optical breadboard and was enclosed by the same aluminum case. During testing, a flow of dry air was directed into the enclosure to maintain a stable operating temperature. Vibrations at the WSR facility were not as severe as those in the gas turbine. In addition, the sensor was set on an optical bench that offered better damping than the previous mounting in the gas turbine cell.

The exhaust gases from the WSR exited through a 0.05 m diameter, 0.30 m long ceramic tube. The mid-infrared beam was directed along the diameter of the tube approximately 3 mm above the tube exit. A B-type thermocouple with 0.02 mm diameter wires was placed in the exhaust at the same height as the beam but about 4 mm to the side. An extractive probe was located in the center of the exhaust stream approximately 2 cm above the beam height. The probe was operated in conjunction with an NDIR analyzer (VIA 510 from Horiba Instruments). The uncertainty of this probe-analyzer system was estimated to be 3%. With this instrumentation, comparison between the mid-IR CO sensor and traditional probe sampling analysis techniques were performed. The photograph in Fig. 31 shows the sensor installed next to the WSR.

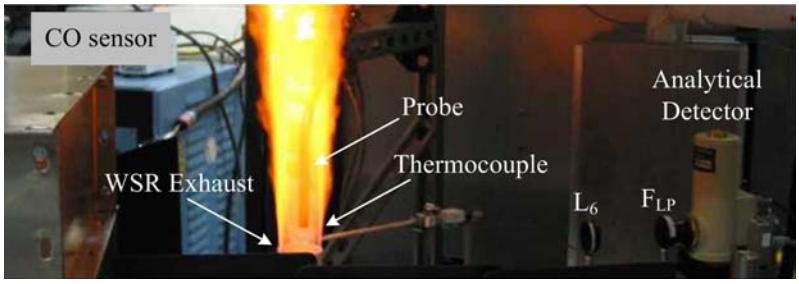

FIGURE 31 Photograph of the CO sensor installed at the well-stirred reactor (WSR) facilities

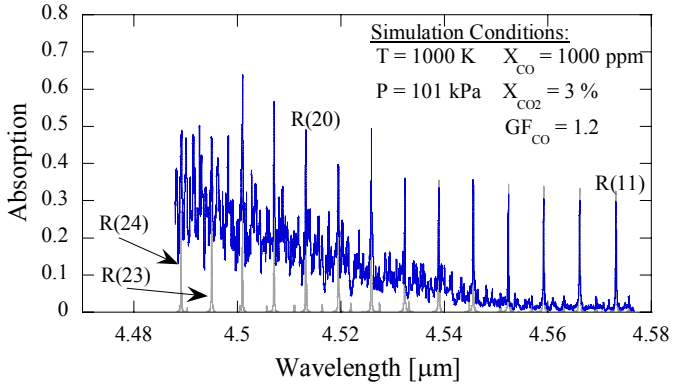

FIGURE 32 Theoretical spectrum for CO/CO_2 in the 4.489 to 4.575 μm range. The spectrum was calculated for a mixture 1000 ppm CO and 3 % CO_2 at 1000 K and atmospheric pressure. The path length was assumed to 0.20 m and the GF_{CO} was 1.2. The faint lines were included to indicate the positions of CO fundamental band transitions, which are the sharp transitions. The labeled transitions are the relevant CO transitions given in Table 6

As seen in Fig. 32, the presence of CO_2 in the exhaust stream introduces significant spectral interference for the R-branch CO transitions for J values higher than 14. To avoid CO_2 interferences, the R(11) CO transition at 2186.639 cm^{-1} was selected for the absorption measurements for the WSR field tests. The ECDL was coarse-tuned to 863.612 nm to achieve mid-IR generation at 4.573 μm. The 852-nm diode laser in the ECDL was replaced with an 862-nm diode, ID 2624. For resonance with transition R(11), the new diode operated with 32.3 mW and exhibited a mode-hop-free tuning range of 14 GHz. With the new diode, the mid-infrared power generated by DFM was only 89 nW. The new diode, ID

2624, exhibit a power reduction of 54 % with respect to diode ID JJ28. Considering this power drop the generation of mid-IR power was calculated to be 0.48 μW by means of (80). In this calculation the wavelength change was taken into account whereas all other focusing and absorption terms were assumed constant from previously implemented DFM processes. Considering as a reference the 0.897 μW generated for the gas cell experiments by using 58.0 mW from the ECDL 860.782 nm, the expected power drop due to the change of the 860-nm diode was 46%. The actual mid-IR power generated was only 9.9% of this value. This power drop of 90.1% was caused primarily by a small chip in the PPLN crystal output face that was discovered at the WSR facility during alignment of the CO sensor.

The field testing proceeded despite the low mid-IR power obtained. The ECDL was scanned at a rate of 1.32 Hz over a mode-hop-free tuning range of 14 GHz. Data was acquired by averaging 10 traces in software for a total acquisition time of 3.7 s. Analytical and reference signals were processed by the lock-in amplifiers set to a time constant of 3 ms with a roll-off of 24 dB/oct. The lock-in was referenced to the synchronous output of the optical chopper at 2.47 kHz, and the sensitivity was adjusted from 20 to 500 mV at each test condition to avoid overloading the dynamic reserve in the lock-in amplifier.

The conditions at which data was taken were dictated by the operational range of the well-stirred reactor. Due to thermal limitations the WSR can only be operated at very fuel rich ($1.4 \leq \Phi \leq 1.85$) or fuel lean conditions ($\Phi \leq 0.75$). Lean blowout of the reactor occurs at about $\Phi = 0.4$. In this series of experiments the reactor was fueled with ethylene and operated at equivalence ratios (Φ) of 0.4, 0.5, 0.65, 1.4, 1.6, 1.75, 1.8, and 1.85. At lean operating conditions, the CO concentration was expected to fall in the range 30 to 60 ppm, with expected CO_2 levels at 6 to 7%. At these conditions, spectral interference from CO_2 was strong enough to completely obscure the identification of CO transitions. At fuel-rich conditions, the CO content of the exhaust stream was expected to be on the order of 12 to 17 %. These CO concentrations are the same order of magnitude as the CO_2 concentration. Measurements could not be made at lower levels of CO because of the limitations of the WSR operating equivalence ratio.

Given the operational conditions of the WSR, and the high CO concentrations, the CO absorption transitions broaden to the extent of the sensor mid-IR tuning capabilities; therefore collected data does not

show un-attenuated regions. Also, because of thermal stresses in the reactor it was not possible to turn it off to take scans with no CO present. In this case, the collected data was normalized by the use of reference detector signal under scheme B as discussed in Chapter IV. For scheme B to be applicable, the slope of the traces must be similar. The slopes of analytical and reference traces were compared at the beginning and end of the test, when the reactor was off and hot air was flowing through the exhaust. It was found in this comparison that the slopes had a deviation less than 1%. Therefore the error induced by normalization scheme B was minimal.

Figure 33 presents some selected results from the field testing of the CO sensor in the WSR. Figure 33 shows the measured and calculated CO absorption line shape for the R(11) transition in the fundamental band at 2186.639 cm^{-1}. In the panels of Fig. 33, the only distinguishable species is CO. Due to the high CO concentration, almost 100% of the energy in the analytical beam is absorbed at the line center. While CO_2 was present in the exhaust stream, its concentration was the same order of magnitude as CO concentration, and the intensity for the CO_2 transitions in this spectral region is two orders of magnitude smaller than for the CO transitions. The CO_2 concentration had no effect on the fitting procedure and its inclusion did not impact the least squares criterion of the fit. Therefore, the concentrations for carbon dioxide obtained from the fitting procedure, including the values reported in Fig. 33, are meaningless for comparison with the extractive sampling. At these conditions, only attained for fuel rich operation of the reactor, the sensor was immune to CO_2 interferences.

The temperature measurements reported in Fig. 33 are the actual readings from the thermocouple. Those temperature measurements were not corrected for radiation because of the small size of the wires and the thermocouple was located at a different position than the absorption beam path. The temperature measured by the thermocouple was not meant to be checked against the best-fit temperature. Across the exhaust stream high temperature gradients exist and the thermocouple only provides the temperature at its location. The equivalent gas temperature of the absorption process is an average of the temperature profile along the beam path weighted by the absorption line strength evaluated at the temperature of each location along the path length. By not correcting the thermocouple reading, the actual gas temperature is expected to be higher due to radiation losses from the couple. Considering all of these, the thermocouple reading at

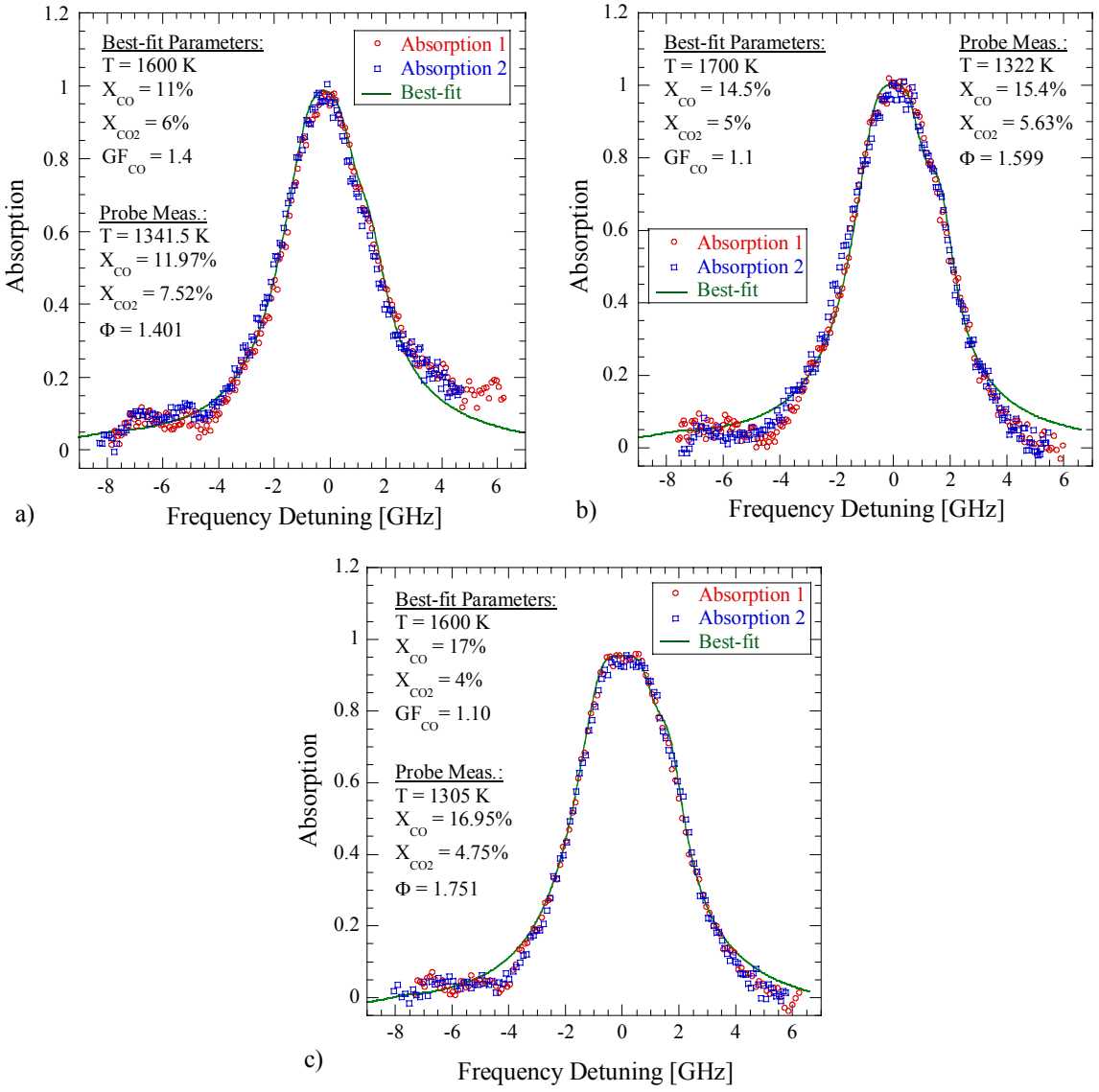

FIGURE 33 Comparison of measured and calculated CO absorption line shape for the R(11) transition in the fundamental band at 2186.639 cm^{-1}. Measurements were performed 3 mm over the exhaust of the WSR at WPAFB. The reactor was run fuel rich at equivalence ratios a) 1.4, b) 1.6, c) 1.75. The best fit parameters are shown for a path length of 0.05 m and atmospheric pressure (P = 101.33 kPa)

each test was used as an initial guess for the best-fit procedure. The resulting best-fit temperatures among the same equivalence ratio experiments were consistent to within 100 K.

In Fig. 33, the best-fit GF_{CO} factor is larger than 1 and accounts for line broadening by other molecules in the exhaust. A theoretical approach to the gamma factor can only be carried out if the

composition of the mixture is known, which is not the case. However, as the CO to CO_2 concentration ratio increases towards higher equivalence ratios it is expected and observed that the GF_{CO} tends to one indicating that the CO molecules have a more important effect on the collisional broadening of the CO transition.

From fuel rich experiments, the CO concentration was obtained through the best-fit to the experimental curves. All of the CO concentrations determined from several scans at different exhaust conditions agreed to within 15% with the results obtained from the extractive probe in conjunction with an NDIR analyzer. Similar discrepancies between probe and diode-laser measurements have been reported previously by Schoenung and Hanson [143], although Nguyen *et al.* [144] have reported that extractive sampling probes underestimate CO concentration by a factor of 10.

The sensitivity of the sensor was limited by the noise in the detection channel. For the field measurements on the WSR, the intrinsic noise rms standard deviation for the best-fit was calculated to be in the range of 0.036 to 0.039. This large value of the random noise is obscured by the strength of the absorption features in the panels of Fig. 33. Assuming a SNR of 1.0 at the detection limit, the rms noise of 0.039 corresponds to 21 ppm per meter for gas at 1000 K and atmospheric pressure. The decrease in sensitivity during the field measurements as compared to the gas cell experiments is due in part to noise and vibrations from the combustion equipment and noise induced by thermal deflections of the beam passing through the exhaust. However, the drop in the generated mid-IR power was the most significant factor in the reduction of the SNR, limiting the sensitivity of the sensor during the WSR measurements. Nonetheless, these measurements are still an excellent demonstration of the capabilities of this sensor in a real combustion environment.

5.3 Hydrogen/Air CO_2-Doped Flame Measurements

After the field testing of the sensor it was clear that the system had to be improved in two areas: damping of vibrations and operation in a region free of spectral interferences. Also, the field tests revealed that temperature measurements in combustion environments are complicated and uncertain. In

the laboratory environment, the goal was to operate the system in a high temperature CO_2 interference-free region.

To detect CO in high temperature environments using diode-laser probes many groups have used hydrocarbon/air diffusion flames (i.e. methane, natural gas, ethylene) [63, 66, 143, 145, 146]. These types of flames achieve CO concentration levels in the range 1 - 15 %, although lower CO production levels had been observed at the edge of the flames. In these flames, CO concentrations are adjusted by controlling the equivalence ratio. Recently, Wehe *et al.* [71] used a rich hydrogen/air diffusion flame to simulate the exhaust of a gas turbine. Their flame was cooled with nitrogen to achieve temperatures in the order of 1150 K; CO_2 was seeded into the burner and CO was formed by dissociation. In this flame Wehe *et al.* reported a measurement of 27 ppm CO in a folded 1.2 m path length using a quantum-cascade laser.

A hydrogen/air flame doped with CO_2 and N_2 allows for adjustment of the CO concentrations by means of CO_2 flow and flame temperature can be adjusted to certain degree by adjusting the N_2 flow. This flame was ideal for testing for the CO sensor since in addition to control of the CO production it offered a high temperature environment with an elevated concentration of CO_2. A Hencken burner was used to produce a flat, uniform, steady, and nearly adiabatic flame [147]. A series of experiments for CO measurements were carried out with the diode-laser sensor in different flames. The flames tested had equivalence ratios of Φ = 0.81, 1.15, 1.34, 1.54 with CO_2 flows within the 0.5 – 4.9 l/min range. For these flames the diode-laser sensor measurements showed flame temperatures in the range of 1600 to 2500 K and CO concentrations in the range of 2100 ppm to 1.7 %. Representative results of these experiments are presented in this section.

To avoid spectral interference with the CO molecule a detailed survey of the P-branch transitions in the fundamental band was carried. As can be seen in Fig. 28, the lower limit for CO P-branch transitions is 4.66 μm. For mid-IR generation by DFM in a PPLN crystal, accessible CO transitions are limited by the 5.2 μm transparency limit of the PPLN crystal. At 1000 K, the strengths of the CO_2 transitions in the 4.66 to 5.2 μm spectral region are about three orders of magnitude lower than those for CO. Similarly, weak H_2O transitions are observed in the same range. In selecting a CO target transition

for measurements in the flame the transition line strength and neighboring spectral interferences were taken into account. Two candidate CO transitions in the P-branch of the fundamental band were selected. Figure 34 shows (a) the P(18) transition at 2068.8469 cm^{-1} and (b) the P(19) transition at 2064.3969 cm^{-1}. These theoretical simulations were produced with the "Direct_Absorption" code for a mixture of 2000 ppm CO and 10% CO_2 at 1500 K, atmospheric pressure, a path length of 0.05 m and assuming only Doppler broadening. Lines P(18) and P(19) are attractive because within the sensor tuning capabilities CO hot-band transitions can be resolved allowing for two-line thermometry. In panels a) and b) of Fig. 34 the CO hot-band transitions P(12) at 2068.8025 cm^{-1} and P(13) at 2064.5839 cm^{-1} occur at -1.5, and +5.5 GHz frequency detuning respectively. Other small perturbations are seen on the baselines of Fig. 34 due to the presence of weak CO_2 absorption transitions.

To check for H_2O interferences for these two lines HITRAN database was directly consulted. Table 13 gives the closest H_2O absorption transitions to the CO P(18) and P(19) transitions. H_2O

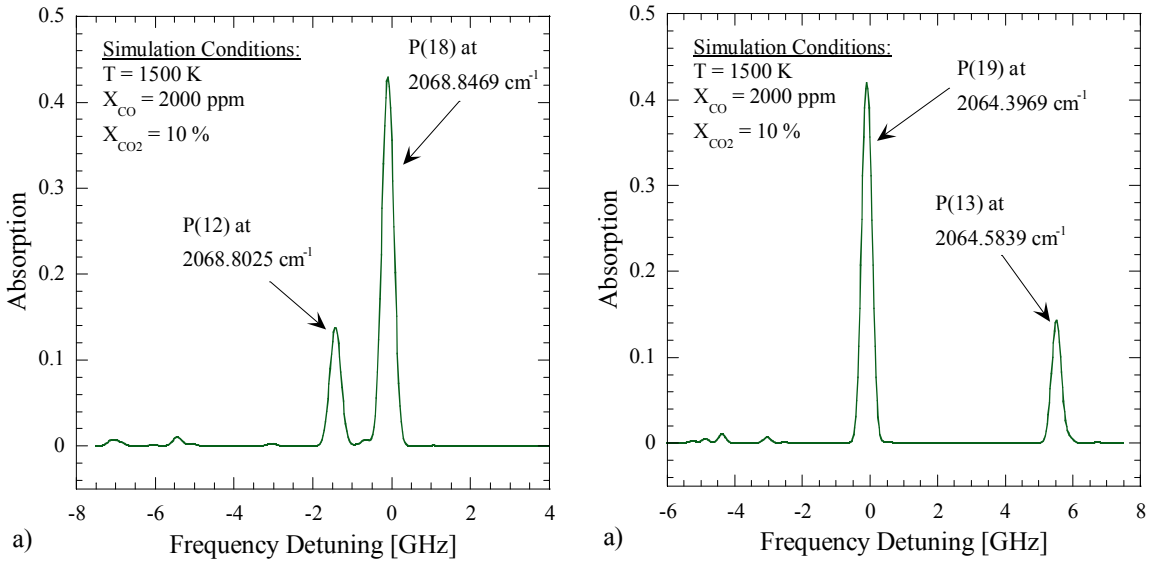

FIGURE 34 Selected CO fundamental band transitions for CO concentration measurements in the H_2/air flame. In panel a) transition P(18) at 2068.8469 cm^{-1} is seen at 0 GHz freq. detuning, in panel b) at 0 GHz freq. detuning is shown transition P(19) at 2064.3969 cm^{-1}. These theoretical simulations were produced for a mixture of 2000 ppm CO and 10% CO_2 at 1500 K, atmospheric pressure, a path length of 0.05 m and assuming only Doppler broadening. The transitions P(12) and P(13) at about -1.5, 5.5 GHz frequency detuning for panels a) and b) respectively corresponds to CO hot-band transitions. Other small perturbations on the baselines are CO_2 absorption transitions

	H_2O transition at [cm^{-1}]	$S_\tau(1000)$ [cm^{-1}/molecule cm^{-2}]	Freq. Det. [GHz]*
CO P(18)			
	2067.877	$4.504x10^{-20}$	-29.07
2068.8469	-	$1.66x10^{-19}$	0
	2068.896	$2.086x10^{-23}$	1.47
	2069.345	$5.976x10^{-24}$	14.9
CO P(19)			
	2063.113	$9.918x10^{-25}$	-38.5
2064.3969	-	$1.583x10^{-19}$	0
	2064.853	$2.472x10^{-21}$	13.67

* Frequency detuning with respect to the nearest CO transition

TABLE 13 Neighboring H_2O absorption transitions for selected CO fundamental band transitions P(18) and P(19)

absorption transitions are not of concern because their strength is at most one order of magnitude lower than CO absorption transitions at 1000 K and they are located well beyond the tuning range of the sensor. Thus, absorption due to H_2O molecules will be weak to modify P(19) or P(18) absorption features and will not affect the sensor measurements, although the H_2O transition at 2068.896 cm^{-1} might interfere very slightly with the P(18) line. Figure 35 shows a scan taken from the hydrogen/air/CO_2 flame in which the sensor was set to detect the transition P(18) of the CO fundamental band. In Fig. 35 the CO transitions P(18) is seen at 0 GHz detuning, whereas the hot-band transition P(12) is observed overlapping with P(18) at -1.5 GHz detuning. The H_2O transition at 2068.896 cm^{-1} was expected to appear at about 1.47 GHz detuning, however the broadening of the CO P(18) line covers this line and makes it difficult to distinguish. The absorption feature seen at about 3.5 GHz was clear, strong and it was present through a set of experiments with the flames. This transition was not listed in the HITRAN [44] database among the 38 species listed. With this unknown interference observed in Fig. 35, it was decided to coarse tune the ECDL to produce mid-IR radiation in resonance with P(19) transition.

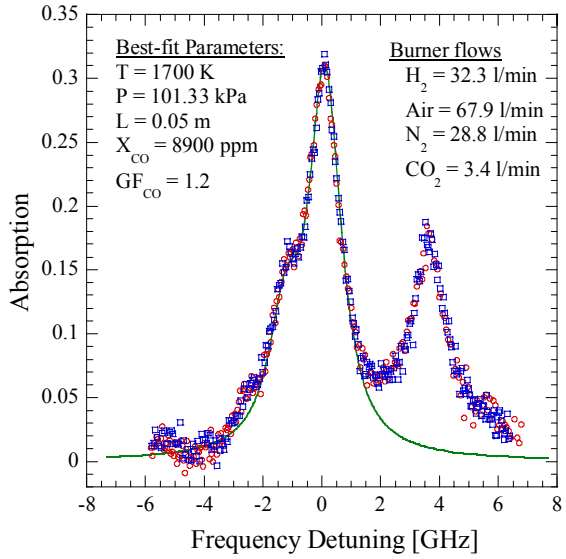

FIGURE 35 Comparison of the measured and calculated mid-IR absorption spectrum in a hydrogen/air CO_2-doped flame. The Absorption features observed corresponds to the CO P(18) (at 0 GHz) transition of the fundamental band at 2068.8469 cm^{-1}, and the P(12) (at -1.5 GHz) hot-band transition at 2068.8025 cm^{-1}. The absorption feature at 3.5 GHz is not listed in among the 38 species of the HITRAN [44] database and represents an undesired spectral interference to transition P(18)

The ECDL was coarse tuned to 872.826 nm so that the generated mid-IR radiation was in resonance with the P(19) transition in the fundamental band of CO at 2064.396 cm^{-1} . Tuning the mid-IR radiation to the wavelength of this particular transition was advantageous because CO_2 absorption was not observed in this region. Also, the P(13) hot-band transition at 2064.583 cm^{-1} emerges at high temperatures within the scanning range of the sensor, offering independent verification of the wavelength and two-line thermometry.

To address the P-branch transitions some modifications to the sensor layout were performed. The PPLN crystal was replaced with another PPLN crystal featuring a track with a 22.1 μm quasi-phase-match period to achieve DFM generation in the 4.8 μm region when operating at 189.7ºC. The ECDL was used with the 862-nm diode, ID 2624. This diode was acquired because it was capable of lasing at higher wavelength. The specified tuning range of the ECDL using this diode was from 848 to 864 nm with maximum output power of 55 mW. To obtain laser radiation at 872.826 nm the ECDL grating was

severely tilted and the cavity was in resonance with a higher order reflection from the grating. This tilting had two important effects in the output beam: the power decreased to 14 mW and the shape of beam was distorted. The ECDL tuning capabilities were degraded so that scanning of the output wavelength was performed very slowly using a sawtooth function at a frequency of 260 mHz. At these conditions the ECDL operated single mode within a mode-hop-free tuning range of about 9 GHz.

By modifying the system to access the P(19) transition, the DFM process was affected by changes in the temperature of the crystal and the wavelengths of the input beams. The change in wavelength of the incident beams induces a change in the indices of refraction for all three interacting beams. The power drop in the ECDL beam directly affects the efficiency of the conversion process. Using (80) and (81), the expected power of the mid-IR beam at the wavelength of the P(19) transition was calculated to be 233 nW; this computation assumed that only the indices of refraction and power of the 860-mn beam changed from the reference conditions of gas cell experiments of the R(23) transition. For the R(23) transition, approximately 897 nW of mid-IR radiation were produced. Actually, the power of the 4.8 μm radiation was measured to be 134 nW, approximately 15% of the power obtained for the R(23) transition. The difference between the calculated mid-IR power and the 134 nW produced can be attributed to distortion of the beam shape which modifies the focusing characteristics of the 873-nm ECDL beam.

Before proceeding with the flame experiments a series of absorption measurements of P(19) transition were performed in the room temperature gas cell. For these experiments the gas cell conditions were similar to those previously described for the R(23) transition experiments. The average best-fit CO concentration of the data was 1005.4 ppm with an uncertainty of ±18 ppm which agrees well with the certified gas mixture concentration. The average best-fit gamma factor (GF_{CO}) was 0.962 for the series of experiments. The HWHM for the N_2-broadening coefficient ($\gamma^o_{CO\text{-}N2}$) was computed to be 0.0493 cm^{-1}/atm for the P(19) line. This value is 8.5% and 6.9% lower than the HWHM coefficients reported in literature by Varghese and Hanson [64] and Nakazawa and Tanaka [137] respectively. In this series of experiments an unwanted etalon effect was observed in the normalized absorption trace. This etalon

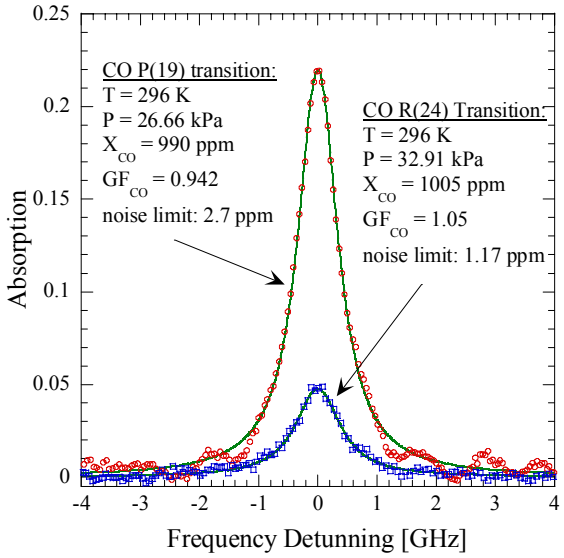

FIGURE 36 Comparison of the measured and calculated CO absorption transitions R(24) and P(19) of the fundamental band at 2227.6386 cm^{-1} and 2064.3969 cm^{-1} respectively. Data was taken in the 0.32 m long gas cell at the indicated conditions. These two sets of data are presented for comparison of the lines shape and noise levels

contributed significantly to the rms standard deviation of the baseline. The rms noise for this testing was in the range from 0.0031 to 0.0073, corresponding to detection limits of 1.9 to 4.5 ppm per meter at 1000 K and atmospheric pressure.

Figure 36 compares the results from testing in the room temperature gas cell for the R(24) and P(19) transitions of the fundamental band of CO. Representative data from R(24) transition experiments at 32.91 kPa is compared with a gas cell data scan of transition P(19) at 26.66 kPa in Fig. 36. The etalon effect is clearly visible in the P(19) trace of Fig. 36. In addition to the etalon effect, the noise level of trace P(19) was increased because of the lower mid-IR power. The estimated detection limit of the sensor is based in the SNR = 1 condition and therefore has increased as expected.

With this low mid-IR power, CO concentration measurements were performed on the H_2/air CO_2-doped flame. For these experiments data was acquired fro a time period of 13.4 s. Typically, seven traces were consecutively acquired and averaged in software. The increase in total acquisition time is due to the slow scanning rate of the ECDL. Binning of ten neighboring channels was performed to reduce read noise. Due to the observation of two CO transitions and the shorter scanning range, the spectra acquired

using the analytical detector do not show un-attenuated regions. Processing of the data was carried using scheme C, as described in Chapter IV. This scheme was implemented because the flame can be turned on/off easily allowing for no-CO scans to be acquired within seconds of having acquired CO absorption data.

Figures 37 and 38 show the measured and calculated fractional absorption spectra for the P(19) fundamental band and P(13) hot-band CO transitions at 0 and 5.5 GHz frequency detuning, respectively. Measurements were performed at 25 mm and 5 mm from the top of the burner. The absorption path length through the flame was estimated to be 0.05 m. The flames that were probed were fuel rich with an equivalence ratio (Φ) of 1.15. Flows with flow rates of 23.0 l/min of hydrogen (H_2) and 28.0 l/min of nitrogen (N_2) were pre-mixed and input to the burner as the fuel stream. The air flow of 65.0 l/min was pre-mixed with the CO_2 flow as the oxidizer stream. In this series of experiments the CO_2 flow rates were in the range of 2.0 to 4.9 l/min. These flows were controlled to within 1% uncertainty by MKS mass flow controllers.

Figure 37 shows the comparison of the experimental spectrum with the best-fit theoretical spectrum at 5 mm from the burner surface. As shown in Fig. 37 the theoretical spectral line shape, intensity and line width of both absorption features are in excellent agreement with the experimental data. Both transitions were resolved. The availability of two lines allowed us to reduce the uncertainty of the fitting procedure. Although the CO concentration measurements were not corroborated by any other means such as extractive sampling, the data was very repeatable. The sensor uncertainty was estimated on the order of 10% based on repeatability of the peak absorption and intrinsic noise read in the data from several tests on different days. For these flame experiments the GF_{CO} parameter had an average value of 1.42 through the series of tests. Also observed in Fig. 37 is the ability to control the amount of CO in the flame by controlling the inlet flow of CO_2. The rms noise standard deviation to the best-fit for the data taken at 5 mm and shown in Fig. 37 was measured to be 0.004. Again, assuming a SNR of 1.0 the equivalent sensor detection limit was computed to be 2.5 ppm per meter of gas at 1000 K and atmospheric pressure.

Measurements were also performed at 25 mm from the top of the burner. Figure 38 a) and b) shows the recorded data at 25 mm for comparison with panels a) and b) of Fig. 37 respectively. It can be seen that the CO concentration dropped about 40% from the 5 mm location to the 25 mm location. This CO concentration decreased probably occurred the flame was operated without a shroud flow and at 25 mm the diffusion flame at the edges is oxidizing the CO. However, numerical simulations of the flame are needed to fully understand this observed behavior of the flame. Despite of the drop of the CO concentration, the rms noise measured maintained the same 0.004 value. Again, improvement of the sensor detection limit can be achieved by increasing the generated mid-IR power since this directly improves the signal-to-noise ratio.

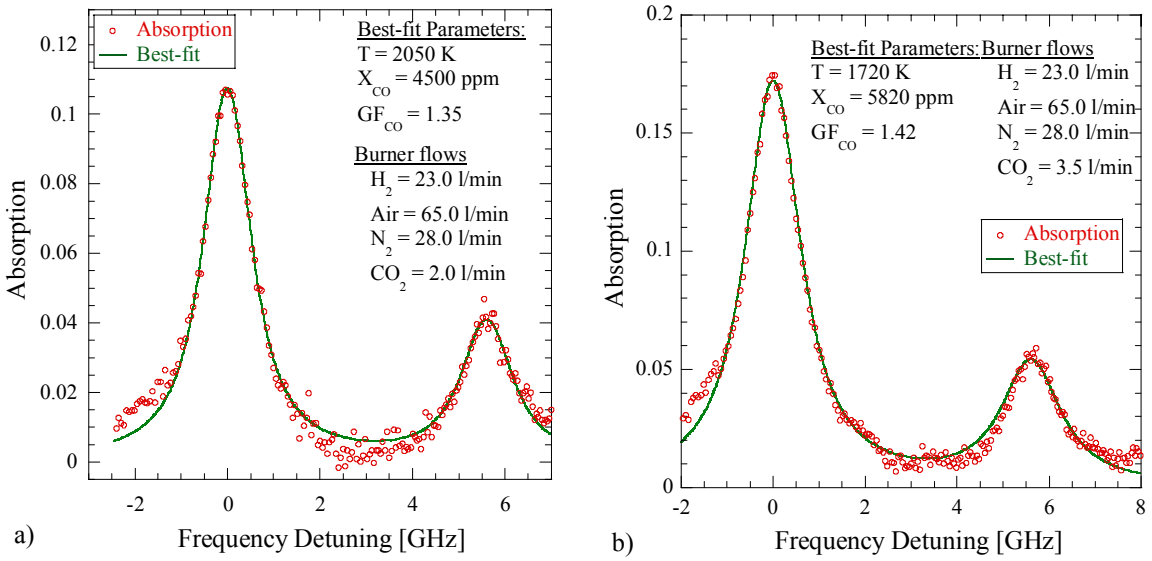

FIGURE 37 Comparison of the measured and calculated CO absorption line shapes for the P(19) (at 0 GHz) fundamental band transition at 2064.3969 cm^{-1} and the P(13) (at 5.5 GHz) hot-band transition at 2064.583 cm^{-1}. Measurements were performed at 5 mm above the surface of the Hencken burner, with a path length of 0.05 m through a fuel rich (Φ = 1.15) H_2/air CO_2-doped flame at atmospheric pressure. Rates of fuel, air, coolant, and dopant flows are shown in panels through which flow of dopant CO_2 was adjusted to a) 2.0 l/min, b) 3.5 l/min, and c) 4.9 l/min to change the CO content of the flame

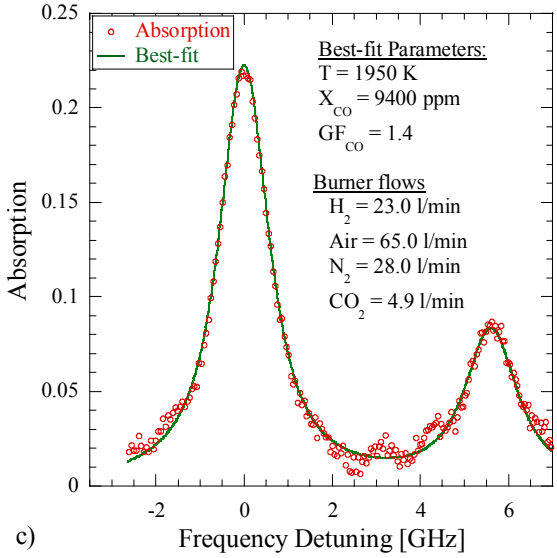

FIGURE 37 Continued

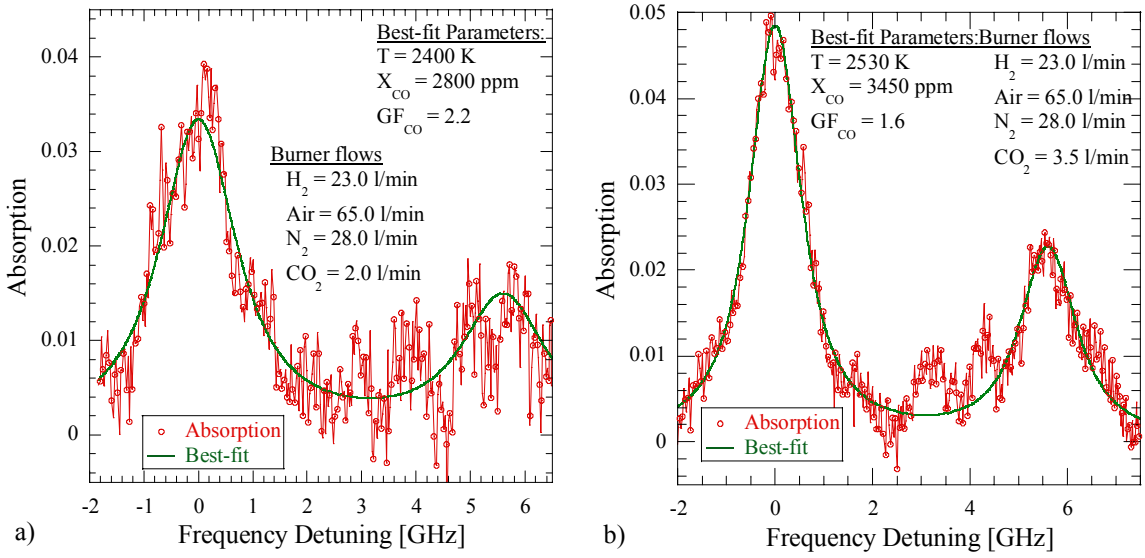

FIGURE 38 Comparison of the measured and calculated CO absorption line shapes for the P(19) (at 0 GHz) fundamental band transition at 2064.3969 cm^{-1} and the P(13) (at 5.5 GHz) hot-band transition at 2064.583 cm^{-1}. Measurements were performed at 25 mm above the surface of the Hencken burner, with a path length of 0.05 m through a fuel rich (Φ = 1.15) H_2/air CO_2-doped flame at atmospheric pressure. Panels compare directly to panels a) and b) in Fig. 37

CHAPTER VI

SUMMARY AND RECOMMENDATIONS

6.1 Summary

A sensor system for mid-infrared single-pass direct absorption measurements of CO has been demonstrated. The system produces mid-IR radiation in the 4.4 – 4.8 μm spectral region by difference frequency mixing (DFM) in a periodically poled lithium niobate (PPLN) crystal. This work presents absorption measurements for several CO transitions in the fundamental band R(24), R(23), R(11), and P(19) at 2227.6386, 2224.7127, 2186.639, and 2064.3969 cm^{-1} respectively. The system was tested in different experiments that demonstrate its operation and ability to detect CO in $CO/N_2/CO_2$ mixtures, under combustor exhaust conditions, and in flames featuring high temperature environment with high CO_2 concentrations.

Direct absorption single-pass measurements of carbon monoxide concentration were performed in a room temperature gas cell to demonstrate the operation of the diode-laser-based sensor and validate the spectral simulation "Direct_Absorption" code. Gas cell measurements were also performed for each transition tested through out the project. These measurements were useful to verify the ECDL wavelength and the HITRAN spectroscopic parameters of each transition. Gas cell conditions allowed us to observe isolated CO transitions and to distinguish them from neighboring CO_2 absorption lines. In particular the isolated CO fundamental band transitions R(24) and R(23) were studied. $CO/N_2/CO_2$ mixtures were also probed. When CO and CO_2 transitions occurred within the scanning range of the sensor and were resolved simultaneously the mid-IR wavelength was further verified.

A "gamma factor" (GF_{CO}) was introduced in the "Direct_Absorption" code to account for collisional broadening due to other molecules present in the gas mixture but not included in the HITRAN database. The effect of this factor in the fitting process was comprehensively studied for the R(23) transition of the CO fundamental band. It was demonstrated that the GF_{CO} factor was useful for calculating the broadening of CO transitions caused by N_2 and CO_2 collisions. Based on the collected

data, the best-fit GF_{CO} value was obtained and CO collisional broadening coefficients for buffer gases were calculated. From gas cell absorption measurements of transition R(24), the half-width half-maximum (HWHM) coefficient for N_2-broadening ($\gamma^o_{CO\text{-}N2}$) was calculated to be 0.0465 cm^{-1}/atm. This value falls within 2% of values reported in the literature. For the CO R(23) transition of the fundamental band, the HWHM coefficient for N_2-broadening was computed to be $\gamma^o_{CO\text{-}N2}$ = 0.0502 cm^{-1}/atm. From gas cell absorption measurements in $CO/N_2/CO_2$ mixtures, the HWHM coefficient for CO_2-broadening for CO transition R(23) was computed to be $\gamma^o_{CO\text{-}CO2}$ = 0.0461 cm^{-1}/atm. These calculated coefficients for transition R(23) are within 6.5% and 4.3% of published values, respectively.

For the CO absorption measurements in the room temperature gas cell, the uncertainty of the sensor concentration measurements was estimated to be on the order of 2%. The current sensitivity of the system in a controlled laboratory environment is computed to be 1.17 ppm for a 1-m path length through 1000 K combustion gas at atmospheric pressure. This limit can be lowered significantly through the use of wavelength modulation spectroscopy (WMS) or frequency modulation spectroscopy (FMS) [39] techniques. Minimum detectable normalized absorption levels of 10^{-5} are usually achieved with WMS, whereas FMS technique at megahertz frequencies can be used to achieve sensitivities on the order of 10^{-8}.

After successful tests of the sensor in the laboratory environment a series of field tests were performed. Field testing of the CO sensor was carried out in real combustion environments. CO measurements were performed on the exhaust of a 90 kW gas turbine at Honeywell Engines and Systems and a well-stirred reactor (WSR) at Wright-Patterson Air Force Base. At these facilities the sensor was subjected to high temperatures, mechanical vibrations, un-damped mounting, and remote operation. The sensor performed well in these realistic combustion environments. In these conditions absorption spectra were acquired successfully. Improvements in mounting and vibration isolation proven helpful in reducing the noise in the operation of the sensor.

The most significant concern in the design and operation of the sensor were spectral interferences from other molecules present in the exhaust stream. For testing in the gas turbine engine, the CO R(20) fundamental band transition at 2215.7044 cm^{-1} was interrogated. This transition was surrounded by CO_2

spectral interferences that prevented the recording of a flat baseline. These CO_2 interferences and mechanical vibrations limited the results obtained from the testing. The noise detection limit for the sensor under these conditions was estimated at 1.93 ppm per meter of gas at 1000 K and atmospheric pressure. CO concentration measurements with the diode-laser-based sensor were compared against standard extractive sampling from the gas turbine exhaust. The probe location was 90 cm upstream from the mid-IR beam. Diode-laser-based sensor measurements were lower by a factor of 3. Probe and diode-laser-based sensor CO measurements did not agree despite the good agreement observed in the best-fit to the data.

The system was also successfully tested by performing CO measurements in the exhaust of the well-stirred reactor (WSR) at Wright-Patterson Air Force Base (WPAFB). For testing at the WSR the sensor was tuned to interrogate the CO R(11) transition at 2186.639 cm^{-1}. To generate mid-IR radiation in resonance with this transition, the diode for the ECDL was replaced by a diode tuned to 863.612 nm. This diode substitution resulted in an ECDL power reduction of 54%. An unfortunate chip in the output face of the PPLN crystal limited the generated mid-IR radiation to 89 nW. With this low mid-IR power the SNR was decreased and the sensitivity of the sensor was determined to be 21 ppm per meter of path length in gas at 1000 K and atmospheric pressure.

Despite the large noise observed in the WSR tests, the high CO concentrations in the exhaust allowed us to perform accurate measurements. Due to thermal limitations, the WSR ran fuel rich at equivalence ratios from 1.4 to 1.85 and under these conditions CO concentrations in the exhaust were in the range 12 to 17%. At these high CO levels, single-pass absorption over 0.05 m path length reached levels of 100% at the line center. The main consequence of high CO concentration in the exhaust is that the CO and CO_2 concentrations were of the same order of magnitude in a region were the strength of CO absorption transitions was two orders of magnitude larger. Thus, the effect of CO_2 spectral interferences was minimal and the best-fit procedure was insensitive to the CO_2 concentration.

Measurements of CO concentrations in the WSR exhaust agreed to within 15% with extractive sampling measurements. The WSR absorption measurements represented an excellent demonstration of the capabilities of the sensor to operate in the severity of a real combustor environment and constituted a

milestone in the development of the diode-laser-based CO sensor towards combustion control applications.

Finally, a set of CO absorption measurements were performed on near-adiabatic hydrogen/air/N_2/CO_2 flames. Spectral interferences were investigated in detail in the CO_2-doped flame tests and CO spectral lines with minimal CO_2 and H_2O absorption interferences were identified. In this type of flame, CO is produced by dissociation of CO_2 and thus can be controlled by controlling the CO_2 flow and flame temperature by the addition of nitrogen into the flame. A Hencken burner was used to produce flat, uniform, steady, and near adiabatic, fuel rich flames with equivalence ratios from 0.81 to 1.54. The resulting CO concentrations measured were in the range of 2100 ppm to 1.7 %.

The CO P(19) transition in fundamental band at 2064.3969 cm^{-1} and P(13) transition in the first hot-band at 2064.5839 cm^{-1} were probed offering the option of two-line thermometry, which also reduces the uncertainty in the best-fit process. To access these transitions the ECDL was coarse tuned to 872.826 nm by tilting the grating in the cavity. The severe grating adjustment needed caused the power of the ECDL to drop to 14.4 mW and the beam shape was distorted. Under these conditions, the generated mid-IR power was of 134 nW, while the ECDL mode-hop-free tuning range was reduced to 9 GHz at a rate of 260 mHz.

Despite the lack of extractive sampling measurements to corroborate the diode-laser CO absorption measurements, the experimental and theoretical line shapes, intensities, and width are in excellent agreement for both transitions within the scanning range. The sensor uncertainty was estimated to be on the order of 10% based on the repeatability of the peak absorption values and the intrinsic noise of the data. The noise equivalent detection limit for the sensor for the hydrogen/air CO_2-doped flame experiments was determined to be 2.5 ppm-m at 1000 K gas at atmospheric pressure. Numerical simulations of the Hencken burner flames are needed for comparison with the diode-laser-sensor absorption measurements.

The simplicity, generality, and relatively low cost of the DFM-based sensor described make it an attractive system for carbon monoxide detection in the mid-IR region. The sensor was successfully tested in real combustor environments that address some of the issues of the sensor design. Spectral

interference-free operation was achieved in the 4.8 μm region and was tested in a near-adiabatic hydrogen/air/N_2/CO_2 flame. The overall success of the testing demonstrated the feasibility of the diode-laser-based CO sensor as a spectroscopic tool and for measurements in real combustors.

6.2 Recommendations for Future Work

To continue the development of the diode-laser-based CO sensor, system modifications need to improve the sensitivity of the concentration measurements and to acquire data at faster rates. To improve the sensitivity of the sensor both an increase in generated mid-IR power and better noise discrimination are required. For increased mode-hop-free tuning range and faster scanning of the output frequency a different scanning technique such as electro-optic tuning or the use of a DFB laser are required.

Tests in the hydrogen/air flame had shown that transitions in the P-branch of the fundamental band of CO are much less affected by CO_2 interferences than R-branch transitions. Having identified meaningful transitions to test, coarse tuning of the laser is not as important as single-mode scanning of the output frequency over a broader range that ensures full resolution of the absorption lines. Distributed Feedback (DFB) diode lasers are ideal for this purpose. As compared to ECDL systems, DFB diode lasers operate single-mode over a much broader scanning range and can be scanned at rates of tens of kHz by current modulation. DFB systems are commercially available at a few selected wavelengths with relative narrow linewidth (5 MHz) and high output powers. Toptica Photonics offers an 860-nm DFB diode laser with 70 mW output power. The output frequency of DFB lasers can be adjusted over a small range by temperature fine tuning at a rate of 21 GHz/K.

To access the P-branch of the fundamental band of CO by DFM, an 860-nm DFB system has to be mixed with a 1047-nm laser source. Nd:YLF lasers operating at 1047 nm are commercially available from Crystalaser. These two laser sources have been substituted into the CO sensor system described in this thesis, and the sensor system was used for a series of CO measurements in August 2004 at WPAFB. The 860-nm DFB laser system has replaced the 872-nm ECDL, whereas the 1064-nm beam has been substituted by a 1047-nm Nd:YLF CrystaLaser system that delivered 140 mW. The wavelength of the 1047-nm beam was measured to be 1047.611 nm. The DFB central wavelength was set at 860.328 nm by

adjusting the temperature to 40.7 ºC. These new sources produced 24 nW of mid-IR radiation at 4.813 μm. This power was generated using 94 mW of the 1047-nm system and 50 mW from the 860-nm DFB. Although the generated mid-IR power was low, the test was preliminary and not much effort was spent on alignment. However, the sensor was applied for direct absorption measurements of CO concentrations in ethylene/air flame from a Hencken burner at Wright-Patterson AFB. For this testing the DFB output was current modulated at a rate of 1 kHz over a 72-GHz mode-hop-free tuning range. Figure 39 shows a comparison of a measured and theoretical spectrum from these tests. The target CO line was the P(16) transition in the fundamental band at 2077.6497 cm^{-1} observed at o GHz frequency detuning. Also, a water vapor transition is observed at about -15 GHz.

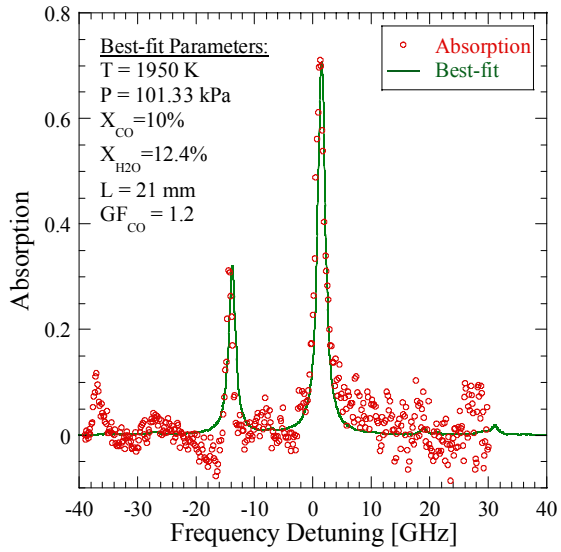

FIGURE 39 Comparison of measured and calculated CO absorption line shapes for the P(16) fundamental band transition at 2077.6497 cm^{-1} (at 0 GHz). Preliminary measurements were performed with the diode-laser-based system described but using a DFB 860-nm laser in a DFM process with a 1047-nm Nd:YLF. CO was detected in a fuel-rich (Φ = 1.4) ethylene/air flame produced in a Hencken burner at WPAFB

With the proposed system, implementation of wavelength modulation spectroscopy (WMS) or frequency modulation spectroscopy (FMS) is straightforward since current modulation of the DFB allows

for high frequency modulation. With these improvements to the system, it is feasible to apply it for either spectroscopic studies or to sensitive detection of carbon monoxide in unsteady environments.

6.2.1 Potential application for detection of NH_3

DFM-based CO absorption sensor strategy described and tested in this study is simple, general, relatively low cost, and potentially applicable to numerous other interesting molecules in the mid-IR spectral region. Previously, the sensor was tuned to interrogate CO transitions and effort was devoted to finding isolated transitions that do not suffer from spectral interferences. These interferences are not desirable since they distort or obscure the absorption line shape and distort the baseline of the trace. However, if the spectral simulation code is sufficiently detailed and accurate, both transitions can be fit and not only one but several molecular concentrations can be determined, simultaneously.

For combustion systems, other interesting molecules with absorption in the mid-IR region are carbon dioxide and water vapor. In fact the diode-laser-based sensor discussed in the thesis was used to detect CO_2 by resolving the P(51) the transition at 2224.519 cm^{-1} as shown in Fig. 21. The "Direct_Absorption" code has the capability of multi-species calculation due to the multi-parameter fitting technique that is used.

Another interesting molecule is ammonia. Ammonia is not a combustion product but it is injected into the combustion process for conversion of nitric oxide (NO) to molecular nitrogen (N_2) through a process known as selective non-catalytic removal (SNCR). At Texas A&M University the Coal Combustor facility provides a fully instrumented 30 kW (100,000 BTU/hr) boiler burner for sensor testing experiments. This facility can be fired with gaseous fuels, coal, biomass, and coal:biomass blends [148 – 150]. The production of NOx from coal:biomass combustion has been investigated extensively in previous experiments with this system. It is hypothesized that the ammonia present in the biomass can act as a DeNOx agent to reduce NOx fromed from burning of the coal, thus biomass serves as a effective reburn fuel. It is of interest to measure the ammonia and NO emissions at the exhaust of the coal combustor in reburn experiments.

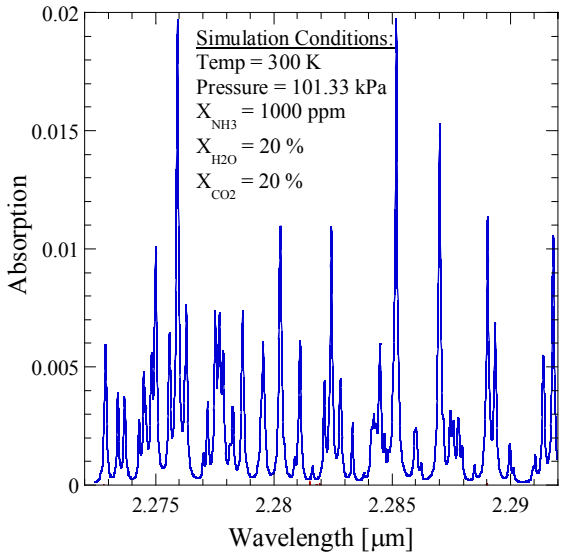

FIGURE 40 Ammonia spectrum in range 2.27 to 2.29 μm. Simulation of this spectrum was done by using the "Direct_Absorption" code, conditions were set for a $NH_3/H_2O/CO_2$ mixture in the 0.32 m gas cell at room temperature and 101.33 kPa

The principle of operation of the diode-laser-based sensor can be applied for detection of ammonia, but appropriate transitions must be identified first. According to HITRAN database [44], strong ammonia absorption transitions are located at about 1.5, 2.0 and 2.3 μm regions. Diode-laser absorption measurements of ammonia have been performed in the 1.5 and 1.98 μm regions [151, 152] using an ECDL system. Recently Kosterev *et al.* [153] used a quantum cascade diode laser to detected ammonia in the 10 μm region. However in these regions spectral interference from CO_2 and H_20 is present almost everywhere. With the capabilities of the "Direct_Absorption" code, the ammonia spectrum in the region from 2.27 to 2.29 μm was simulated. Figure 40 shows the calculated absorption spectrum of ammonia in a 0.32 m gas cell at 300 K and 101.33 kPa filled with a mixture of NH_3, H_2O, and CO_2. It appears that this spectral region is a good candidate for ammonia detection since it is free from spectral interferences. The maximum ammonia absorption levels are of 2%. The ammonia transitions overlap and are approximately about 20 GHz wide.

To access the spectral region in Fig. 40 with a diode-laser-based sensor system, at least two options are available for DFM generation of mid-IR radiation. Using the 1064-nm CrystaLaser system and a diode laser at 725-nm, or using a diode-pumped 532-nm intracavity frequency doubled Nd:YAG laser and a 695-nm diode laser are two possibilities. These diodes are commercially available but their powers are in the order of 20 mW. It may also be possible to use DFB diode lasers for the latter DFM combination. Thus, modifications to the system are minimal but much more design of the system is involved since the target spectral region has been reestablished. Nevertheless, the experience acquired in developing the CO diode-laser-based sensor described is of great importance for future development of either a new generation of CO sensors or the development of new sensors based on the DFM process.

REFERENCES

1. Office of Research and Development: *Air Quality Criteria for Carbon Monoxide*, EPA 600/P-99/001F (United States Environmental Protection Agency, Washington DC, June 2000)
2. Air Resources Board: *California exhaust emission standards and test procedures for 2001 and subsequent model passenger cars, light-duty trucks, and medium-duty vehicles*, (California Environmental Protection Agency, August 1999)
3. D. E. Burch, F. J. Gates, J. D. Pembrook: *Ambient carbon monoxide monitor*, report no. EPA-600/2-76-210 (Environmental Protection Agency, Environmental Sciences Research Laboratory, Research Triangle Park, NC, 1976)
4. D. D. Parrish, J. S. Holloway, F. C. Fehsenfeld: Environ. Sci. Technol. **28**, 1615 (1994)
5. J. M. Hoell, G. L. Gregory, D. S. McDougal, G. W. Sachse, G. F. Hill, E. P. Condon, R. A. Rasmussen: J. Geophys. Res. Atmos. **92**, 2009 (1987)
6. W. Seiler, H. Giehl, P. Roggendorf: Atmos. Technol. **12**, 40 (1980)
7. P. C. Novelli, V. S. Connors, H. G. Reichle, B. E. Anderson, C. A. M. Brenninkmeijer, E. G. Brunke, B. G. Doddridge, V. W. H. J. Kirchhoff, K. S. Lam, K. A. Masarie, T. Matsuo, D. D. Parrish, H. E. Scheel, L. P. Steele: J. Geophys. Res. Atmos. **103**, 19285 (1998)
8. L. Wallace, J. Thomas, D. Mage, W. Ott: Atmos. Environ. **22**, 2183 (1988)
9. W. Ott, P. Switzer, N. Willits: J. Air Waste Manage. Assoc. **44**, 1010 (1994)
10. S. J. McBridge, A. R. Ferro, W. R. Ott, P. Switzer, L. M. Hildemann: J. Expo. Anal. Environ. Epidemiol. **9**, 602 (1999)
11. C. Gerbig, D. Kley, A Volz-Thomas, J. Kent, K. Dewey, D. S. McKenna: J. Geophys. Res. Atmos. **101**, 29299 (1996)
12. C. Gerbig, S. Schmitgen, D. Kley, A. Volz-Thomas, K. Dewey, D. Haaks: J. Geophys. Res. Atmos. **104**, 1699 (1999)

13. L. W. Chaney, D. G. Rickel, G. M. Russwurm, W. A. McClenny: Appl. Opt. **18**, 3004 (1979)

14. G. W. Sachse, G. F. Hill, L. O. Wade, M. G. Perry: J. Geophys. Res. Atmos. **92**, 2071 (1987)

15. A. Fried, B. Henry, D. D. Parrish, J. R. Carpenter, M. P. Buhr: Atmos. Environ. **25A**, 2277 (1991)

16. J. Roths, T. Zenker, U. Parchatka, F. G. Wienhold, G. W. Harris: Appl. Opt. **35**, 7075 (1996)

17. K. C. Clemitshaw: Crit. Rev. Environ. Sci. Technol. **34**, 1 (2004)

18. N. Docquier, S. Candel: Prog. Energy Combust. Sci. **28**, 107 (2002)

19. L. D. Birkefeld, A. M. Azad, S. A. Akbar: J. Am. Ceram. Soc. **75**, 2964 (1992)

20. H. Torvela, J. Huusko, V. Lantto: Sens. Actuators B Chem. **4**, 479 (1991)

21. N. Miura, T. Raisen, G. Lu, N. Yamazoe: Sens. Actuators B Chem. **47**, 84 (1998)

22. J. H. Visser, R. E. Soltis, L. Rimai, E. M. Logothetis: Sens. Actuators B Chem. **9**, 233 (1992)

23. A. C. Eckbreth: *Laser Diagnostics for Combustion Temperature and Species* (Gordon and Breach Publishers, Amsterdam, 1996)

24. M. Versluis, G. Meijer, D. W. Chandler: Appl. Opt. **33**, 3289 (1994)

25. G. Meijer, D. W. Chandler: Chem. Phys. Lett. **192**, 1 (1992)

26. N. Georgiev, U. Westblom, M. Alden: Opt. Commun. **94**, 99 (1992)

27. K. Nyholm, R. Fritzon, N. Gregoriev, M. Alden: Opt. Commun. **114**, 76 (1995)

28. U. Westblom, S. Agrup, M. Alden, H. M. Hertz: Appl. Phys. B-Photo. Phys. **50**, 487 (1990)

29. H. Hasegawa, K. Tsukiyama: Appl. Phys. B-Lasers Opt. **63**, 311 (1996)

30. F. Di Teodoro, J. E. Rehm, R. L. Farrow, P. H. Paul: J. Chem. Phys. **113**, 3046 (2000)

31. A. P. Nefedov, V. A. Sinel'shchikov, A. D. Usachev, A. V. Zobnin: Appl. Opt. **37**, 7729 (1998)

32. J. S. Bernstein, A. Fein, J. B. Choi, T. A. Cool, R. C. Sausa, S. L. Howard, R. J. Locke, A.W. Miziolek: Combust. Flame **92**, 85 (1993)

33. S. Agrup, M. Alden: Chem. Phys. Lett. **189**, 211 (1992)

34. J. M. Seitzman, J. Haumann, R. K. Hanson: Appl. Opt. **26**, 2892 (1987)

35. J. Haumann, J. M. Seitzman, R. K. Hanson: Opt. Lett. **11**, 776 (1986)

36. M. G. Allen: Meas. Sci. Technol. **9**, 545 (1998)

37. W. Lenth: Opt. Lett. **8**, 575 (1983)

38. G. C. Bjorklund: Opt. Lett. **5**, 15 (1980)

39. J. A. Silver: Appl. Opt. **31**, 707 (1992)

40. N. Kagawa, O. Wada, R. Koga: Opt. Eng. **36**, 2586 (1997)

41. V. V. Liger: Spect. Act. A **55**, 2021 (1999)

42. M. G. Allen, K. L. Carleton, S. J. Davis, W. J. Kessler, C. E. Otis, D. A. Palombo, D. M Sonnenfroh: Appl. Opt. **34**, 3240 (1995)

43. P. Werle, F. Slemr, K. Maurer, R. Kormann, R. Mücke, B. Jänker: Opt. Lasers Eng. **37**, 101 (2002)

44. L. S. Rothman, A. Barbe, D. Chris Benner, L. R. Brown, C. Camy-Peyret, M. R. Carleer, K. Chance, C. Clerbaux, V. Danna, V. M. Devi, A. Fayt, J. –M. Flaud, R. R. Gamache, A. Goldman, D. Jacquemart, K. W. Jucks, W. J. Lafferty, J. –Y. Mandin, S. T. Massie, V. Nemtchinov, D. A. Newnham, A. Perrin, C. P. Rinsland, J. Schroeder, K. M. Smith, M. A. H. Smith, K. Tang, R. A. Toth, J. Vander Auwera, P. Varanasi, K. Yoshino: J. Quant. Spectrosc. Radiat. Transfer **82**, 5 (2003)

45. H. Teichert, T. Fernholz, V. Ebert: Appl. Opt. **42**, 2043 (2003)

46. D. S. Baer, J. B. Paul, M. Gupta, A. O'Keefe: Appl. Phys. B-Lasers Opt. **75**, 261 (2002)

47. R. M. Mihalcea, D. S. Baer, R. K. Hanson: Meas. Sci. Technol. **9**, 327 (1998)

48. R. M. Mihalcea, D. S. Baer, R. K. Hanson: Appl. Opt. **36**, 8745 (1997)

49. E. R. Furlong, R. M. Mihalcea, M. E. Webber, D. S. Baer, R. K. Hanson: AIAA J. **37**, 732 (1999)

50. J. J. Nikkari, J. M. DiIorio, M. J. Thomson: Appl. Opt. **41**, 446 (2002)

51. B. L. Upschulte, D. M. Sonnenfroh, M. G. Allen: Appl. Opt. **38**,1506 (1999)

52. D. M. Sonnenfroh, M. G. Allen: Appl. Opt. **36**, 3298 (1997)

53. J. Wang, M. Maiorov, D. S. Baer, D. Z. Garbuzov, J. C. Connolly, R. K. Hanson: Appl. Opt. **39**, 5579 (2000)

54. J. Wang, M. Maiorov, J. B. Jeffries, D. Z. Garbuzov, J. C. Connolly, R. K. Hanson: Meas. Sci. Technol. **11**, 1576 (2000)

55. M. E. Webber, J. Wang, S. T. Sanders, D. S. Baer, R. K. Hanson: Proc. Combust. Inst. **28**, 407 (2000)

56. J-C Nicolas, A. N. Baranov, Y. Cuminal, Y. Rouillard, C. Alibert: Appl. Opt. **37**, 7906 (1998)

57. M. Lackner, G. Totschnig, F. Winter, M. A. Maiorov, D. Z. Garbuzov, J. C. Connolly: Meas. Sci. Technol. **13**, 1545 (2002)

58. J. B. Jeffries: Private communication, Stanford University

59. B. Sumpf, J. P. Burrows, A. Kissel, H.-D. Kronfeldt, O. Kurtz, I. Meusel, J. Orphal, S. Voigt: J. Mol. Spectrosc. **190**, 226 (1998)

60. M. Murtz, M. Schaefer, T. George, J. S. Wells, W. Urban: Appl. Phys. B-Lasers Opt. **60**,31 (1995)

61. C. B. Carlisle, D. E. Cooper, H. Preier: Appl. Opt. **28**, 2567 (1989)

62. H. S. Lowry, C. J. Fisher: J. Quant. Spectrosc. Radiat. Transfer. **31**, 575 (1984)

63. P. L. Varghese, R. K. Hanson: J. Quant. Spectrosc. Radiat. Transfer **26**, 339 (1981)

64. P. L. Varghese, R. K. Hanson: J. Quant. Spectrosc. Radiat. Transfer **24**, 479 (1980)

65. R. G. Daniel, K. L. McNesby, A. W. Miziolek: Appl. Opt. **35**, 4018 (1996)

66. J. H. Miller, S. Elreedy, B. Ahvazi, F. Woldu, P. Hassanzadeh: Appl. Opt. **32**, 6082 (1993)

67. F. Hempel, J. Röpcke, F. Miethke, H. E. Wagner: Plasma Sources Sci. Technol. **11**, 266 (2002)

68. T. Güllük, H. E. Wagner, F. Slemr: Rev. Sci. Instr. **68**, 230 (1997)

69. A. A. Kosterev, F. K. Tittel: IEEE J. Quantum Electron. **38**, 582 (2002)

70. C. Peng, H. L. Zhang, H. Q. Le: Appl. Phys. Lett. **83**, 4098 (2003)

71. S. Wehe, M. G. Allen, X. Liu, J. B. Jeffries, R. K. Hanson: AIAA Pap. No. 2003-0588 (2003)

72. A. A. Kosterev, F. K. Tittel, R. Köhler, C. Gmachl, F. Capasso, D. L. Sivco, A. Y. Cho, S. Wehe, M. G. Allen: Appl. Opt. **41**, 1169 (2002)

73. J. Wagner, C. Mann, M. Rattunde, G. Weimann: Appl. Phys. A Mater. Sci. Process **78**, 505 (2004)

74. T. J. Kulp, S. E. Bisson, R. P. Bambha, T. A. Reichardt, U. –B. Goers, K. W. Aniolek, D. A. V. Kliner, B. A. Richman, K. M. Armstrong, R. Sommers, R. Schmitt, P. E. Powers, O. Levi, T. Pinguet, M. Fejer, J. P. Koplow, L. Goldberg, T. G. Mcrae: Appl. Phys. B-Lasers Opt. **75**, 317 (2002)

75. W. Chen, D. Boucher, F. K. Tittel: Recent Res. Devel. Applied Phys. **5**, 27 (2002)

76. F. K. Tittel, D. Richter, A. Fried: Topics Appl. Phys. **89**, 445 (2003)

77. W. Schade, T. Blanke, U. Willer, C. Rempel: Appl. Phys. B-Lasers Opt. **63**, 99 (1996)

78. T. Kelz, A. Schumacher, M. Nägele, B. Sumpf, H. –D. Kronfeldt: J. Quant. Spectrosc. Radiat. Transfer. **61**, 591 (1999)

79. A. Khorsandi, U. Willer, P. Geiser, W. Schade: Appl. Phys. B-Lasers Opt. **77**, 509 (2003)

80. D. G. Lancaster, D. Richter, F. K. Tittel: Appl. Phys. B-Lasers Opt. **69**, 459 (1999)

81. M. Seiter, M. W. Sigrist: Infrared Phys. Technol. **41**, 259 (2000)

82. D. Richter, D. G. Lancaster, R. F. Curl, W. Neu, F. K. Tittel: Appl. Phys. B-Lasers Opt. **67**, 347 (1998)

83. K. P. Petrov, R. F. Curl, F. K. Tittel: Appl. Phys. B-Lasers Opt. **66**, 531 (1998)

84. T. Töpfer, K. P. Petrov, Y. Mine, D. Jundt, R. F. Curl, F. K. Tittel: Appl. Opt. **36**, 8042 (1997)

85. K. P. Petrov, L. Goldberg, W. K. Burns, R. F. Curl, F. K. Tittel: Opt. Lett. **21**, 86 (1996)

86. G. Herzberg: *Molecular Spectra and Molecular Structure, I. Spectra of Diatomic Molecules* (D. Van Nostrand Company Inc., Princenton, NJ, 1950)

87. S. V. Khristenko, A. I. Maslov, V. P. Shevelko: *Molecules and Their Spectroscopic Properties* (Springer-Verlag, New York, 1998)

88. W. S. Struve: *Fundamentals of Molecular Spectroscopy* (John Wiley, New York, 1989)

89. L. Pauling, E. B. Wilson: *Introduction to Quantum Mechanics* (McGraw-Hill, New York, 1937)

90. H. Deslandres: Acad. Sci. Paris C. R. **106**, 842 (1888)

91. K. P. Huber, G. Herzberg: *Molecular Spectra and Molecular Structure, IV. Constants of Diatomic Molecules* (D. Van Nostrand Reinhold Company, New York, 1979)

92. D. C. Morton, L. Noreau: Astrophys. J. Suppl. Ser. **95**, 301 (1994)

93. M. Eidelsberg, F. Rostas: Astrophys. J. Suppl. Ser. **145**, 89 (2003)

94. S. R. Federman, M. Fritts, S. Cheng, K. M. Menningen, D. C. Knauth, K. Fulk: Astrophys. J. Suppl. Ser. **134**, 133 (2001)

95. G. Stark, B. R. Lewis, S. T. Gibson, J. P. England: Astrophys. J. **505**, 452 (1998)

96. E. N. Lassettre, A. Skerbele: J. Chem. Phys. **54**, 1597 (1971)

97. W. F. Chan, G. Cooper, C. E. Brion: Chem. Phys. **170**, 123 (1993)

98. K. Kirby, D. L. Cooper: J. Chem. Phys. **90**, 4895 (1989)

99. G. Guelachvili, D. De Villeneuve, R. Farrenq, W. Urban, J. Verges: J. Mol. Spectrosc. **98**, 64 (1983)

100. I. G. Nolt, J. V. Radostitz, G. DiLonardo, K. M. Evenson, D. A. Jennings, K. R. Leopold, M. D. Vanek, L.R. Zink, A. Hinz, K. V. Chance: J. Mol. Spectrosc. **125**, 274 (1987)

101. M. Schneider, J. S. Wells, A. G. Maki: J. Mol. Spectrosc. **139**, 432 (1990)

102. M. Schneider, M. K. Evenson, M. D. Vanek, D. A. Jennings, J. S. Wells, A. Stahn, W. Urban: Journal of Molecular Spectroscopy **135**, 197 (1989)

103. R. A. McClatchey, W. S. Benedict, S. A. Clough, D. E. Burch, R. F. Calfee, K. Fox, L. S. Rothman, J. S. Garing: *AFCRL Atmospheric Absorption Line Parameters Compilation* (Air Force Cambridge Research Laboratories AFCRL.TR-73-0096, Bedford, MA, 1973)

104. L. A. Young: J. Quant. Spectrosc. Radiat. Transfer. **8**, 693 (1968)

105. L. S. Rothman, C. P. Rinsland, A. Goldman, S. T. Massie, D. P. Edwards, J.-M. Flaud, A. Perrin, C. Camy-Peyret, V. Danna, J. Y. Mandin, J. Schroeder, A. McCann, R. R. Gamache, R. B. Wattson, K. Yoshino, K. V. Chance, K. W. Jucks, L. R. Brown, V. Nemtchinov, P. Varanasi: J. Quant. Spectrosc. Radiat. Transfer **60**, 665 (1998)

106. J. L. Dunham: Physic. Rev. **41**, 721 (1932)

107. A. Le Floch: Molec. Phys. **72**, 133 (1991)

108. R. Farrenq, G. Guelachvili, A. J. Sauval, N. Grevesse, B. C. Farmer: J. Mol. Spectrosc. **149**, 375 (1991)

109. N. Authier, N. Bagland, A. Le Floch: J. Mol. Spectrosc. **160**, 590 (1993)

110. K. Kirby-Docken, B. Liu: Astrophys. J. Suppl. Ser. **36**, 359 (1978)

111. C. Chackerian, R. H. Tipping: J. Mol. Spectrosc. **99**, 431 (1983)

112. J. M. Hure, E. Roueff: J. Mol. Spectrosc. **160**, 335 (1993)

113. D. Goorvitch: Astrophys. J. Suppl. Ser. **95**, 535 (1994)

114. T. D. Varberg, K. M. Evenson: IEEE Trans. Instrum. Meas. **42**, 412 (1993)

115. R. P. Lucht, R. C. Peterson, N. M. Laurendeau: *Fundamentals of Absorption Spectroscopy for Selected Diatomic Flame Radicals* (School of Mechanical Engineering Purdue University, West Lafayette, IN, 1978)

116. S. S. Penner: *Quantitative Molecular Spectroscopy and Gas Emissivities* (Addison-Wesley Publishing Company Inc., Reading, MA, 1959)

117. B. H. Armstrong: J. Quant. Spectrosc. Radiat. Transfer. **7**, 61 (1967)

118. J. Humlicek: J. Quant. Spectrosc. Radiant. Transfer. **21**, 309 (1979)

119. D. B. Fogel: IEEE Trans. Neural Networks **5**, 3 (1994)

120. W. H. Press, S. A. Teukolsky, W. T. Vetterling, B. P. Flannery: *Numerical Recipes in FORTRAN 77: The Art of Scientific Computing, Vol 1 of FORTRAN Numerical Recipes* (Cambridge University Press, Cambridge, 2001)

121. W. H. Press, S. A. Teukolsky, W. T. Vetterling, B. P. Flannery: *Numerical Recipes in FORTRAN 90: The Art of Parallel Scientific Computing, Vol 2 of FORTRAN Numerical Recipes* (Cambridge University Press, Cambridge, 2002)

122. R. R. Gamache, R. L. Hawkins, L. S. Rothman: J. Mol. Spectrosc. **142**, 205 (1990)

123. R. W. Boyd: *Nonlinear Optics* (Academic Press, San Diego, CA, 1992)

124. R. L. Aggarwal, B. Lax: In *Topics in Applied Physics*, Vol. 16, *Nonlinear Infrared Generation,* ed. by Y. R. Shen (Springer-Verlag, New York, 1977)

125. C. Fischer, W. Sigrist: Topics Appl. Phys. **89**, 97 (2003)

126. D. J. Bamford: *PPLN Tutorial* (Gemfire Corporation, Fremont, CA, 1998)

127. G. D. Boyd, D. A. Kleinman: J. Appl. Phys. **39**, 3597 (1968)

128. D. H. Jundt: Opt. Lett. **22**, 1553 (1997)

129. G. J. Dixon: Laser Foc. W. **37 no. 5**, 105 (1997)

130. J. A. Armstrong, N. Bloembergen, J. Ducuing, P. S. Pershan: Phys. Rev. **127**, 1918 (1962)

131. *DL-100 Doide Laser System Manual* (Toptica Photonics AG, Martinsried Germany, 2002)

132. *Laser Optics and Coatings, CVI Catalog* (CVI Laser Corporation , Albuquerque, NM, 1997)

133. S. F. Hanna, R. Barron-Jimenez, T. N. Anderson, R. P. Lucht, J. A. Caton, T. Walther: Appl. Phys. B-Lasers Opt. **75**, 113 (2002)

134. R. Barron-Jimenez, T. N. Anderson, J. A. Caton, R. P. Lucht, T. Walther, S. Roy, M. S. Brown, J. R. Gord: AIAA Pap. No. 03-0402 (2003)

135. A. McIlroy: Private communication, Sandia National Laboratories

136. A. Yariv: *Optical Electronics in Modern Communications* (Oxford University Press, New York, 1997)

137. T. Nakazawa, M. Tanaka: J. Quant. Spectrosc. Radiat. Transfer. **28**, 409 (1982)

138. J. M. Hartmann, L. Rosenmann, M. Y. Perrin, J. Taine: Appl. Opt. **27**, 3063 (1988)

139. A. Predoi-Cross, C. Luo, P. M. Sinclair, J. R. Drummond, A. D. May: J. Mol. Spectrosc. **198**, 291 (1999)

140. P. M. Sinclair, P. Duggan, R. Berman, A. D. May, J. R. Drummond: J. Mol. Spectrosc. **181**, 41 (1997)

141. J. P. Bouanich: J. Quant. Spectrosc. Radiat. Transfer. **13**, 953 (1973)

142. P. Varanasi: J. Quant. Spectrosc. Radiat. Transfer. **15**, 191 (1975)

143. S. M. Shoenung, R. K. Hanson: Combust. Sci. Technol. **24**, 227 (1981)

144. Q. V. Nguyen, B. L. Edgar, R. W. Dibble, A. Gulati: Combust. Flame **100**, 395 (1995)

145. B. Rosier, P. Gicquel, D. Henry, A. Coppalle: Appl. Opt. **27**, 360 (1988)

146. R. R. Skaggs, J. H. Miller: Combust. Flame **100**, 430 (1995)

147. R. D. Hancock, K. E. Bertagnolli, R. P. Lucht: Combust. Flame **109**, 323 (1997)

148. S. Frazzitta, K. Annamalai, J. Sweeten: J. Propul. Power **15**, 181 (1999)

149. K. Annamalai, B. Thien, J. Sweeten: Fuel **82**, 1183 (2003)

150. J. M. Sweeten, K. Annamalai, B. Thien, L. McDonald: Fuel **82**, 1167 (2003)

151. M. E. Webber, D. S. Baer, R. K. Hanson: Appl. Opt. **40**, 2031 (2001)

152. R. M. Mihalcea, M. E. Webber, D. S. Baer, R. K. Hanson, G. S. Feller, W. B. Chapman: Appl. Phys. B-Lasers Opt. **67**, 283 (1998)

153. A. A. Kosterev, R. F. Curl, F. K. Tittel, R. Köhler, C. Gmachl, F. Capasso, D. L. Sivco, A. Y. Cho: Appl. Opt. **41**, 573 (2002)

154. P. Horowitz, W. Hill: *The Art of Electronics* (Cambridge University Press, New York, 1989)

155. R. E. Simpson: *Introductory Electronics for Scientists and Engineers* (Allyn and Bacon, Boston, MA, 1987)

156. J. L. Guiñón, J. García-Antón, E. Ortega, V. Pérez-Herranz: Afinidad LX **506**, 396 (2003)

157. M. Satchel, Virtual Lock-in Project (Konstanz Germany, 1999) [http://fp.physik.uni-konstanz.de/LockIn/index.shtml]

APPENDIX A

"DIRECT_ABSORPTION" CODE

A.1 Modular Design

The "Direct_Absorption" code was developed to process experimental direct absorption data. It is based on a full-parameter fit to the experimental data as described in Chapter III. In addition to perform the full-parameter fit, the code reads, prepares, and normalizes the data. All these processes are carried out by different modules. The modular design allows for better understanding and easier debugging of the code.

The code is composed by a main program called "Direct_Absorption" which works as the user interface controlling the data input/output. The main code makes use of the other 21 modules. Each module has a specific purpose, declaration modules contain declarations of variables, constants, or other modules, utilities modules contain small subroutines commonly used, and the main modules contain the actual subroutines and functions for data fit. A brief description of each module and its internal subroutines are given in Table 14.

When the "Direct_Absoprtion" code runs, the user is prompted to select from a menu the normalization scheme to be used. Normalization schemes where discussed in Chapter IV. Depending on the user selection, the code request the total number of data files to be manipulated. The code names "air-scans" the scans taken for the no-CO case. If the number of files is larger than one, the data on the files is averaged reducing random noise as discussed in Chapter IV.

Next, the code requests the name of each data file. Files should be located under a folder "data." Data in the file must be formatted in five columns each 13 characters long with 8 decimal places. The columns in the data file corresponds to oscilloscope time reference, etalon trace, signal from the analytical detector, ECDL scanning ramp, and signal from the reference detector. To format the data as required by the code, an Excel macro "change_format" was used once the data was opened in an Excel spread sheet.

Next the code asks for a data file that contains the baseline scans for the analytical and reference detectors. Also the user should indicate if data is to be binned or "averaged" to reduce read noise and if so, how many neighboring channels to average. Finally the code requests the position in wavenumbers of the main transition. The code assigns this spectral position to the peak absorption on the data spectral region.

To continue, the code will separate the data into absorption 1 and 2 as indicated by the positive turn around of the ECDL scanning ramp. Each side of the ramp is processed separately and the user selects either half or both halves to be processed. Then the etalon trace of the first entered file is fitted by (89). The etalon trace is adjusted over 50 generations of the evolutionary algorithm and the Levenberg-Marquardt method. Only one etalon trace is fitted and the others are displaced so that the etalon peaks on the trace match the position of the fitted trace. From these fitting and matching processes the output files "EtalonOut.txt" and "MatchEtalonOut.txt" are generated in the folder "results."

Then data is normalized according to the user selected scheme and frequency conversion is performed. The resulting analytical and reference traces are written in the output file "TraceOut.txt." At this point, binning of the neighboring points and fitting to the absorption trace are performed. Fitting of the absorption trace is also carried out by the evolutionary routine over 100 generations with 100 sets per generation fitting the absorption trace 10000 times with different sets of parameters. To select the parameter set, the user is required to enter the range for each parameter. When a parameter is known, to hold it fix the upper and lower limits of the range must be equal. After the evolutionary algorithm, a best-fit parameter set was chosen and it is used as the initial guess for the Levenberg-Marquardt routine. The output file "AbsOut.txt" contains the resulting best-fit parameters set, information on the fitting procedure such as the noise rms value , processed files and the data for the normalized absorption trace, the best-fit trace, and the residuals of the best-fit to the experimental data.

Output from the "Direct_Absorption" code can be easily visualized with the LabView program "evaluate COx spectra.vi." This LabView code also allows the user to perform a custom fit to the data by selecting the parameters T, P, L, X_{CO}, X_{CO2}, GF_{CO}, and GF_{CO2}.

Module	Description
Direct_Absorption.f90	This is the main program. Process the collected data in a direct optical CO/CO_2 absorption experiment and fits it to a Voigt profile using a set of parameters that when optimized will minimize the χ^2 value of the fit.
AbsorptionFit.f90	This routine controls the fitting of the absorption data to Beer's law by using the function implemented in AbsCalc.F90.
EtalonFit.f90	This routine controls the fitting of the etalon data to the etalon equation by using the function implemented in EtalonFunction.F90. Given the etalon data it returns the best-fit parameter set.
AbsCalc.f90	Given the absorption parameters (T[K], P[torr], X_{CO}[ppm], X_{CO2}[%], L[m], GF_{CO}, GF_{CO2}) and the wavenumber (ω), the spectral absortivity is calculated.
EtalonFunction.f90	It is the user-supplied function to evaluate the etalon transmitted intensity at each time using the parameters. The etalon function is defined by (89).
LMBestFit.f90	This routine is used to control the application of the Levenberg-Marquardt method.
evolution.f90	Implements the evolutionary algorithm. Given the limits of each parameter of the user defined function the best fit to the data is obtained by means of the evolutionary algorithm.
Routines adapted from Numerical Recipes in Fortran 90 [120, 121]	
mrqmin.f90	Routine to implement the non-linear Levenberg-Marquardt method.
Covsrt.f90	Expand in storage the covariance matrix, so as to take into account parameters that are being held fixed.
Gaussj.f90	Implements Gauss-Jordan elimination for the solution of linear equations.
rann.f90	Minimal random number generator of Park and Miller combined with Marsaglia shift sequence. Returns a uniform random deviate between 0.0 and 1.0.
Definition modules	
nrtype.f90	This module is adapted from Numerical Recipes in Fortran 90 [120, 121]. It is used to define the type of variables used through the code.
nr.f90	Interface module for the routines adapted from Numerical Recipes in Fortran 90 [120, 121].
HitranInfo.f90	This module establishes the global variables that contain the spectroscopic parameters from HITRAN.
AdjustConstants.f90	Define the constants that control the execution of "Direct_Absorption" code.
absCOconstants.f90	Define constants used by the "Direct_Absorption" code.
usercodes.f90	This module is the interface module for developed codes: AbsorptionFit, EtalonFit, evolution, and LMBestFit.
Utilities modules	
nrutil.f90	This module is adapted from Numerical Recipes in Fortran 90 [120, 121]. It is used to define some small functions used through the code as semi-intrinsic functions.
Fileutil.f90	This module contains the routines required to perform operations on the data files generated by the oscilloscope.
average_files	The input matrix contains the information of all data files. The analytical and reference columns of each file are properly averaged.
cut_in_half	The ramp trace is examined in order to extract the uphill and downhill portions.

TABLE 14 Description of modules and internal subroutines

Module	Description
Etalonutil.f90	This module contains the routines required to handle the etalon trace.
adjust_traces	Compares the peak centers to the first etalon trace and adjust the traces so that the etalon traces coincide.
binning_data	To bin data from the given arrays.
etalon_fit_check	This subroutine is to check the fit of the etalon by comparing the peaks center position.
etalon_parameter_limits	This subroutine establishes the limits to each parameter used to fit the etalon trace.
get_etalon_peaks	Given the etalon trace, this routine finds the center position of each peak.
mirror_2ndhalf	Since the second half of the data occurs as a mirror image of the first then the second half of the data is mirrored so that the etalon, ramp and detectors signals have similar shapes.
darwinutil.f90	This module contains the utilities required for implementation of the evolutionary algorithm.
calcchisq	Evaluates the chi-square value for a fit between the data and the evaluation of the indicated function which is user defined.
Sortchisq	Sorts the parameter sets according to their χ^2 value. It also checks for very similar parameters sets and eliminate the repeated sets.
absCOutil.f90	This module contains the utilities used by the routine AbsorptionFit.f90 that calculates the absorption.
abs_parameter_limits	This subroutine asks the user to establish the limits to each of the parameters used to fit the absorption data.
FindAbsorptionCoeff	Evaluates the total spectral absorption coefficient k_ω [cm^{-1}] at the given frequency.
PartitionSums	Evaluates the Partition Sums [$Q(T)$] and its derivative respect to temperature.
ReadTransitions	Gets the name of the file that contains transition information and retrieves the information of the lines within the range of the data. Line spectroscopic parameters obtained from the HITRAN database for CO and CO_2 are formatted for the code and compiled in the file "COLines-hitemp-isotopes.prn" and "CO2Lines-hitemp-isotopes" respectively.
Voigtprofile	Calculates the Voigt profile given the Voigt parameter (a) and x. This routine uses the algorithm by Humlicek [118].

TABLE 14 Continued

A.2 Selected Modules

In this section the Fortran 90 code lines for selected modules are included. The selected modules are: the main program "Direct_Absoprtion", the module "AbsorptionFit" that controls the fitting procedure for the absorption data, "AbsCalc" and "FindAbsoprtionCoeff" which compose the user defined functions for the absorption fit and the modules for the evolutionary and Levenberg-Marquardt methods "evolution" and "LMBestFit" respectively.

A.2.1 Main program "Direct_Absorption"

```
program Direct_Absorption
!       This program will process the collected data in a direct optical CO/CO2
!absorption experiment and fit this data to a Voigt profile(s) using a set of parameters
!that optimized will minimize the chi-square value of the fit.
!Output are two pairs of files containing the data sets for [NUdata,Absdata],
![NUfit,AbsFit,residuals]and the second file contains the best fit parameters values and
!information related to the fit. The second pair of files refers to the fit of the other
!half of data(mirror image of the first half).
!
!       Created 10/1/2003 by Rodolfo Barron-jimenez
!       Log modifications:
!       10/27/03 Change sp to be double precision (see page 1362 in Numerical Recipes)
!       12/03/03 Include individual standard deviation of each point from the averaged
!files
!       12/24/03 Generate the stdev.txt file and treat the case of one data file with
!stdev=1.0
!       12/26/03 Program four schemes to evaluate the absorption from the data files
!       04/30/04 Error found inthe stdev evaluation. Some values equal 0. Corrected by
!the average of all stdev
!       05/04/04 Inclusion of the random number routine from NR in Fortran
!       05/05/04 Improvement to the etalon fit checking routine
!
!       Version 8 (don't forget, change the screen printout)
!
        use nrtype
        use AdjustConstants
        use absCOconstants
        use nrutil, only: nrerror
        use fileutil, only: fix_times,cut_in_half,average_files
        use etalonutil, only: mirror_2ndhalf, get_etalon_peaks, adjust_traces,
binning_data
        use usercodes, only: EtalonFit,AbsorptionFit

        implicit none
        integer(i4b):: ngasfiles,nairfiles,nfiles,totalcol,half,ave
        integer(i4b):: i,j,EoF,dumi1,dumi2,count,maxcount
        integer(i4b), dimension(1):: dumi
        integer(i4b), dimension(:), allocatable:: npeaks
        integer(i4b), dimension(:,:), allocatable:: ndata
        real(sp):: centralNU,chisq,rms
        real(sp), dimension(4):: poly
        real(sp), dimension(:), allocatable:: tiempo, etalon, fitEtalon, signal,refer,
wsig, wref, freq, NU, normabs, NUfit, AbsFit,          res, freqdet, freqdetfit
        real(sp), dimension(:,:), allocatable:: rawdata, dummallo, peaktime, gastesrr,
airtesrr, dumm, dumm1, dumm2
        real(sp), dimension(:,:,:), allocatable:: rawdatahalf
        real(sp), dimension(netalonparams):: etalonparams
        real(sp), dimension(nabsparams):: NAparams,err
        real(sp), dimension(halves,totalrows,col):: tesrrbl
        character(len=1):: answ,caso
        character(len=40), dimension(:), allocatable:: filename,nameout


        write(*,*) 'Direct_Absorption for CO/CO2  (version 8)'
        write(*,*) '-------------------------------------------'
        write(*,*)

        !Get from user type of data reduction
        caso='r'
        do while ((caso /= 'A') .and. (caso /= 'B') .and. (caso /= 'C') .and. (caso /=
'D'))
                write(*,*) 'To reduce collected data to absorption trace there are 4
options'
                write(*,*) '   a) Use reference detector trace as the no-abs case'
                write(*,*) '      Scale it with air traces'
                write(*,*) '   b) Use reference detector trace as the no-abs case'
                write(*,*) '      Scale it with the maximums (no air scans)'
                write(*,*) '   c) Use only signal detector'
                write(*,*) '      Use the signal trace for the air scans as the no-abs
case'
                write(*,*) '   d) Use only signal detector and fit a 3rd degree polynomio'
                write(*,*) '      to the non-atenuated regions as the no-abs case'
                write(*,*) 'Enter selection: '
```

```
                read(*,*) caso
                write(*,*)
                select case (caso)
                case ('a')
                        caso = 'A'
                case ('b')
                        caso = 'B'
                case ('c')
                        caso = 'C'
                case ('d')
                        caso = 'D'
                end select
        end do

        !Get from user the names of the files to process
        write(*,*) 'How many Gas Files? '
        read(*,*) ngasfiles
        if (ngasfiles < 1) then
                write(*,*) 'Must indicate at least one file with GAS data'
                write(*,*) 'How many Gas Files? '
                read(*,*) ngasfiles
        end if
        write(*,*)
        if ((caso == 'A') .or. (caso == 'C')) then
                write(*,*) 'How many Air/No-Gas Files? '
                read(*,*) nairfiles
                if (nairfiles < 1) then
                        write(*,*) 'Must indicate at least one file with Air/No-gas data'
                        write(*,*) 'How many Air/No-Gas Files? '
                        read(*,*) nairfiles
                end if
        else
                nairfiles=0
        end if
        write(*,*)

        !Get data from files
        nfiles=ngasfiles+nairfiles+1          !1 is added to account for the baseline file
        totalcol=col*(nfiles-1)
        allocate(rawdata(totalrows,totalcol),filename(nfiles))
        do i=0, ngasfiles-1
                write(*,*) ' Name of the',i+1,'-th GAS file'
                read(*,*) filename(i+1)
                open(unit=10, file='data\'//filename(i+1), status='unknown')
                EoF=0
                j=1
                do while (EoF >= 0)
                        read(10,'(<col>f13.8)', iostat=EoF) rawdata(j,(i*col)+1:(i*col)+
col)
                        j=j+1
                end do
                close(10)
        end do
        write(*,*)

        do i=ngasfiles, ngasfiles+nairfiles-1
                write(*,*) ' Name of the',i-ngasfiles+1,'-th AIR file'
                read(*,*) filename(i+1)
                open(unit=10, file='data\'//filename(i+1), status='unknown')
                EoF=0
                j=1
                do while (EoF >= 0)
                        read(10,'(<col>f13.8)', iostat=EoF)
rawdata(j,(i*col)+1:(i*col)+col)
                        j=j+1
                end do
                close(10)
        end do
        write(*,*)

        !Take the data from each file, and extract the up and down hill of the ramp
        allocate(ndata(2,nfiles))
        allocate(rawdatahalf(halves,totalrows,totalcol))
        allocate(dumm(totalrows,col),dumm1(totalrows,col),dumm2(totalrows,col))
        do j=0, ngasfiles+nairfiles-1
                dumm(:,:)=rawdata(:,(j*col)+1:(j*col)+col)
```

```
                call cut_in_half(dumm,dumm1,dumm2,dumi1,dumi2)
                call mirror_2ndhalf(dumm2(:dumi2,:))

                call fix_times(dumm1(:dumi1,:))
                call fix_times(dumm2(:dumi2,:))

                ndata(1,j+1)=dumi1
                ndata(2,j+1)=dumi2
                rawdatahalf(1,:dumi1,(j*col)+1:(j*col)+col)=dumm1(:dumi1,:)
                rawdatahalf(2,:dumi2,(j*col)+1:(j*col)+col)=dumm2(:dumi2,:)
        end do
        deallocate(rawdata)

        !Get baseline information
        answ='r'
        do while ((answ /= 'n') .and. (answ /= 'N') .and. (answ /= 'y') .and. (answ /=
'Y'))
                write(*,*) 'Use baseline? y/n'
                read(*,*) answ
        end do
        if ((answ == 'y') .or. (answ == 'Y')) then
                write(*,*) ' Name of the BASELINE file'
                read(*,*) filename(nfiles)
                write(*,*)
                open(unit=10, file='data\'//filename(nfiles), status='unknown')
                EoF=0
                j=1
                dumm(:,:)=0.0_sp
                do while (EoF >= 0)
                        read(10,'(<col>f13.8)', iostat=EoF) dumm(j,:)
                        j=j+1
                end do
                close(10)
                call cut_in_half(dumm,dumm1,dumm2,ndata(1,nfiles),ndata(2,nfiles))
                call mirror_2ndhalf(dumm2(:ndata(2,nfiles),:))
                tesrrbl(1,:,:)=dumm1(:,:)
                tesrrbl(2,:,:)=dumm2(:,:)
                tesrrbl(1,ndata(1,nfiles)+1:,3)=(sum(tesrrbl(1,:ndata(1,nfiles),3)))/
ndata(1,nfiles)
                tesrrbl(1,ndata(1,nfiles)+1:,5)=(sum(tesrrbl(1,:ndata(1,nfiles),5)))/
ndata(1,nfiles)
                tesrrbl(2,ndata(2,nfiles)+1:,3)=(sum(tesrrbl(2,:ndata(2,nfiles),3)))/
ndata(1,nfiles)
                tesrrbl(2,ndata(2,nfiles)+1:,5)=(sum(tesrrbl(2,:ndata(2,nfiles),5)))/
ndata(1,nfiles)
        else
                tesrrbl(:,:,:)=0.0_sp
        end if
        deallocate(dumm,dumm1,dumm2)

        !Asks averaging of data
        answ='r'
        do while ((answ /= 'n') .and. (answ /= 'N') .and. (answ /= 'y') .and. (answ /=
'Y'))
                write(*,*) 'Average data? y/n'
                read(*,*) answ
        end do
        if ((answ=='y') .or. (answ=='Y')) then
                write(*,*) 'How many points to be averaged'
                read(*,*) ave
                write(*,*)
        else
                ave=1
        end if

        !Get main transition location
        write(*,*) 'Give the location [in cm^-1] of the main transition in the data'
        read(*,*) centralNU
        write(*,*)

        !Asks for which half of the data to process
        answ='r'
        do while ((answ /= '1') .and. (answ /= '2') .and. (answ /= 'B') .and. (answ /=
'b'))
                write(*,*) 'Which half of the data to be processed?:'
                write(*,*) '    1 - First half'
```

```
                write(*,*) '    2 - Second half'
                write(*,*) '    B - Both halves'
                read(*,*) answ
        end do
        if ((answ == 'B') .or. (answ == 'b')) then
                half=1
                maxcount=2
        else if (answ == '1') then
                half=1
                maxcount=1
        else
                half=2
                maxcount=1
        end if

        !work each half of the data independently
        count=1
        do while (count <= maxcount)

                write(*,*)
                write(*,*) 'Processing data half: ',half
                write(*,*) '-------------------------------'
                write(*,*)

                !Fits etalon of the first data file
                allocate(dummallo(ndata(half,1),2))
                dummallo(:,:)=rawdatahalf(half,:ndata(half,1),1:2)

                call binning_data(dummallo(:,1),dummallo(:,2),dumi1,Etalonbin)
                allocate(etalon(dumi1),tiempo(dumi1),fitEtalon(dumi1))
                tiempo(:)=dummallo(:dumi1,1)
                etalon(:)=dummallo(:dumi1,2)
                call EtalonFit(tiempo,etalon,fitEtalon,etalonparams)
                deallocate(dummallo)

                !Save etalon fitting data
                allocate(nameout(netalonparams))
                nameout(1)='               Frequency offset'
                nameout(2)='   Frequency linear coefficient'
                nameout(3)='Frequency cuadratic coefficient'
                nameout(4)='                Etalon finesse'
                nameout(5)='             Incident intensity'
                nameout(6)='                    Data offset'
                nameout(7)='                          1/FSR'
                if (half == 1) then
                        open(unit=13, file='results\EtalonOut I.txt', status='replace')
                else
                        open(unit=13, file='results\EtalonOut II.txt', status='replace')
                end if
                write(13,*) 'Best parameters for Etalon curve-fit'
                do j=1, netalonparams
                        write(13,'(a31,": ",f20.10)') nameout(j),etalonparams(j)
                end do
                write(13,*)
                write(13,'(3a20)') '        Channel No.','         Etalon Data','
Fit Etalon'
                do j=1, dumi1
                        write(13,'(3f20.10)') tiempo(j),etalon(j),fitEtalon(j)
                end do
                close(13)
                deallocate(tiempo,etalon,fitEtalon,nameout)

                !get peaks for each etalon in the data files
                allocate(peaktime(nfiles-1,maxpeaks),npeaks(nfiles-1))
                do j=0, ngasfiles+nairfiles-1
                        allocate (tiempo(ndata(half,j+1)),etalon(ndata(half,j+1)))
                        tiempo(:)=rawdatahalf(half,:ndata(half,j+1),(j*col)+1)
                        etalon(:)=rawdatahalf(half,:ndata(half,j+1),(j*col)+2)
                        call get_etalon_peaks(tiempo,etalon,peaktime(j+1,:),npeaks(j+1),
Etalonbin)
                        deallocate(tiempo,etalon)
                end do

                !Save peaks matching info
                if (half == 1) then
```

```
                        open(unit=13, file='results\MatchEtalonOut I.txt',
status='replace')
                else
                        open(unit=13, file='results\MatchEtalonOut II.txt',
status='replace')
                end if
                write(13,*) 'Adjustment of etalon peaks'
                do j=1, nfiles-1
                        dumi2=npeaks(j)
                        write(13,'("file ",i3,<dumi2>f20.10)') j,peaktime(j,:dumi2)
                        allocate(signal(dumi2))
                        signal(:)=dble(j-1)
                        write(13,'("        ",<dumi2>f20.10)') signal(:)
                        deallocate(signal)
                end do
                close(13)

                !Adjust files to match etalons to the etalon on the first data file
                do j=1, ngasfiles+nairfiles-1
                        call adjust_traces(rawdatahalf(half,:ndata(half,1),1),rawdatahalf
(half,:ndata(half,j+1),(j*col)+1),peaktime(1,:npeaks(1)),peaktime(j+1,:npeaks(j+1)))
                end do
                deallocate(npeaks,peaktime)

                !Average the files' signal and reference columns also evaluates the
standard deviation of each data point
                allocate(dumm1(totalrows,col),dumm2(totalrows,col))
                call average_files(rawdatahalf(half,:,:),ngasfiles,nairfiles,dumm1,dumm2,
dumi1)
                allocate(gastesrr(dumi1,col),airtesrr(dumi1,col))
                gastesrr(:,:)=dumm1(:dumi1,:)
                airtesrr(:,:)=dumm2(:dumi1,:)
                deallocate(dumm1,dumm2)

                !Perform absorption normalization and time to frequency conversion
                allocate(freq(dumi1),NU(dumi1),normabs(dumi1),signal(dumi1),refer(dumi1))
                signal(:)=gastesrr(:,3)-tesrrbl(half,:dumi1,3)

                if (half == 1) then
                        open (unit=16, file='results\SignaltraceI.txt', status='replace')
                else
                        open (unit=16, file='results\SignaltraceII.txt', status='replace')
                end if
                do j=1, dumi1
                        write(16,'(f20.10,",",f20.10)') gastesrr(j,1),signal(j)
                end do
                close(16)

                poly(:)=0.0_sp
                write(*,*) 'Data is being treated using the scheme:'
                select case (caso)
                case ('A')
                        refer(:)=gastesrr(:,5)-tesrrbl(half,:dumi1,5)
                        write(*,*) 'a) Use reference detector trace as the no-abs case'
                        write(*,*) '   Scale it with air traces'
                        refer(:)=refer(:)*(airtesrr(:,3)-tesrrbl(half,:dumi1,3))/
(airtesrr(:,5)-tesrrbl(half,:dumi1,5))
                case ('B')
                        refer(:)=gastesrr(:,5)-tesrrbl(half,:dumi1,5)
                        write(*,*) 'b) Use reference detector trace as the no-abs case'
                        write(*,*) '   Scale it with the maximums (no air scans)'
                        allocate(wsig(dumi1),wref(dumi1))
                        wsig(:)=signal(:)
                        wref(:)=refer(:)
                        call binning_data(wsig,wref,dumi2,tracebin)
                        refer(:)=refer(:)*(wsig(1))/(wref(1))        !Use the First (most
left) bin of the data to scale the reference trace deallocate(wsig,wref)
                case ('C')
                        write(*,*) 'c) Use only signal detector'
                        write(*,*) '   Use the signal trace for the air scans as the no-
abs case'
                        refer(:)=(airtesrr(:,3)-tesrrbl(half,:dumi1,3))
                case ('D')
                        write(*,*) 'd) Use only signal detector'
                        write(*,*) '   Use a 3rd degree polynomial fit of the non-
atenuated regions'
```

```
                        write(*,*) '      as the no-abs case'
                        write(*,*) ' NOTE: the file: results\Signaltrace.txt provides the
signal trace'
                        write(*,*) '       whose un-atenuated regions must be fitted'
                        write(*,*)
                        answ='r'
                        write(*,*) ' For this data reduction case the coefficients of the
polynomio are needed'
                        do while ((answ /= '1') .and. (answ /= '2'))
                                write(*,*) ' Enter the coefficients:'
                                write(*,*) '    1 - by user'
                                write(*,*) '    2 - from file results\poly.txt'
                                read(*,*) answ
                        end do
                        if (answ == '1') then
                                write(*,*) 'Cubic coefficient:'
                                read(*,*) poly(4)
                                write(*,*) 'Cuadratic coefficient:'
                                read(*,*) poly(3)
                                write(*,*) 'Linear coefficient:'
                                read(*,*) poly(2)
                                write(*,*) 'Independent coefficient:'
                                read(*,*) poly(1)
                        else
                                open (unit=16, file="results\poly.txt",status="unknown")
                                do j=1, 4
                                        read(16,'(e20.10)') poly(j)
                                end do
                                close (16)
                        end if
                        refer(:)=(poly(4)*((gastesrr(:,1))**3))+(poly(3)*((gastesrr (:,1)
)**2))+ (poly(2)*gastesrr(:,1))+poly(1)
                end select
                write(*,*)
                write(*,*)

                normabs(:)=1.0_sp-(signal(:)/refer(:))

                freq(:)=((etalonparams(3))*((gastesrr(:,1)-etalonparams(1))**2))+
((etalonparams(2))*(gastesrr(:,1)-etalonparams(1)))
                freq(:)=freq(:)*etalonparams(7)*EtalonFSR    !Units are given by the
EtalonFSR [GHz]
                NU(:)=(freq(:)*1.0e9_sp)/lightspeed                 !lightspeed is in
[cm/s] check absCOconstants.f90
                dumi=maxloc(normabs)
                NU(:)=NU(:)+centralNU-NU(dumi(1))
                deallocate(gastesrr,airtesrr)

                !Save signal and reference traces on frequency
                if (half == 1) then
                        open(unit=13, file='results\TraceOut I.txt', status='replace')
                else
                        open(unit=13, file='results\TraceOut II.txt', status='replace')
                end if
                write(13,*) 'Signal & reference traces versus Wavenumber'
                write(13,*)
                write(13,'(3a20)') '  Wavenumber [cm^-1]','          Signal [V]','
Reference [V]'
                do j=1, dumi1
                        write(13,'(3f20.10)') NU(j),signal(j),refer(j)
                end do
                close(13)
                deallocate(signal,refer)

                !Average data to reduce noise by binning it
                call binning_data(NU,normabs,dumi1,ave)
                allocate(dumm(totalrows,col))
                dumm(:dumi1,1)=NU(:dumi1)
                dumm(:dumi1,2)=normabs(:dumi1)
                deallocate(NU,freq,normabs)
                allocate(NU(dumi1),normabs(dumi1))
                NU(:)=dumm(:dumi1,1)
                normabs(:)=dumm(:dumi1,2)
                deallocate(dumm)

                !Perform fit on the absorption trace
```

```
                allocate(NUfit(dumi1),AbsFit(dumi1),res(dumi1))
                call AbsorptionFit(NU,normabs,NUfit,AbsFit,NAparams,err,chisq,res)
                allocate(freqdet(dumi1),freqdetfit(dumi1))
                rms=dsqrt(chisq/dumi1)
                freqdet(:)=(NU(:)-centralNU)*lightspeed*1.0e-9      !original Freq
detuning [GHz] for data
                freqdetfit(:)=(NUfit(:)-centralNU)*lightspeed*1.0e-9 !Freq detuning [GHz]
for the fitted data & theoretical curves

                !Save Absorption fitting data
                allocate(nameout(nabsparams))
                nameout(1)='                Temp [K]'
                nameout(2)='           Pressure [torr]'
                nameout(3)='   CO concentration [ppm]'
                nameout(4)='    CO2 concentration [%]'
                nameout(5)='          Path length [m]'
                nameout(6)='     gammafactorCO [adim]'
                nameout(7)='    gammafactorCO2 [adim]'
                nameout(8)='            NUoff [cm^-1]'
                nameout(9)='            absoff [adim]'
                if (half == 1) then
                        open(unit=13, file='results\AbsOut I.txt', status='replace')
                        open(unit=14, file='results\AbsparamI.txt', status='replace')
                        open(unit=15, file='results\AbsdataI.txt', status='replace')
                else
                        open(unit=13, file='results\AbsOut II.txt', status='replace')
                        open(unit=14, file='results\AbsparamII.txt', status='replace')
                        open(unit=15, file='results\AbsdataII.txt', status='replace')
                end if
                write(13,*) 'Best parameters for Absorption curve-fit'
                write(13,*)
                do j=1, nabsparams
                        write(13,'(a25,": ",f20.10," ± ",f20.10)') nameout(j),
NAparams(j), err(j)
                        write(14,'(f20.10)') NAparams(j)
                end do
                write(13,'("                      chisq:",f20.10)') chisq
                write(13,'("                        rms:",f20.10)') rms
                write(13,'("      Freq Det offset [GHz]:",f20.10)') NAparams(8)*
lightspeed*1.0e-9
                write(13,'("    Main Transition [cm^-1]:",f20.10)') centralNU
                write(13,'("    Data averaged over [ch]:",i10)') ave
                write(13,*)
                write(13,'(" Used scheme to reduce data: ",a1)') caso
                write(13,*) 'For scheme D polynomial coeff. used (otherwise, ignore)'
                write(13,'(a17,e20.11)') 'Independent coeff', poly(1)
                write(13,'(a17,e20.11)') '     Lineal coeff', poly(2)
                write(13,'(a17,e20.11)') '  Cuadratic coeff', poly(3)
                write(13,'(a17,e20.11)') '      Cubic coeff', poly(4)
                write(13,*)
                write(13,*) 'Files processed:'
                do j=1, nfiles
                        write(13,'(a40)') filename(j)
                end do
                write(13,*)
                write(13,'(5a20)') '      NU fit [cm^-1]','      Freq Det [GHz]','
Norm. Absorption','    Theo. Absorption','    Residuals [adim]'
                do j=1, dumi1
                        write(13,'(5f20.10)') NUfit(j),freqdetfit(j),normabs(j),
AbsFit(j),res(j)
                        write(15,'(f20.10,",",f20.10,",",f20.10,",",f20.10)') freqdet(j),
freqdetfit(j),normabs(j),AbsFit(j)
                end do
                close(13)
                close(14)
                close(15)
                deallocate(nameout)
                deallocate(NU,freqdet,normabs,NUfit,freqdetfit,AbsFit,res)

                half=half+1
                count=count+1
        end do

        write(*,*)
        write(*,*) '----------------------------'
        write(*,*) 'Data processing is completed'
```

```
        write(*,*) ' ********************************** '
        read(*,*)

end program Direct_Absorption
```

A.2.2 AbsorptionFit.f90

```
subroutine AbsorptionFit(NUdata,Absdata,NUfit,AbsFit,params,err,chisq,res)
!       This routine controls the fitting of the absorption data [NUdata,Absdata] to
!Beer's law by using the function implemented in AbsCalc.F90.  Given the data sets
!Wavenumbers versus Absorption it returns the best-parameters set params, the evaluation
!of the best-fit [NUfit,AbsFit] at these parameters, the chi-square value of the fit
!chsq, the error err associated with each parameter, and the residuals (res(i) [%]
!=((AbsFit(i)-Absdata(i))*100%)/AbsFit(i)).
!Note: bestfittol is the tolerance to which chi-square is reduced, this parameter is
!specified in the
!module AdjustConstants.


        use nrtype
        use AdjustConstants
        use HitranInfo
        use absCOconstants
        use nrutil, only: assert_eq,nrerror
        use absCOutil, only: ReadTransitions,abs_parameter_limits
        use usercodes, only: evolution,LMBestFit

        implicit none
        real(sp), dimension(:), intent(in):: NUdata
        real(sp), dimension(:), intent(inout):: Absdata
        real(sp), dimension(:), intent(out):: params,NUFit,AbsFit,err,res
        real(sp), intent(out):: chisq
        interface
                subroutine AbsCalc(NU,absparams,absorption,dyda)
                        use nrtype
                        real(sp), dimension(:), intent(in):: NU,absparams
                        real(sp), dimension(:), intent(out):: absorption
                        real(sp), dimension(:,:), intent(out):: dyda
                end subroutine AbsCalc
        end interface

        integer(i4b):: ndata,nlines,dumi,jj
        real(sp):: NUoffset,junk
        real(sp), dimension(size(NUdata)):: sigma
        real(sp), dimension(maxlines,nprop):: dumm
        real(sp), dimension(size(NUdata),nabsparams):: dumm1
        real(sp), dimension(nabsparams):: parammax,parammin
        logical(lgt), dimension(nabsparams):: maskara

        dumi=assert_eq(nabsparams,size(params),size(err), 'AbsorptionFit 1')
        ndata=assert_eq(size(NUdata),size(Absdata),size(res), 'AbsorptionFit 2')
        ndata=assert_eq(size(NUdata),size(NUFit),size(AbsFit), 'AbsorptionFit 3')

        !Read CO transition data
        call ReadTransitions(HitempCOfile,dumm,nlines,NUdata(1),NUdata(ndata))
        if (nlines > maxlines) call nrerror('Number of CO lines in range is larger than
maximum specified [AbsorptionFit]')
        allocate (linepropCO(nlines,nprop))
        linepropCO(:,:)=dumm(:nlines,:)

        !Read CO2 transition data
        call ReadTransitions(HitempCO2file,dumm,nlines,NUdata(1),NUdata(ndata))
        if (nlines > maxlines) call nrerror('Number of CO2 lines in range is larger than
maximum specified [AbsorptionFit]')
        allocate (linepropCO2(nlines,nprop))
        linepropCO2(:,:)=dumm(:nlines,:)

        !Use evolutionary algorith to get params initial values
        call abs_parameter_limits(NUdata,Absdata,maskara,parammax,parammin)
        call evolution(NUdata,Absdata,parammax,parammin,params,chisq,AbsCalc,2)
```

```
        !Using the evolution best set of params as initial guess, use Levenberg-Marquardt
method
        open(unit=21, file='results\stdev.txt', status='unknown')
                do jj=1, ndata
                        read(21,'(2f20.10)') junk,sigma(jj)
                end do
        close(21)

        write(*,*)
        write(*,*) 'Process Absorption LM Fit:'
        call LMBestFit(NUdata,Absdata,params,maskara,AbsCalc,chisq,err,bestfittol,sigma)

        NUfit=NUdata+params(8)
        NUoffset=params(8)
        params(8)=0.0_sp
        call AbsCalc(NUfit,params,Absfit,dumm1)
        params(8)=NUoffset

        AbsFit(:)=AbsFit-params(9)
        params(9)=-1.0_sp*params(9)
        Absdata(:)=Absdata(:)+params(9)

        res(:)=AbsFit(:)-Absdata(:)

        !calcualte chisq because the value from LMBestfit includes division by
stdeviations
        chisq=0.0_sp
        do jj=1, ndata
                chisq=chisq+(res(jj)**2)
        end do
        write(*,*) 'LM chisq=',chisq
        write(*,*)

        deallocate (linepropCO,linepropCO2)
end subroutine absorptionFit
```

A.2.3 AbsCalc.f90

```
subroutine AbsCalc(NU,absparams,absorption,dyda)
!       Given the absparams(Temp [K], P[torr], xgasCO [ppm], xgasCO2 [%], length [m],
!gammafactorCO [adim], gammafactorCO2 [adim], NUoff [cm^-1], absoff [adim]) and the
!wavenumber NU, the absorption[=1-exp(-kw*length)+absoff] is calculated.
!The rutine also evaluates the derivatives dyda of abs with respect to each parameter
!absparams at each evaluated point NU.
!By using global variables linepropCO/CO2 CO and CO2 absorption is evaluated and abs adds
!the effect of each transition within the range [NUupper,Nulower]

        use nrtype
        use AdjustConstants
        use nrutil, only: assert_eq
        use absCOutil, only: FindAbsorptionCoeff

        implicit none
        real(sp), dimension(:), intent(in):: NU,absparams
        real(sp), dimension(:), intent(out):: absorption
        real(sp), dimension(:,:), intent(out):: dyda

        real(sp), dimension(nsentcoeff):: aa
        real(sp), dimension(nsentcoeff+1):: dkda            !this extra element in array
is for dkdNUoff
        real(sp), dimension(size(NU),nsentcoeff+1):: dkdaCO, dkdaCO2
        real(sp), dimension(size(NU)):: kwCO,kwCO2
        integer(i4b):: dummi,j,ndata
        real(sp):: length,absoff
        logical(lgt):: isCO,withCO2

        dummi=assert_eq(size(absparams),size(dyda,2),nabsparams, 'AbsCalc1')
        ndata=assert_eq(size(NU),size(absorption),size(dyda,1),'AbsCalc2')
```

```
        !Prepare for CO absorption coefficient
        isCO=.TRUE.
        aa(1)=absparams(1)                                          !Temp
        aa(2)=absparams(2)                                          !P
        aa(3)=absparams(3)                                          !xgasCO
        aa(4)=absparams(6)                                          !gammafactorCO
        do j=1, ndata
                call FindAbsorptionCoeff(NU(j)+absparams(8),aa,kwCO(j),isCO,dkda)
                dkdaCO(j,:)=dkda(:)
        end do

        !Prepare for CO2 absorption coefficient
        withCO2=.TRUE.
        isCO=.FALSE.
        aa(1)=absparams(1)                                  !Temp
        aa(2)=absparams(2)                                  !P
        aa(3)=absparams(4)*1.0e4_sp                         !xgasCO2 [ppm]
        aa(4)=absparams(7)                                  !gammafactorCO2
        if (aa(3) == 0.0_sp) withCO2=.FALSE.

        if (withCO2 == .TRUE.) then
                do j=1, ndata
                        call FindAbsorptionCoeff(NU(j)+absparams(8),aa,kwCO2(j),isCO,dkda)
                        dkdaCO2(j,:)=dkda(:)
                end do
        else
                kwCO2(:)=0.0_sp
                dkdaCO2(:,:)=0.0_sp
        end if

        length=absparams(5)*100.0_sp                !100cm=1m to convert lenght to cm
        absoff=absparams(9)
        absorption(:)=1.0_sp-dexp(-1.0_sp*length*(kwCO(:)+kwCO2(:)))+absoff

        !evaluate partial derivatives
        !absorption respect to temperature
        dyda(:,1)=(absorption(:)-1.0_sp-absoff)*(-1.0_sp*length*(dkdaCO(:,1)+
dkdaCO2(:,1)))

        !absorption respect to pressure
        dyda(:,2)=(absorption(:)-1.0_sp-absoff)*(-1.0_sp*length*(dkdaCO(:,2)+
dkdaCO2(:,2)))

        !absorption respect to xgasCO
        dyda(:,3)=(absorption(:)-1.0_sp-absoff)*(-1.0_sp*length*dkdaCO(:,3))

        !absorption respect to xgasCO2
        dyda(:,4)=(absorption(:)-1.0_sp-absoff)*(-1.0_sp*length*dkdaCO2(:,3))

        !absorption respect to length
        dyda(:,5)=dexp(-1.0_sp*length*(kwCO(:)+kwCO2(:)))*(kwCO(:)+kwCO2(:))

        !absorption respect to gammafactorCO
        dyda(:,6)=(absorption(:)-1.0_sp-absoff)*(-1.0_sp*length*dkdaCO(:,4))

        !absorption respect to gammafactorCO2
        dyda(:,7)=(absorption(:)-1.0_sp-absoff)*(-1.0_sp*length*dkdaCO2(:,4))

        !absorption respect to freq offset in wave numbers NUoff
        dyda(:,8)=(absorption(:)-1.0_sp-absoff)*(-1.0_sp*length*(dkdaCO(:,5)+
dkdaCO2(:,5)))

        !absorption respect to absorption offset absoff
        dyda(:,9)=1.0_sp

end subroutine AbsCalc
```

A.2.4 Subroutine FindAbsorptionCoeff

```
        Subroutine FindAbsorptionCoeff(NUlaser,absparams,kw,isCO,dkda)
        !       Given the indication of CO (isCO=TRUE) or CO2 (isCO=FALSE); evaluates the
        !total spectral absorption coefficient kw [cm^-1] at the given NUlaser frequency.
        !Spectral data contained in the global variable linepropCO/CO2 is used under
        !conditions passed in absparams (Temp,P,xgas,gammafactor respectively).

                use nrtype
                use AdjustConstants
                use absCOconstants
                use HitranInfo
                use nrutil, only: assert_eq

                implicit none
                real(sp), dimension(:), intent(in):: absparams
                real(sp), intent(in):: NUlaser
                real(sp), intent(out):: kw
                logical(lgt), intent(in):: isCO
                real(sp), dimension(:), intent(out):: dkda

                integer(i4b)::jj,nline,dumi
                real(sp), dimension(:,:), allocatable:: lineprop
                real(sp), dimension(:), allocatable:: NU21, S21, gammaAir, gammaSelf, E,
nbroad, isoname
                real(sp):: Temp,P,xgas,gammafactor,QTemp,PM,QTref,nlower
                real(sp):: gammacorr,deltaNUc,deltaNUd,x,y,wreal,gv,SijT
                real(sp):: dwdx, dwdy, dQdT, dNUcdT, dNUddT, dydT, dxdT, dwdT, dgdT, dSdT,
dndT, dNUcdP, dydP, dwdP
                real(sp):: dgdP, dndP, dNUcdX, dydX, dwdXX, dgdX, dndX, dNUcdG, dydG,
dwdG, dgdG, dxdNUoff, dwdNUoff, dgdNUoff

                if (isCO) then
                        allocate(lineprop(size(linepropCO,1),size(linepropCO,2)))
                        lineprop(:,:)=linepropCO(:,:)
                        PM=PMCO
                else
                        allocate(lineprop(size(linepropCO2,1),size(linepropCO2,2)))
                        lineprop(:,:)=linepropCO2(:,:)
                        PM=PMCO2
                end if

                dumi=assert_eq(size(lineprop,2),nprop, 'FindAbsorption1')
                dumi=assert_eq(size(absparams),nsentcoeff, 'FindAbsorption2')
                dumi=assert_eq(size(dkda),nsentcoeff+1, 'FindAbsorption3')

                nline=size(lineprop,1)
                allocate (NU21(nline), S21(nline), gammaAir(nline), gammaSelf(nline),
E(nline), nbroad(nline), isoname(nline))

                NU21(:)=lineprop(:,1)
                S21(:)=lineprop(:,2)
                gammaAir(:)=lineprop(:,3)
                gammaSelf(:)=lineprop(:,4)
                E(:)=lineprop(:,5)
                nbroad(:)=lineprop(:,6)
                isoname(:)=lineprop(:,7)

                Temp=absparams(1)
                P=absparams(2)
                xgas=absparams(3)
                gammafactor=absparams(4)
                nlower=(P*133.322368_sp)*(xgas*1.0e-6_sp)/(kb*Temp)         !m^-3
                dndT=-1.0_sp*nlower/Temp
                dndP=nlower/P
                dndX=nlower/xgas

                kw=0.0_sp
                dkda(:)=0.0_sp

                !Contribution of each transition to the absorption at the laser freq.
                do jj=1,nline

                        !Calculate transition halfwith and correct for temperature
```

```
                        gammacorr=((Tref/Temp)**nbroad(jj))*((gammaAir(jj)*(P/760.0_sp)*
(1.0_sp-(xgas*1.0e-6_sp)))+(gammaSelf(jj)*(P/760.0_sp)*(xgas*1.0e-6_sp)))
                        !Line collisional width (cm^-1)
                        deltaNUc=2.0_sp*gammacorr*gammafactor

                        !Line Doppler width (cm^-1)
                        deltaNUd=7.162e-7_sp*NU21(jj)*dsqrt(Temp/PM)

                        !Evaluation of Partition function at Tref & Temp
                        call PartitionSums(Tref,QTref,dQdT,int(isoname(jj)),isCO)
                        call PartitionSums(Temp,QTemp,dQdT,int(isoname(jj)),isCO)

                        !Temperature correction of line intensity
                        SijT=S21(jj)*(QTref/QTemp)*((dexp(-1.0_sp*c2*E(jj)/Temp))/(dexp(-
1.0_sp*c2*E(jj)/Tref)))*((1.0_sp-dexp(-1.0_sp*c2*NU21(jj)/Temp))/(1.0_sp-dexp(-1.0_sp*
c2*NU21(jj)/Tref)))

                        !Voigt parameters
                        x=2.0_sp*dsqrt(lntwo)*((NUlaser-NU21(jj))/deltaNUd)
                        y=dsqrt(lntwo)*(deltaNUc/deltaNUd)
                        call voigtprofile(x,y,wreal,dwdx,dwdy)

                        gv=dsqrt(lntwo/pi)*(2.0_sp/deltaNUd)*wreal
                        kw=kw+((SijT*nlower*1.0e-6_sp)*gv)   !factor 1.0d-6cm^-3=1m^-3

                        !Calculate the partial derivatives with respect to each absparam
                        dNUcdT=-1.0_sp*deltaNUc*nbroad(jj)/Temp
                        dNUddT=0.5_sp*deltaNUd/Temp
                        dydT=(y*dNUcdT/deltaNUc)-(y*dNUddT/deltaNUd)
                        dxdT=-1.0_sp*x*dNUddT/deltaNUd
                        dwdT=(dwdx*dxdT)+(dwdy*dydT)
                        dgdT=(gv*dwdT/wreal)-(gv*dNUddT/deltaNUd)
                        dSdT=(-1.0_sp*SijT*dQdT/QTemp)+(SijT*c2*E(jj)/(Temp**2))+(-
1.0_sp*SijT*c2*NU21(jj)*dexp(-1.0_sp*c2*NU21(jj)/Temp)/(1-dexp(1.0_sp*c2*NU21(jj)/Temp)))
                        dNUcdP=deltaNUc/P
                        dydP=y*dNUcdP/deltaNUc
                        dwdP=dwdy*dydP
                        dgdP=gv*dwdP/wreal
                        dNUcdX=2.0_sp*gammafactor*((Tref/Temp)**nbroad(jj))*(P/760.0_sp)
*(gammaAir(jj)+gammaSelf(jj))
                        dydX=y*dNUcdX/deltaNUc
                        dwdXX=dwdy*dydX
                        dgdX=gv*dwdXX/wreal
                        dNUcdG=deltaNUc/gammafactor
                        dydG=y*dNUcdG/deltaNUc
                        dwdG=dwdy*dydG
                        dgdG=gv*dwdG/wreal
                        dxdNUoff=2.0_sp*dsqrt(lntwo)/deltaNUc
                        dwdNUoff=dwdx*dxdNUoff
                        dgdNUoff=gv*dwdNUoff/wreal

                        !Partial derivative of kw respect to Temp
                        dkda(1)=dkda(1)+(1.0e-6_sp*nlower*gv*dSdT)+(1.0e-6_sp*SijT*gv*
dndT)+(1.0e-6_sp*nlower*SijT*dgdT)

                        !Partial derivative of kw respect to P
                        dkda(2)=dkda(2)+(1.0e-6_sp*SijT*gv*dndP)+(1.0e-6_sp*SijT*nlower*
dgdP)

                        !Partial derivative of kw respect to xgas
                        dkda(3)=dkda(3)+(1.0e-6_sp*SijT*gv*dndX)+(1.0e-6_sp*SijT*nlower*
dgdX)

                        !Partial derivative of kw respect to gammafactor
                        dkda(4)=dkda(4)+(1.0e-6_sp*SijT*nlower*dgdG)

                        !Partial derivative of kw respect to NUoffset
                        dkda(5)=dkda(5)+(1.0e-6_sp*SijT*nlower*dgdNUoff)
                end do
                deallocate (lineprop)
        end subroutine FindAbsorptionCoeff
```

A.2.5 evolution.f90

```
subroutine evolution(xdata,ydata,parammax,parammin,bparam,bchisq,fname,trialfactor)
!       Implements the evolutionary algorithm. Given the limits [paramax,parammin] of
!each parameter of the function fname the best fit to the data [xdata,ydata] is obtained.
!After maxgen generations the best-fit is based in the parameters set bparam with the
!minimum chisquare bchisq.
!Supply the subroutine fname

        use nrtype
        use AdjustConstants
        use nrutil, only: assert_eq
        use nr, only: rann
        use darwinutil, only: calcchisq, sortchisq

        implicit none
        integer(i4b), intent(in):: trialfactor
        real(sp), dimension(:), intent(in):: xdata,ydata,parammax,parammin
        real(sp), dimension(:), intent(out):: bparam
        real(sp), intent(out):: bchisq
        interface
                subroutine fname(x,param,eval,derivada)
                        use nrtype
                        real(sp), dimension(:), intent(in):: x,param
                        real(sp), dimension(:), intent(out):: eval
                        real(sp), dimension(:,:):: derivada
                end subroutine fname
        end interface

        integer(i4b):: nop,nparam,j,i,k,l,ikeep,lp1,lp2,inicio
        integer(i4b), dimension(8):: fecha
        real(sp):: ran,gene
        real(sp), dimension(maxsets):: chisq
        real(sp), dimension(size(parammax),maxsets):: work

        nop=assert_eq(size(xdata),size(ydata), 'evolution1')
        nparam=assert_eq(size(parammax),size(parammin), 'evolution2')

        !initialize the random number routine
        call date_and_time(VALUES=fecha)
        inicio = int((fecha(6)*fecha(8))/sqrt(dble(fecha(7))))
                                !minutes*miliseconds/sqrt(seconds) (60)(1000)/V60

        !set initial parameters array within limits
        do j=1, maxsets
                do i=1, nparam
                        ran=rann(inicio)
                        work(i,j)=parammin(i)+(ran*(parammax(i)-parammin(i)))
                end do
        end do

        !calculate chi-square for all sets
        do j=1,maxsets
                chisq(j)=calcchisq(fname,xdata,ydata,work(:,j))
        end do

        !sort chi-square by size
        call sortchisq(work,chisq)

        !Iterate generations until maxgen is reached
        ikeep=idint(dble(maxsets)*dkeep)
        do k=1, (maxgen*trialfactor)
                write(*,*) 'process generation ',k,'   of',(maxgen*trialfactor)
                do l=ikeep+1, maxsets         !keep the best chisq sets
                        if (l >= (maxsets-ikeep)) then  !for the worst chisq
                                do j=1, nparam
                                        ran=rann(inicio)
                                        work(j,l)=parammin(j)+(ran*(parammax(j)-
parammin(j)))
                                end do
                        else    !the intermediate chisq are mixed up among them
                                lp1=1
                                lp2=lp1
                                do while (lp1==lp2)
                                        ran=rann(inicio)
```

```
                                        lp1=int(ran*ikeep)+1
                                        ran=rann(inicio)
                                        lp2=int(ran*ikeep)+2
                                end do
                                do j=1, nparam
                                        ran=rann(inicio)
                                        if (gene < 0.2) then
                                                work(j,l)=work(j,lp1)
                                        else if (gene < 0.4) then
                                                work(j,l)=work(j,lp2)
                                        else if (gene < 0.7) then
                                                ran=rann(inicio)
                                                work(j,l)=work(j,lp1)+(ran*(work(j,lp2)-
work(j,lp1)))
                                        else
                                                ran=rann(inicio)
                                                work(j,l)=parammin(j)+(ran*(parammax(j)-
parammin(j)))
                                        end if
                                end do
                        end if
                        chisq(l)=calcchisq(fname,xdata,ydata,work(:,l))
                end do
                call sortchisq(work,chisq)
                write(*,*) 'best chisq for this generation: ', chisq(1)
        end do

        !transfer best parameter set
        bparam(:)=work(:,1)
        bchisq=chisq(1)

end subroutine evolution
```

A.2.6 LMBestFit.f90

```
Subroutine LMBestFit(xdata,ydata,a,maska,funcs,bchisq,errora,tol,sig)
!       This routine is used to call mrqmin.f90 (from Numerical Recipes in Fortran) so
!controlling the application of Levenberg-Marquardt method to reduce the chi-square of
!the fit of the data [xdata,ydata] and a non-linear function funcs that depends on m
!parameters a. By adjusting the parameters indicated in maska with TRUE the routine
!obtains the best-fit parameters and the estimated parameters errors.
!The best fit is achieved when chi-square of sucesive iterations agree within tolerance
!tol.

        use nrtype
        use nrutil, only: assert_eq
        use nr, only: mrqmin

        implicit none

        real(sp), dimension(:), intent(in):: xdata,ydata,sig
        real(sp), dimension(:), intent(inout):: a
        real(sp), dimension(:), intent(out):: errora
        real(sp), intent(out):: bchisq
        real(sp), intent(in):: tol
        logical(lgt), dimension(:), intent(in):: maska
        interface
                subroutine funcs(x,a,yfit,dyda)
                        use nrtype
                        real(sp), dimension(:), intent(in):: x,a
                        real(sp), dimension(:), intent(out):: yfit
                        real(sp), dimension(:,:), intent(out):: dyda
                end subroutine funcs
        end interface

        integer(i4b) :: kk,npoints,mparams
        real(sp) :: alamda,chisq,initialchisq,chisqchange
        real(sp), dimension(size(a),size(a)):: covar,alpha

        npoints=assert_eq(size(xdata),size(ydata),size(sig), 'LMBestFit1')
        Mparams=assert_eq(size(a),size(maska),size(errora),'LMBestFit2')
```

```
        covar(:,:)=0.0_sp
        alpha(:,:)=0.0_sp
        chisq=10.0_sp
        alamda=-1.0_sp

        !call to fit
        chisqchange=1.0_sp
        do while (chisqchange > tol)
                initialchisq=chisq
                call mrqmin(xdata,ydata,sig,a,maska,covar,alpha,chisq,funcs,alamda)
                chisqchange=dabs(initialchisq-chisq)
        end do

        !last fit call
        alamda=0.0_sp
        call mrqmin(xdata,ydata,sig,a,maska,covar,alpha,chisq,funcs,alamda)
        bchisq=chisq

        !Errors from covarianze matrix
        do kk=1, Mparams
                if (covar(kk,kk) >= 0.0_sp) then
                        errora(kk)=dsqrt(dabs(covar(kk,kk)))
                else
                        errora(kk)=-1.0_sp*dsqrt(dabs(covar(kk,kk)))
                end if
        end do

end subroutine LMBestFit
```

APPENDIX B

LOCK-IN AMPLIFIER OPERATION FUNDAMENTALS

B.1 The Lock-in Amplifier - Introduction

Lock-in Amplifiers are used because the improvement of the SNR of the measured signal in an experiment through phase sensitive detection (PSD). Phase sensitive, synchronous detection is a powerful technique to recover small ac signals which may be obscured by noise. Lock-in amplifiers SR830 from Stanford Research Systems were used in processing the signals from the analytical and reference detectors of the CO sensor.

The principles of lock-in are covered in common electronics textbooks [154, 155], also software simulations of the instrument response are available [156, 157]. The lock-in amplifier theory given in this appendix is not intended to be comprehensive but rather introductive to the operation basics of a lock-in amplifier and the important parameters for its application to direct optical absorption measurements.

Figure 41 shows a schematic of the lock-in amplifier. A lock-in amplifier is basically composed by the internal oscillator, a phase locked loop, a 90º phase shifter, two multiplier stages, and two low pass filters. Lock-in measurements require a frequency reference, thus the CO sensor was modulated by the optical chopper and the lock-in detected the response from the experiment at the chopper frequency. The TTL synchronous output from the chopper was used for the reference frequency of the lock-in amplifier. The SR830 uses a phase locked loop (PLL) that allows the internal oscillator to generate a digitally

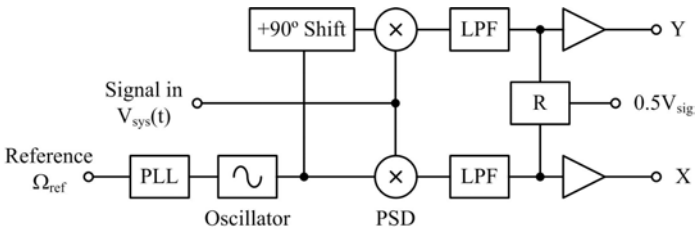

FIGURE 41 SR830 Lock-in amplifier schematic diagram. PLL – phase locked loop, PSD – phase sensitive detector, and LPF – low pass filter

synthesized sine wave at the reference frequency (Ω_{ref}) as given by (102). The PLL actively locks the internal oscillator to the external reference thus changes in the external reference frequency do not affect the measurement.

$$V_{ref} = \sin(\Omega_{ref} t + \theta_{ref}) \tag{102}$$

Consider the system response (V_{sys}), in terms of voltages, as

$$V_{sys} = V(t) + V_{noise}(t) \tag{103}$$

where $V(t)$ is the signal to be measured and $V_{noise}(t)$ is noise included in the signal from many sources including background, shot, Johnson and $1/f$ noise sources. As a first approach, consider

$$V(t) = V_{sig} \sin(\Omega_{sig} t + \theta_{sig}) \tag{104}$$

where Ω_{sig}, V_{sig}, and θ_{sig} are the angular frequency, amplitude, and phase of the response respectively.

The phase-sensitive detector (PSD) in the SR830 multiplies V_{sys} and the internal reference sine obtaining

$$\begin{aligned} V_{PSD} = {} & 0.5V_{sig} \cos([\Omega_{sig} - \Omega_{ref}]t + \theta_{sig} - \theta_{ref}) - 0.5V_{sig} \cos([\Omega_{sig} + \Omega_{ref}]t + \theta_{sig} + \theta_{ref}) + \\ & + V_{noise}(t) \sin(\Omega_{ref} t + \theta_{ref}) \end{aligned} \tag{105}$$

which represents two ac signals at frequencies (Ω_{sig}-Ω_{ref}) and (Ω_{sig}+Ω_{ref}). However, since the internal oscillator is locked to the reference frequency at which the experiment is modulated, i.e. the chopper frequency, then $\Omega_{sig} = \Omega_{ref}$ and the difference frequency component will be a dc signal. The low pass filter following the multiplier provides the average that removes the ac component.

The noise multiplied by the sinusoidal reference is not affected; recall that the noise has a zero expectation value. Thus the last term in (105) can be replaced for a new random variable. The PSD and the low pass filter eliminate frequency components away from the reference frequency. Neither (Ω_{ref}-Ω_{noise}) nor (Ω_{ref}+Ω_{noise}) are close to dc, however noise frequencies very close to the Ω_{ref} will result in very low ac outputs from the PSD and their attenuation depends on the bandwidth and roll-off of the low pass filter. Thus the low pass filter determines the bandwidth of the detection.

The output from the low pass filter is given by

$$X = 0.5V_{sig}\cos(\theta_{sig} - \theta_{ref}) + V'_{noise}(t) \tag{106}$$

where V'_{noise} is the filter output noise. This lock-in amplifier output is proportional to the phase difference between the signal modulation and the oscillator reference. This phase dependency can be eliminated with the second PSD in which the signal is multiplied with a reference sine shifted 90º. The filtered output of this second PSD will be

$$Y = 0.5V_{sig}\sin(\theta_{sig} - \theta_{ref}) + V'_{noise}(t) \tag{107}$$

The two outputs X and Y represent the signal as a vector relative to the lock-in reference oscillator. These components are called "in-phase" and "quadrature" respectively. The amplitude of the signal is computed by calculating the magnitude of the vector (R) which removes the phase dependency. The expectation value of the square of the magnitude is given by

$$\left\langle R^2 \right\rangle = [0.5V_{sig}\cos(\theta_{sig} - \theta_{ref})]^2 + [0.5V_{sig}\sin(\theta_{sig} - \theta_{ref})]^2 + 2\sigma_n^2 \tag{108}$$

where σ^2_n is the noise power introduced by the filtered noise signal. If the low pass filter cut off frequency is low enough for a severe attenuation of the noise interference, which is a common case for a lock-in amplifier, the noise power can be neglected. Thus the lock-in amplifier output gives

$$R = 0.5\,V_{sig} \tag{109}$$

For the previous development, the signal to be measured was given by (104) as a sine function. Usually this is not the case; however given the periodicity of the ac input signal, any input signal can be represented by a sine Fourier series expansion of the form

$$V(t) = \sum_{m=1}^{\infty} b_m \sin(m\Omega t + \theta) \tag{110}$$

thus, since the SR830 lock-in amplifier uses a pure sine in the PSD and the sine wave is an orthogonal function, the lock-in amplifier will measure the coefficient b_m of the series component at the reference frequency. In other words, for an ideal lock-in amplifier only inputs at the reference frequency (Ω_{ref}) will result in an output. This property allows for detection of higher harmonics with the use of lock-in amplifiers by setting the correspondent multiple of the reference frequency.

For a real lock-in amplifier, the output will contain signals close to the reference frequency. The detection bandwidth of the lock-in amplifier is set by the low pass filter time constant and roll-off. By increasing the time constant, the output becomes steadier and reliable measurements are possible. However, when the time constant increases, the waiting period for the filter to reach its final value also increases. Thus, changes in the input signal are reflected at the output after many time constants. The time constant reflects how slowly the output responds and the degree of smoothening of the output. The equivalent noise bandwidth (*ENBW*) of the filter is determined by the time constant and the roll-off slope. The SR830 lock-in amplifier has a four filter stages that allows for up to 24 dB/oct of roll-off. For a time constant τ and a slope of 24 dB/oct, the waiting time is 10τ and the ENBW is given by

$$ENBW = \frac{5}{64\tau} \tag{111}$$

In practice, the selection of a large time constant produces the low pass filter to average the signal and the lock-in amplifier output tends to have a sinusoidal shape. For very low time constants the filter bandwidth increases and more noise is observed in the output, in addition, and because of the amplification stages at the lock-in input and after the PSD, the amount of noise can overload the instrument.

B.2 Time Constant Effect on Direct Absorption Measurements

For the direct absorption experiments performed, a poor choice of the lock-in amplifier settings and the experiment conditions can result in affecting the shape of the absorption feature leading to false results from the fitting procedure. It is desirable to modulate the experiment at a higher reference frequency because the reduction of the 1/*f* noise. In the CO sensor system, the modulation frequency was determined by the speed of the chopper blade and the beam size. For the experimental system described in Chapter IV the maximum chopper frequency was 3 kHz. Thus, the 12 GHz of the ECDL scanning range were modulated on/off every 0.166 ms. As seen before, the modulation is removed by the PSD which recovers the amplitude V_{sig} of the measured signal. In (104) V_{sig} was considered to be constant with time, but for the sweeping of the absorption trace V_{sig} is actually a function of time that reproduces the Voigt

profile of the absorption feature. After the PSD, $V_{sig}(t)$ was averaged by the low pass filter. In this filtering stage the time constant can affect the shape of the absorption feature. If the waiting time (=10τ for 26 dB/oct roll-off) was as large as the time that takes to scan the absorption trace, i.e. acquisition time, the output of the low pass filter will be the exponential average of the trace. And the absorption feature will not be reproduced. Lowering the time constant or increasing the data acquisition time will result in averaging $V_{sig}(t)$ values close to each other. The drawback is that decreasing the time constant more noise is passed to the lock-in output since the ENBW increases.

The data acquisition time to scan the absorption feature was determined by the ECDL scanning frequency. The ECDL scanning frequency was controlled by the piezoelectric crystal; although scanning rates of 10 kHz are possible with the piezoelectric crystal, the upper limit was set by the single mode operation of the laser. As described in Chapter V, the ECDL was commonly scanned at 1.3 Hz for the gas cell measurements and field tests and at 260 mHz for the hydrogen/air flames experiments. At these rates $V_{sig}(t)$ was slowly acquired. As long as the function is smooth in time, i.e. small gradients in time, the averaging of the low pass filter does not distort the absorption shape. However, for narrow absorption features, the $V_{sig}(t)$ trace has very sharp peaks that are prone to be affected by the averaging of the low pass filter.

It is clear that, the incorrect settings of the lock-in amplifier affect the shape of the absorption trace. The averaging of the absorption trace reduces its peak absorption and increases the spam of the wings. These are characteristics of a "more" Lorentzian shape and thus, it is anticipated that the best-fit pressure and CO concentration will be affected by the change in lock-in amplifier time constant. To observe these effects a series of simulations were performed on the 0.32-m long room temperature gas cell on the CO fundamental band transition R(11) at 2186.6390 cm^{-1}. Fig. 42 shows the change in the absorption trace as the gas cell pressure was varied from 3.33 to 79.99 kPa. It is observed that the wings of the trace get thicker as the pressure increases but the peak absorption approaches an asymptotic value at 0.511, as observed in Fig. 25 for CO fundamental band transition R(23). Thus the averaging effect of a long time constant can be adjusted by fitting the pressure parameter. To reduce the peak absorption of the trace, the CO concentration has to be reduced. Fig. 43 shows the simulation of reducing the CO

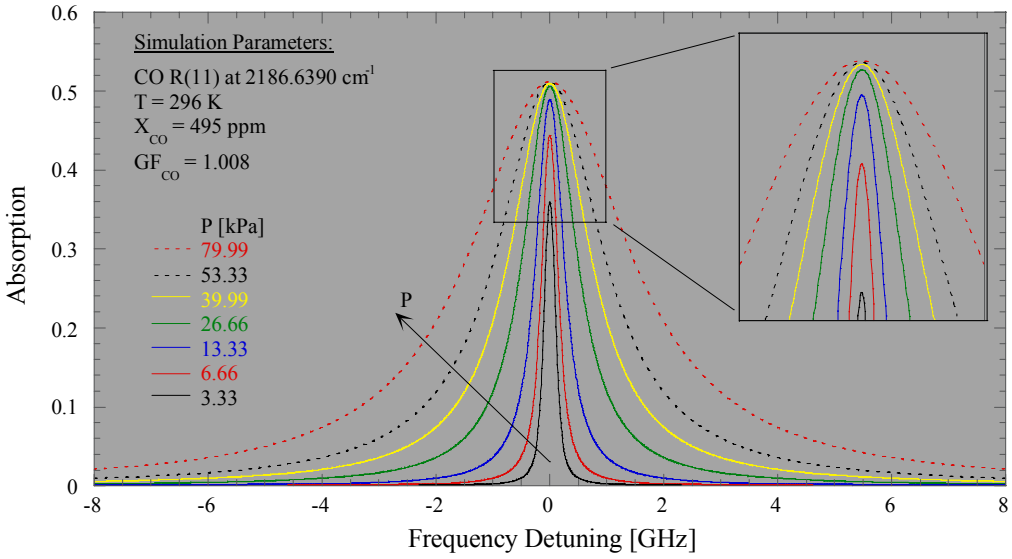

FIGURE 42 Pressure dependence on the absorption line shape. Theoretical absorption line shape for R(11) transition of the fundamental band of CO at 2186.6390 cm^{-1}. Data simulated the expected line shape for absorption in a 32 cm long gas cell at room temperature filled at the indicated pressures with a gas mixture of 495 ppm CO and balance N_2. By increasing the pressure the absorption trace becomes Lorentzian as expected, see Fig. 25

concentration from 1010 to 50 ppm while keeping the room temperature gas cell pressure to a value of 6.66 kPa. From Figs 42 and 43 it is clear that when the lock-in time constant affects the absorption shape the resulting best-fit pressure and CO concentration will deviate from the actual experimental gas cell conditions. The resulting best-fit pressure is expected to be higher while best-fit X_{CO} will be lowered significantly depending on the effect of the time constant.

To corroborate this observations a series of experiments on the gas cell were performed to measure absorption of the CO fundamental band transition R(11) at 2186.639 cm^{-1}. First, the gas cell was filled with a Matherson certified mixture of 495 ppm CO in buffer gas N_2. The cell was kept at 296 K and the gas mixture pressure was varied from 100 to 600 torr. Data was taken in two sets that differentiate by the processing of the signals from the analytical and reference detectors. In one set the signals from the detectors were recorded directly, on the other set, the signals were processed by the SR830 lock-in amplifiers set to τ = 3 ms with a filter roll-off of 24 dB/oct. The acquired data was fitted by the "Direct_Absorption" code T, L, and GF_{CO} were set fixed while the best-fit X_{CO} and P were determined.

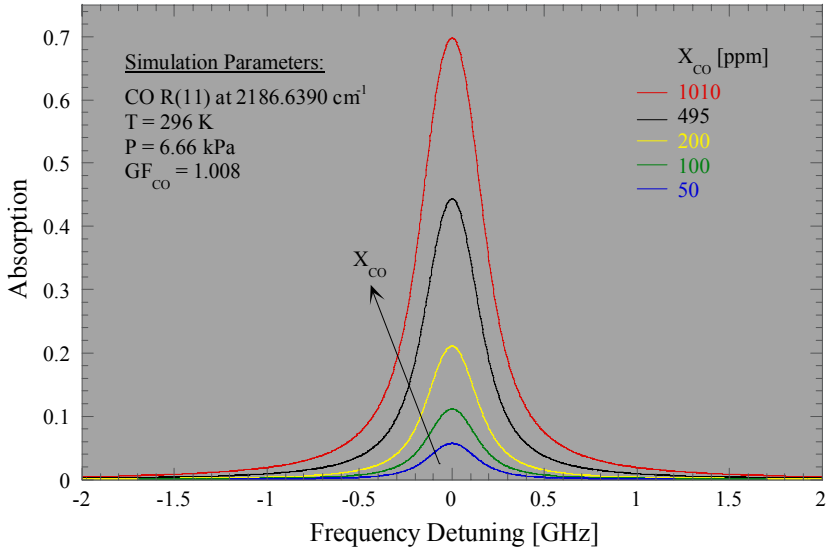

FIGURE 43 CO concentration dependence on the absorption line shape. Theoretical absorption line shape for R(11) transition of the fundamental band of CO at 2186.6390 cm^{-1}. Data simulated the expected line shape for absorption in a 32 cm long gas cell at room temperature filled to 6.66 kPa with a gas mixture of indicated CO concentrations with buffer gas N_2. By increasing the CO concentration only the peak absorption increases significantly

The assumed gamma factor for transition R(11) was 1.008, this value is the average obtained from the literature published values of $\gamma^{o}_{CO\text{-}N2}$ (0.0627 cm^{-1}/atm [138], 0.05707 cm^{-1}/atm [139], 0.05737 cm^{-1}/atm [140], and 0.0565 cm^{-1}/atm [64]) and the CO concentration of the certified mixture X_{CO} = 495 ppm.

Figure 44 shows the comparison of the best-fit parameters obtained when the data was taken with and without the lock-in amplifier. It is clear that the signals processed without the lock-in amplifier were unaffected. For the no lock-in case the best-fit CO concentration agrees with the mixture concentration at all tested pressures, whereas the best-fit pressure follows the pressure gauge readings. However the data from the signals processed by the lock-in amplifiers produced false results. For narrow lines, observed at lower pressures, the averaging of the low pass filter greatly reduces the peak absorption. The CO concentration was under-predicted up to 68% of the gas cell mixture composition. It is observed that as the gas cell pressure increases the CO concentration approaches to 495 ppm because the line broadens and the effect of the averaging is diminished. As expected, the best-fit pressure is higher than the gauge

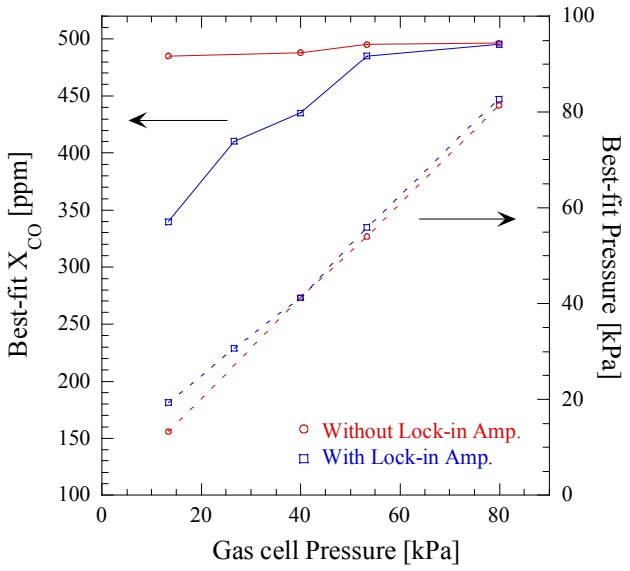

FIGURE 44 Comparison of data processed with and without the lock-in amplifier. Data processed without the lock-in amplifier results in the expected fit to the gas cell conditions. As the gas cell pressure increases the absorption feature broadens and the best-fit pressure and CO concentration are affected by the lock-in amplifier. Experiments were performed on CO fundamental band transition R(11) in the 0.32 m long room temperature gas cell filled with a certified gas mixture of 495 ppm CO in N_2. The lock-in $\tau = 3$ ms with a roll-off of 24 dB/oct. For the fit GF_{CO} was set to 1.008

pressure, and shows the same behavior as the best-fit concentration, as gas cell pressure increases and line broadens; the best-fit pressure better corresponds to the gauge pressure.

For this series of experiments the lock-in time constant was set constant allowing to observe its effect as the transitions broadens. The next set of experiments was designed to observe the effect of the time constant on a narrow line. The 0.32 m long room temperature gas cell was filled to 6.66 kPa of the same certified gas mixture of 495 ppm CO in N_2. At this low pressure, the line FWHM was about 0.44 GHz making it very likely to be affected by the averaging of the low pass filter. The time constant was changed from 0.1 to 30 ms, lower τ were not possible since the low noise rejection overloaded the instrument. Fig. 45 shows the resulting best-fit X_{CO} and P as a function of the lock-in time constant. It is evident that as the time constant increases the smoothening of the absorption trace erases the information on the absorption shape leading to increasingly lower CO concentrations and larger best-fit pressures. It is observed that at any available filter roll-off the general trend is followed. However the difference

observed is due to the noise present in the output signal which introduces uncertainty to the fitting process. For instance, the ENBW for the 24 dB/oct roll-off is 3.5 times narrower than the ENBW at 6 dB/oct.

This series of experiments have shown how the correct settings of the lock-in amplifier are essential for the appropriate interpretation of the absorption data. The proper setting of the lock-in amplifier, especially the time constant are dependent on the width of the transition limiting the noise rejection for very narrow lines. In practice, the locking settings such as phase, gain, and instrument sensitivity are set by the auto functions of the SR830 lock-in amplifier to the optimum values given the input signal. However, the time constant is a parameter that most be carefully adjusted by the user since its effect can only be understood in the light of a rapidly changing experiment.

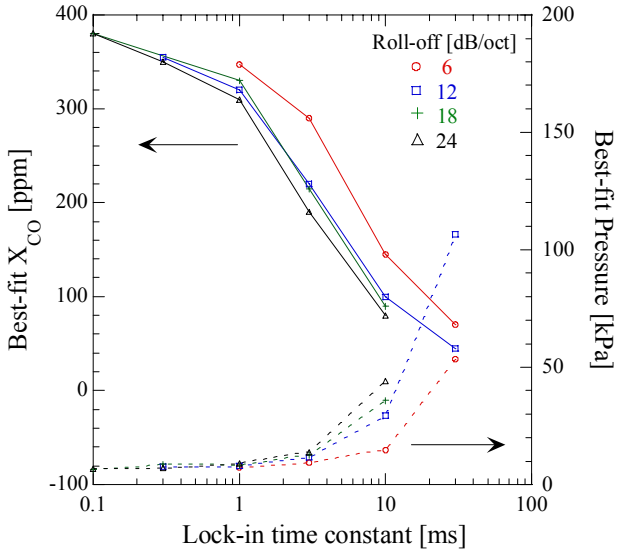

FIGURE 45 Effect of the lock-in time constant over the best-fit X_{CO} and P in the direct absorption measurements. The 0.32 m gas cell was filled with a gas mixture of 495 ppm CO in buffer gas N_2 at 296 K and 6.66 kPa. At this pressure, the FWHM of the R(11) transition of the CO fundamental band was 0.44 GHz

VITA

Rodolfo Barron Jimenez

Pasajero 314, Salamanca Gto., 36700, México

A native of central México, Mr. Barron was awarded a Bachelor of Science degree in mechanical engineering by the Universidad de Guanajuato in June, 1999. After graduation and a semester as an engineer intern at Ferranti Packard de México he began graduate studies under Prof. G. P. Peterson at Texas A&M University. At the Two-Phase Laboratory he was completely responsible of an experimental investigation of condensation in micro-grooved plates. He obtained the degree of Master of Science in mechanical engineering at Texas A&M University in May, 2001.

In the spring of 2001 he began working in the Diode-Laser-Based Sensor Laboratory at Texas A&M University under the guidance of Prof. R. P. Lucht. He started actively collaborating in the development of hydroxyl radical and nitric oxide sensors. Later he was responsible for the development and testing of the carbon monoxide sensor. He received the degree of Doctor of Philosophy in mechanical engineering in December 2004. This degree sets the stage for the development of a career as a scientist.

Publication of several referenced papers and other research related activities have given him professional satisfaction. He has been a reviewer of several publications for the AIAA and SOMIM journals, participated in combustion and heat transfer conferences, and won the 1998 ASME Young Design-Engineer's Paper Competition. Through his academic endeavors, Mr. Barron has been involved in student organizations serving as chairman in the ASME Student Section of the Universidad de Guanajuato and MEGSO in the Department of Mechanical Engineering at Texas A&M University. While pursuing his graduate degrees he earned a national scholarship from CONACYT (Mexican Government Agency for Science and Technology) as well as Fellowships from the College of Engineering at Texas A&M University.